Development of a Phoswich Detector for Neutron Dose Rate Measurements in the Earth's Atmosphere

Dissertation
zur Erlangung des Doktorgrades
der Mathematisch-Naturwissenschaftlichen Fakultät
der Christian-Albrechts-Universität
zu Kiel

vorgelegt von
Esther Miriam Dönsdorf

Kiel, 2014

Erster Gutachter:	Prof. Dr. Bernd Heber
Zweiter Gutachter:	Prof. Dr. Holger Kersten
Tag der mündlichen Prüfung:	30.04.2014
Zum Druck genehmigt:	30.04.2014

gez. Prof. Dr. Wolfgang J. Duschl, Dekan

Zusammenfassung

Die Erde ist einem konstanten Strom energiereicher Teilchen ausgesetzt. Durch die Wechselwirkung dieser Strahlung mit der Magnetosphäre und Atmosphäre entsteht ein komplexes Strahlungsfeld, welches sich mit der Position innerhalb der Erdatmosphäre ändert. Es besteht aus geladenen und ungeladenen Teilchen und führt zu der permanenten Strahlenexposition des Menschen. Da diese ionisierende Strahlung für Menschen gefährlich sein kann, ist es notwendig Dosisraten in verschiedenen Höhen in der Erdatmosphäre zu messen. Aufgrund ihrer höheren biologischen Wirksamkeit ist die Exposition durch Neutronen gefährlicher als die durch γ-Strahlung oder geladene Teilchen, deshalb steht die Messung von Neutronendosisraten im Fokus dieser Arbeit. In dieser Arbeit wurde der Prototyp eines Phoswich-Detektors namens PING (**P**hoswich **I**nstrument for **N**eutrons and **G**ammas) entwickelt, um Neutronendosisraten in der Erdatmosphäre zu messen und von γ-Strahlung zu unterscheiden. Das Instrument besteht aus zwei verschiedenen Szintillatoren die optisch mit einander gekoppelt sind und von einem gemeinsamen Photomultiplier ausgelesen werden. Das Szintillatorpaket besteht aus einem inneren Plastikszintillator des Materials BC-412 und der umgebenden Antikoinzidenz aus natriumdotierten Cäsiumjodid (CsI(Na)). In dieser Arbeit wird das Instrument kalibriert, getestet und geflogen und es wird ein Verfahren zur Pulsformanalyse für dieses Instrument entwickelt, mit der es möglich ist Pulse vom Plastikszintillator und vom CsI(Na) zu unterscheiden. Die Pulse vom Plastikszintillator entstehen hauptsächlich durch Wechselwirkung mit Neutronen, aber es gibt eine energieabhängige Beimischung durch γ-Strahlung in diesen Ereignissen. Messungen der Dosisraten an Bord eines Flugzeuges zeigen, dass die mit dem entwickelten Detektor gemessenen Dosisraten in der gleichen Größenordnung liegen wie Ergebnisse anderer Instrumente. Bei Messungen an Bord von Stratosphärenballonen wird die Höhenabhängigkeit der Zähl- und Dosisraten bestimmt. Die Zählraten zeigen ein Maximum, welches sich mit der Position des Pfotzer-Maximums (Pfotzer, 1936) deckt. In den Dosisraten wurde ebenfalls ein Maximum gefunden, welches auch in Bartlett (2004) genannt wird.

Abstract

The Earth is constantly exposed to a stream of energetic particles from outer space. Through the interaction of this radiation with the Earth's magnetosphere and atmosphere a complex radiation field is formed which varies with the location inside the Earth's atmosphere. This radiation field consists of charged and uncharged particles leading to the constant exposure of human beings to radiation. As this ionizing radiation can be harmful for humans, it is necessary to perform dose rate measurements in different altitudes in the Earth's atmosphere. Due to their higher biological effectiveness the exposure to neutrons is more harmful than the exposure to γ-rays and charged particles, which is why the determination of neutron dose rates is the focus of this work. In this work the prototype of a Phoswich detector called PING (**P**hoswich **I**nstrument for **N**eutrons and **G**ammas) is developed to determine dose rates caused by neutrons in the Earth's atmosphere and to distinguish these from γ-rays. The instrument is composed of two different scintillators optically coupled to each other and read out by one common photomultiplier tube. The scintillator package consists of an inner plastic scintillator made of the material BC-412 and a surrounding anti-coincidence made of sodium doped caesium iodide (CsI(Na)). In this work the instrument is calibrated, tested and flown and a procedure for a pulse shape analysis for this instrument is developed. With this analysis it is possible to distinguish pulses from the plastic scintillator and pulses from the CsI(Na). The pulses from the plastic scintillator are mainly due to the interaction of neutrons but there is an energy-dependent contribution of γ-rays to these events. Measurements performed on board an airplane show that the dose rates measured with the developed detector are in the same order of magnitude as results of other instruments. During measurements on board stratospheric balloons the altitude dependence of count rates and dose rates is determined. The count rates show a maximum which corresponds to the location of the Pfotzer maximum (Pfotzer, 1936). In the dose rates a maximum is found as well, which has been mentioned in Bartlett (2004).

Contents

Chapter 1

Introduction

We as human beings are constantly exposed to ionizing radiation from various sources. One of these sources are cosmic rays. With his balloon-borne measurements in 1912 Viktor F. Hess was the first to find evidence that there is a source of ionizing radiation other than the terrestrial ones. He found that the intensity of this radiation, after decreasing when leaving ground, starts to increase with altitude (Hess, 1912). Today this increase is explained by the interaction of mainly galactic cosmic rays, arriving isotropically at the top of the Earth's atmosphere, with the constituents of the atmosphere. In this interaction process a complex radiation field consisting of charged and neutral particles is formed, where the neutral component is mainly composed of neutrons and γ-rays. This mixed radiation field is highly variable with respect to the position in the Earth's atmosphere and leads to the constant exposure of human beings to different intensities of ionizing radiation. In the interaction with the human body ionizing radiation imparts energy to the tissue, which may lead to the damage of living cells. Considering this fact, it becomes obvious that radiation exposure is potentially harmful for the human body and that it is necessary to quantify the radiation exposure at different locations in the Earth's atmosphere. A first step to do so is the determination of the absorbed dose, which is defined as the amount of energy imparted per mass.

When the dose rates in a mixed radiation field, such as the radiation field in the Earth's atmosphere are to be determined, it is important to differentiate between the different particle species because different types of radiation have a different potential to cause damage to the human body. That means if the same amount of absorbed dose is imparted to the body by different particle types, the degree of damage can be very different. To account for this effect, radiation is categorized according to its relative biological effectiveness (RBE). Especially for neutral particles like γ-rays and neutrons the

RBE differs significantly, which is the reason why it is very important to distinguish between these neutral particles and determine their contribution to the absorbed dose separately. However, while it is possible to differentiate between neutral and charged particles using an anticoincidence technique, it is not simple to distinguish between neutrons and γ-rays.
For the measurement of neutrons as well as for the determination of dose rates in the Earth's atmosphere several other instruments have already been developed. One of the best ways for neutron spectrometry is the use of Bonner spheres (see e.g. Thomas and Alevra, 2002). The disadvantage of this technique is that the setup of different Bonner spheres is not very well suitable as a portable device and for the use on board a stratospheric balloon. Two well established instruments for dosimetry in the Earth's atmosphere are the Tissue Equivalent Proportional Counter (TEPC) (description of a TEPC see e.g. European Commission, 1996 or Lindborg et al., 1999) and the dosimetry telescope DOSTEL (see e.g. Beaujean et al., 1999) but in both of these measurement techniques no distinction between different particle species is done.
The aim of this work is the development of an instrument which is able to measure fast neutrons in the mixed radiation field of the Earth's atmosphere and to develop a data analysis technique for the output of this detector in order to be able to distinguish neutrons from other particle types, especially γ-rays. One of the goals of this work is to build an instrument which is relatively small, lightweight and portable in order to make it suitable for the use in different locations such as e.g. aircraft or stratospheric balloons. In this work a prototype of such an instrument has been developed, which is called PING (**P**hoswich **I**nstrument for **N**eutrons and **G**ammas). The developed instrument is based on the so-called Phoswich technique where two or more dissimilar scintillators, which are optically coupled to one another, are read out by a common photomultiplier tube. One of the advantages of this technique is that the inner scintillator, which in this case is dedicated to measure fast neutrons, can be completely surrounded by an anticoincidence. In this work two different scintillator materials are used for the developed detector: a hydrogen rich plastic scintillator made of the material BC-412 as the inner scintillator and a sodium-doped caesium iodide (CsI(Na)) scintillator as the surrounding anticoincidence. While the inner scintillator is very sensitive to neutrons due to its hydrogen content, the CsI(Na) has a high cross section for γ-rays. Based on the fact that the two scintillators chosen for this instrument have different decay times concerning their light output, it is possible to distinguish the pulses from the two scintillators. In this work a procedure for a pulse shape analysis has been developed which allows to distinguish between the pulses from the plastic scintillator and the CsI(Na).

Structure of This Work

The following work is divided into nine chapters. Chapter 2 summarizes the theoretical background including particle interactions, basic information about scintillators and Phoswich detectors, a description of the radiation environment as well as some principles about dosimetry. In Chapter 3 the concept and development of PING is described while the data structure, data reduction and analysis is explained in Chapter 4. The calibration of the developed instrument with neutrons and γ-rays is shown in Chapter 5. In Chapter 6 test measurements as preparation for the balloon flights are described. The results of the measurements on board an aircraft are shown in Chapter 7, while Chapter 8 contains the results of the measurements of the balloon flights. Finally, Chapter 9 contains a summary and conclusions whereas Chapter 10 gives an outlook for future work.

Contribution of the Author

Note that the concept and design of the sensor head as described in Chapter 3 was done by the author, but the construction of the housing for the sensor head as well as the frame for the instrument and the transformation into a CAD drawing was done by L. Seimetz.
The development of the procedure for the data analysis technique, explained in Chapter 4, was performed in close collaboration with S. I. Böttcher, but the author participated in all steps of the development, especially the programming of the data analysis was done by the author.
All calibration measurements (Chapter 5), test measurements under low pressure and low temperature conditions (Chapter 6), the measurement on board the airplane (Chapter 7) as well as the measurement on board the stratospheric weather balloon (Chapter 8) were performed by the author alone and independently.
As indicated in Section 8.2, the measurement on board the BEXUS balloon was realized together with a group of students.

Chapter 2

Theoretical Background

This chapter gives an overview of the theoretical background of this work. It summarizes the particle interactions in matter, the different types of scintillators and the basics of a Phoswich detector including photomultiplier tubes. Finally an introduction to the radiation environment in the Earth's atmosphere and into the basic quantities of dosimetry is given.

2.1 Particle Interactions

2.1.1 Neutrons

The neutron, discovered by Chadwick in 1932, is the second constituent of the atomic nucleus apart from the proton. Its mass is slightly higher than that of protons and unlike the positively charged proton the neutron carries no charge. Therefore, neutrons do not interact with matter via the Coulomb force and as a result are able to travel through many centimeters of matter without undergoing any type of interaction. When an interaction does take place, it is with the nuclei of the absorbing material. Neutrons are not measured directly but via the secondary radiation they produce. In most cases these secondary particles are heavy charged ions. Neutrons can undergo a variety of different processes which include elastic scattering, inelastic scattering, neutron capture and other nuclear reactions. The cross sections for the various nuclear interactions of neutrons change significantly with the neutron energy E_n, therefore neutrons are usually classified according to their energy E_n in order to discuss their interaction properties separately. The boundaries between the different categories vary a lot between different authors. One possible definition is that neutrons with energies between a few hundred keV and a few ten's of MeV are called fast neutrons, whereas neu-

trons with energies above about 100 MeV are termed high energy neutrons (Leo, 1987). The Phoswich detector developed in this work is designed to detect fast neutrons up to 100 MeV only. For the detection of neutrons in this energy range the most important conversion process is the elastic scattering with nuclei. Inelastic scattering can also occur when the energy of the incident neutron is sufficiently high to excite a nucleus (this is in order of 1 MeV or more (Leo, 1987)). In case of scattering the secondary radiations are recoil nuclei. When inelastic scattering occurs the recoil nucleus is elevated to an excited state and may later decay by emitting a γ-ray. Compared to an equivalent elastic collision the neutron loses more of its energy in the inelastic collision.
In this work the most commonly used method to detect fast neutrons, which is the elastic scattering of neutrons by light nuclei (Knoll, 2000), is applied. For this purpose a tissue equivalent hydrogen rich organic scintillator is used. The main interaction mechanism for neutrons in this material is elastic scattering with hydrogen nuclei. In this interaction a fraction of the kinetic energy of the incoming neutron is transferred to the hydrogen nucleus, so the resulting secondary particle is a recoil proton. In Fig. 2.1 a schematic view of the neutron elastic scattering is shown for the center-of-mass system (left) as well as for the laboratory system (right).

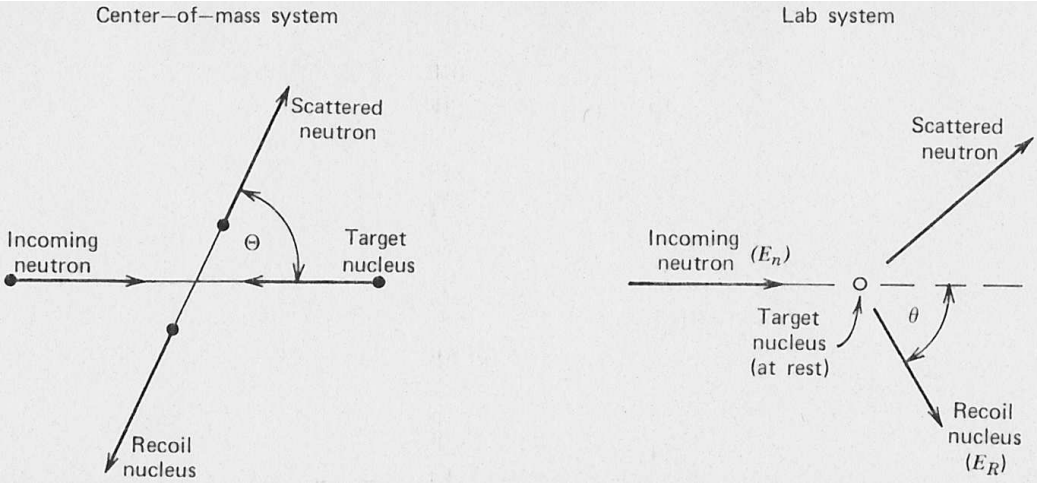

Figure 2.1: *Schematic view of neutron elastic scattering (taken from Knoll, 2000, Copyright 2000 John Wiley & Sons, Inc.; used with permission)*

To calculate the energy of the recoil nucleus the following definitions are used:

A : mass of the target nucleus
E_n : kinetic energy of incoming neutron (laboratory system)
E_R : kinetic energy of the recoil nucleus (laboratory system)
Θ : scattering angle of neutron (center-of-mass system)
θ : scattering angle of recoil nucleus (laboratory system)

In elastic scattering processes the kinetic energy before and after the reaction is the same by definition. Assuming that the target nucleus is at rest, the sum of the kinetic energies of the scattered neutron and the recoil nucleus must equal the energy of the incoming neutron. Considering incident neutrons with non-relativistic energies and taking into account the conservation of energy and momentum the following relation for the energy of the recoil nucleus is found for the center-of-mass system:

$$E_R = \frac{2A}{(1+A)^2}\ (1 - cos\ \Theta)\ E_n \tag{2.1}$$

The following transformation is used for the conversion from the center-of-mass system to the laboratory system:

$$cos\ \theta = \sqrt{\frac{1 - cos\ \Theta}{2}} \tag{2.2}$$

The combination of equation (2.1) and (2.2) results in the following expression for the energy of the recoil nucleus in the laboratory system:

$$E_R = \frac{4A}{(1+A)^2}\ (cos^2\ \theta)\ E_n \tag{2.3}$$

The maximum possible energy is transferred in a head-on collision where the scattering angle is θ=0:

$$E_{R,max} = \frac{4A}{(1+A)^2}\ E_n \tag{2.4}$$

For single scattering of neutrons with hydrogen nuclei the energy of the recoil proton can range between zero and the total energy of the incoming neutron, whereas in scattering with heavier nuclei only a smaller fraction of the neutron's energy can be transferred. For carbon as a target material,

for example, only a maximum of 28 % of the primary neutron energy is transferred.
When considering simple hydrogen scattering of neutrons some simplifying assumptions can be made (see Knoll, 2000) concerning the expected proton recoil energy distribution. In this simple case the detector response to a monoenergetic neutron is a simple rectangle ranging from zero to the full energy of the incoming neutron as shown in Fig. 2.2. The recoil energies for the scattering angles θ are indicated by the arrows. In this figure the energy of the recoil proton is denoted as E_p, which equals the quantity E_R used in equations (2.1) to (2.4). There are many effects that distort this

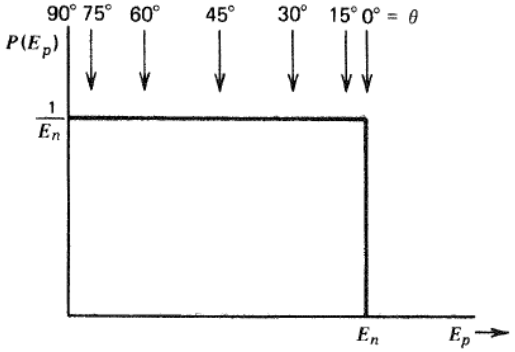

Figure 2.2: *Ideal form of the energy distribution of recoil protons produced by monoenergetic neutrons. The recoil energies for different scattering angles θ are indicated by the arrows (taken from Knoll, 2000, Copyright 2000 John Wiley & Sons, Inc.; used with permission)*

simple rectangular detector response including the nonlinear light output with respect to the deposited energy, the edge effect (meaning that recoil protons escape from the surface of the scintillator), multiply scattering from hydrogen, scattering from carbon and the detector resolution. Figure 2.3 displays how the different factors alter the detector response function. The nonlinearity of the light output and the edge effect lead to the fact that events are shifted to lower energies than they originally have, which results in the increase of events at lower energies seen in the upper panel of Fig. 2.3. Multiple scattering from hydrogen will results in an increasing number of events with larger amplitudes in comparison with events with smaller pulse heights. Scattering from carbon leads to an additional 'edge' in the detector response illustrated in the middle panel of Fig. 2.3 and the noise caused by different effects washes out the distinct shape of the response function which is shown in the lower panel of Fig. 2.3. For more information on the detector

response, on neutrons and neutron scattering please refer to Knoll (2000).

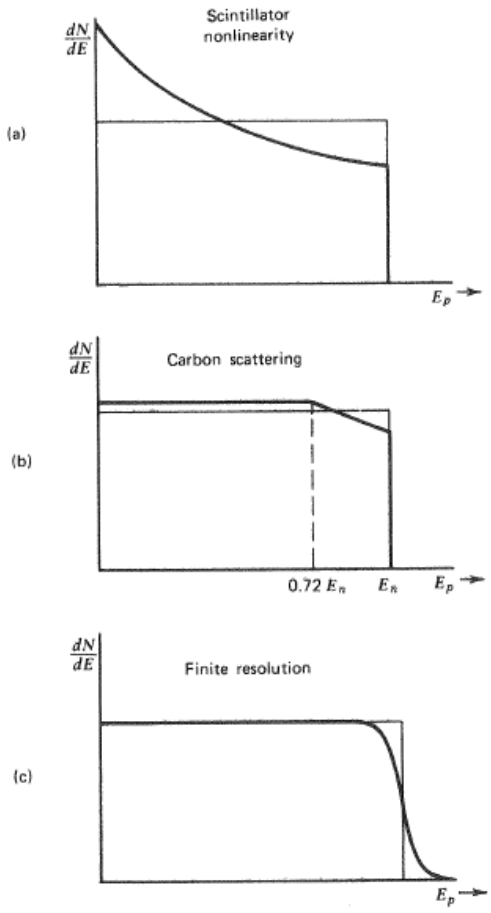

Figure 2.3: *Three different examples of the distortion of the rectangular recoil proton spectrum (taken from Knoll, 2000, Copyright 2000 John Wiley & Sons, Inc.; used with permission)*

2.1.2 Gamma Rays

Like neutrons, γ-photons are uncharged particles and they are measured via their secondary radiation. In the case of γ-rays the resulting secondary particles are electrons. The three most important interaction mechanisms for γ-rays in radiation measurements are photoelectric absorption, Compton scattering and pair production. While the photoelectric effect is the predominant process for low γ-ray energies up to several hundred keV, pair production is the most probable interaction mechanism for energies above 5

to 10 MeV. Compton scattering is the most prominent interaction process in the energy range between the two extremes.
In the photoelectric absorption process the incident γ-ray photon interacts with an atom of the absorber material. The γ-ray completely disappears and an energetic photoelectron is ejected from one of the electron shells of the absorbing atom. This photoelectron has the following kinetic energy:

$$E_{photo} = h\nu - E_b \tag{2.5}$$

with E_b the binding energy of the photoelectron. For photoelectrons originating from the K shell the binding energy ranges from a few keV to tens of keV depending on the atomic number Z of the material (Knoll, 2000).
After the emission of the photoelectron the atom is left with a vacancy in the electron shell. It is filled by capturing a free electron or electron rearrangement under the emission of the original binding energy in form of a characteristic X-ray or Auger electron. In most cases the X-ray is reabsorbed near the original interaction site by photoelectric interaction and the Auger electron has a very short range because of its low energy. If all secondary radiation produced in this interaction is absorbed and does not leave the detector, the sum of the kinetic energies of the secondary radiations equals the energy of the incident γ-ray. Thus, the process of photoelectric absorption with monoenergetic γ-rays leads to a single peak in the measured electron spectrum which corresponds to the total energy of the incoming γ-ray. The probability τ of photoelectric absorption per atom over all ranges of γ-ray energies E_γ and atomic numbers Z is approximately given by

$$\tau \approx const. \frac{Z^n}{E_\gamma^{3.5}} \tag{2.6}$$

with n between 4 and 5 (see Knoll, 2000).
Because of this strong dependence of the probability for this interaction mechanism on the atomic number Z, materials with a high atomic number are favoured for the detection of γ-rays.
In the Compton scattering process the incoming γ-ray photon is scattered by an electron of the absorbing material, creating a recoil electron and a scattered γ-ray photon. The kinetic energy of the recoil electron depends on the scattering angle θ and is given by

$$E_{e^-} = h\nu - h\nu' = h\nu \left(\frac{(h\nu/m_0c^2)(1 - \cos\ \theta)}{1 + (h\nu/m_0c^2)(1 - \cos\ \theta)} \right) \tag{2.7}$$

with the energy of the recoil electron E_{e^-}, the energy of the incident and scattered γ-ray photon $h\nu$ and $h\nu'$ and the rest mass energy of the electron

m_0c^2 (see Knoll, 2000). In case of head-on collision (angle $\theta = \pi$) the maximum possible energy is transferred to the recoil electron and equation (2.7) reduces to

$$E_{e^-}(\theta = \pi) = h\nu \left(\frac{2h\nu/m_0c^2}{1 + (2h\nu/m_0c^2)} \right). \tag{2.8}$$

Since all scattering angles are possible, the kinetic energy of the recoil electron can vary between zero and the maximum energy given by equation (2.8). In the measured electron spectrum a so-called *Compton continuum* is formed ranging from zero to the maximum energy. The high energy end of this continuum is called the *Compton edge*. The probability of Compton scattering per atom of the absorbing material increases linearly with the atomic number Z because it depends on the number of electrons of the absorber.
If the energy of the incident γ-ray photon is higher than twice the rest mass energy of the electron (1.02 MeV) the pair production process becomes possible. This interaction occurs in the Coulomb field of the nuclei of the absorbing material. While the incident γ-ray photon disappears in this process an electron-positron pair is created. All energy of the incoming γ-ray photon which exceeds the required 1.02 MeV for the creation of the pair is converted into kinetic energy which is shared by the electron and the positron. As the positron will annihilate, normally two annihilation photons with an energy of m_0c^2 each, are produced as secondary radiation in this interaction process. In the measured spectrum the process of pair production leads to a peak which is located $2m_0c^2$ below the energy of the incoming γ-ray photon. The probability of pair production per nucleus increases approximately with the square of the atomic number Z of the absorber material (Knoll, 2000).
To discuss the response of γ-ray detectors one differentiates between small, intermediate size and large detectors. These categories are defined by comparing the detector size with the mean free path of the secondary γ-rays produced by the interaction of the incoming γ-rays. The dimensions of a small detector do not exceed 1 or 2 cm (Knoll, 2000). The CsI(Na) scintillator used as an anti-coincidence in the developed Phoswich detector has a maximum thickness of 1 cm and falls into the category of a small detector. In the lower part of Fig. 2.4 the expected electron energy deposition spectra for a small size detector are shown for two cases: on the left side the incident γ-ray energies are less than the value at which pair production becomes possible and on the right side they are larger than this value. In the first case the resulting spectrum consists only of the *Compton continuum* with the *Compton edge* and the full energy peak, or *photopeak*, caused by photoelectric absorption. The spectrum in the second case features another peak caused by pair production. This peak is referred to as *double escape*

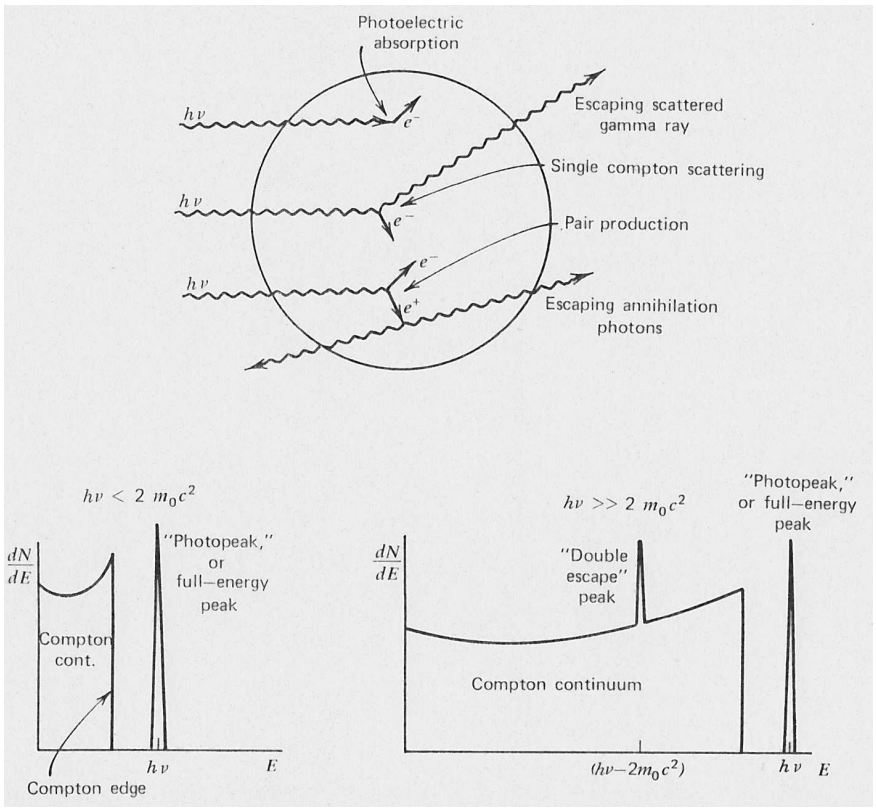

Figure 2.4: *Upper part: the three main interaction mechanisms for γ-rays in a small size detector. Lower part: the resulting electron energy deposition spectra with (left side) and without pair production (right side) (taken from Knoll, 2000, Copyright 2000 John Wiley & Sons, Inc.; used with permission)*

peak because in a small size detector only the kinetic energies of the electron and positron created in pair production are absorbed in the detector and the two annihilation photons leave the detector without any interaction.
Even though γ-ray spectroscopy is not the purpose of the CsI(Na) scintillator in the developed Phoswich detector, knowledge about the expected electron energy deposition spectra is needed for the evaluation of measurements with γ-rays sources which are used for the energy calibration of the CsI(Na).

2.1.3 Charged Particles

To discuss the energy loss of charged particles in matter they have to be divided into two categories: (a.) electrons and positrons and (b.) heavy charged particles which includes all particles which are heavier than electrons (Leo, 1987). The latter will be discussed first. Although different

interaction processes are known for heavy charged particles, the most important mechanism leading to energy loss in matter is the inelastic collision with atomic electrons of the absorbing material (Leo, 1987). The other process that frequently takes place is elastic scattering from nuclei but due to the usually small mass of the incident particle compared to the absorber nuclei, in this interaction not much energy is transferred.
When a heavy charged particle enters the absorber material it interacts via Coulomb forces with many electrons at the same time. In each of these interactions energy is transferred from the incident particle to the electron leading to either excitation or ionization of the absorber atoms. In each such encounter the incident particle loses energy and as a result it is slowed down. The maximum energy that can be transferred in a single collision is about 1/500 of the particle energy per nucleon (Knoll, 2000). This is a small amount of the total energy of the incident particle and thus the charged particle must undergo many of these interactions to lose its energy while passing through the absorbing material. By interacting with many electrons simultaneously at a given time, the heavy charged particle is decelerated continuously until it stops.
The average energy loss per unit path length is called the stopping power S and is described by the Bethe formula (Knoll, 2000):

$$S = -\frac{dE}{dx} = NZ\,\frac{4\pi e^4 z^2}{m_0 v^2}\left(ln\,\frac{2m_0 v^2}{I} - ln\left(1-\frac{v^2}{c^2}\right) - \frac{v^2}{c^2}\right) \tag{2.9}$$

N and Z are the number density and atomic number of the absorbing atoms, ze and v are charge and velocity of the primary particle, m_0 and e are the electron rest mass and the electron charge. The average ionization and excitation potential of the absorbing material I cannot be calculated easily and is thus determined experimentally for different materials. A list of values for I can be found in Leo (1987).
For incident charged particles with non-relativistic energies ($v \ll c$) only the first term in the brackets of equation (2.9) is significant. As this term varies slowly with the energy the general behaviour of dE/dx for non-relativistic particles can be described by the multiplicative factor which varies with $1/v^2$. This can be understood by noting that when the incident particle has a lower velocity it will spend more time in the vicinity of an electron of the absorber and thus the energy transfer from the incoming particle to the electron will be larger. This means for non-relativistic energies the energy loss of a heavy charged particle increases as its velocity decreases. This can be visualised with the so-called *Bragg curve*, where the energy loss is plotted versus the penetration depth (see for example Leo, 1987, chapter 2, Fig. 2.5).

This is only valid until the velocity of the incident particle approaches the speed of light. In this case a minimum in the energy loss is reached which lies at energies above several hundred MeV for heavy charged particles and at about 1 MeV for fast electrons. Relativistic particles in this minimum region are known as *minimum ionizing* particles.
For very low energies of the incident particle, when its velocity becomes comparable to the velocity of the atomic electrons, the Bethe formula begins to fail. In this case dE/dx reaches a maximum and then drops down. The reason for this behaviour is that at such low energies charge exchange between the incoming particles and the atomic electrons of the absorber becomes important. The positively charged particles will begin to pick up electrons which reduces their charge and leads to a smaller dE/dx.

Electrons and positrons may also lose energy through collision but due to their small mass an additional process becomes important: the energy loss through radiation. The collisional energy loss of fast electrons can be described by an expression similar to the Bethe formula given in equation (2.9), which takes into account that in case of fast electrons the incoming particle will be deflected in the collision process and that the incoming electrons are indistinguishable from the electrons of the absorber.
It is known from classical theory that whenever a charged particle is accelerated it emits radiation, the so-called *bremsstrahlung*, with a magnitude that is proportional to this acceleration. When a particle is scattered in the electric field of the absorber nuclei, it will be accelerated or decelerated and thus the energy loss through radiation happens in form of *bremsstrahlung* which is created along the track of the particle. Because the total *bremsstrahlung* per atom is inversely proportional to the square of the mass of the incident particle (Evans, 1955), only electrons and positrons will yield a significant amount of *bremsstrahlung* and thus only for these particles the energy loss through radiation becomes important. However, for electron energies of less than a few MeV, which is the energy range of secondary electrons from γ-ray interactions, energy loss by radiation is still a small fraction of the total energy loss (Knoll, 2000).

The range of a charged particle in matter is a concept describing the thickness of an absorber which the particle can just penetrate. For the range different definitions and values are used. For example a distinction can be made between the *mean range* and the *extrapolated range*, where *mean range* corresponds to the absorber thickness at which half of the initial charged particles are absorbed while the *extrapolated range* gives the thickness beyond which none of the initial particles can penetrate (Leo, 1987). In Berger

et al. (2005a) the *CSDA ranges* and *projected ranges* are given. These ranges are obtained by different calculation methods. *CSDA* stands for *continuous-slowing-down approximation* and a definition for the *CSDA range* can be found in Podgoršak (2010). The *projected ranges* are computed by considering the transport of the charged particles through the absorber including elastic scattering (see Berger et al., 2005a). For the *projected range* the sum of individual path length projected onto the incoming particle direction is used (Podgoršak, 2010). In this work the *projected range* is used to dimension the detector.

2.2 Scintillators

A scintillator is a material which produces light in the visible part of the electromagnetic spectrum when ionizing radiation interacts with it. In the scintillation process kinetic energy of the incident charged particles is converted into detectable light. The process of prompt emission of visible light by a material after its excitation is called fluorescence. There are two other processes which also lead to the emission of visible light, phosphorescence and delayed fluorescence, but these two processes involve a much longer emission time after excitation. A good scintillator material converts as much of the incident radiation energy as possible into prompt fluorescence. Other properties of an ideal scintillator would include the following (Knoll, 2000):

- High scintillation efficiency: The fraction of incident energy that is converted into detectable light should be high
- Linearity: The light yield of the scintillator should be proportional to the deposited energy over a wide energy range
- No self-absorption: The material should be transparent to the wavelength at which it emits light
- Short decay time: The induced luminescence should decay fast in order to generate fast signal pulses
- Good refraction index: To ensure efficient coupling of the scintillation light to a light sensor the refraction index of the scintillator should be near 1.5 (refraction index of glass)

Basically, there are two different types of scintillators: inorganic and organic scintillators. The most prominent inorganic scintillators are crystals made

from alkali halides like e.g. sodium iodide (NaI). Widely used organic scintillators are liquid and plastic scintillators. While inorganic scintillator have a higher light output and good linearity they are comparably slow in their response time. Organic scintillators on the other hand are much faster but yield less light. Since the scintillation process is different for both scintillator types, they are discussed separately in the following.

2.2.1 Inorganic Scintillators

Inorganic scintillators are usually crystals made form alkali halides which contain a small amount of impurities serving as an activator for the luminescence process. The scintillation mechanism in inorganic scintillators can best be described with the energy band structure of an activated crystal as shown in Fig. 2.5. An undoped crystal is represented by a valence band

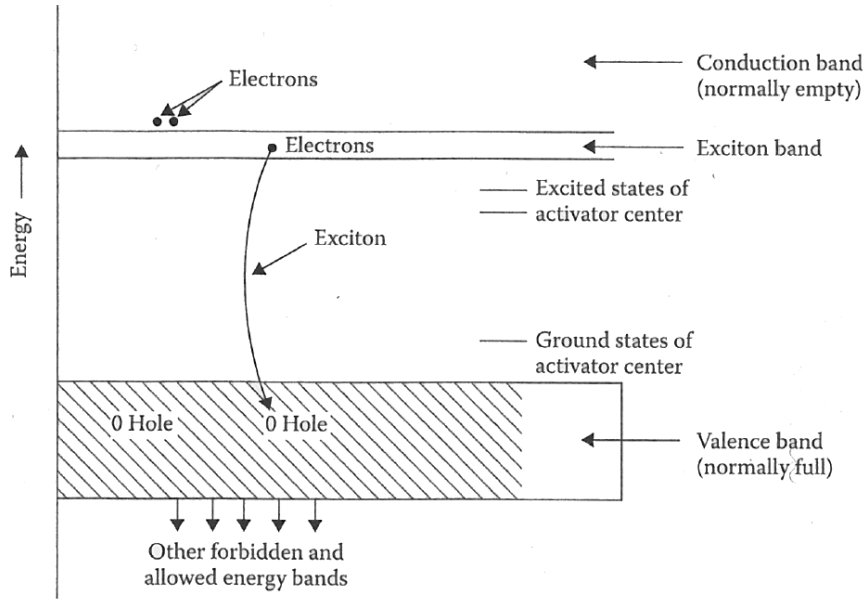

Figure 2.5: *Energy band structure of an activated crystal (taken from Tsoulfanidis and Landsberger, 2011, Copyright 2011 From Measurement and Detection of Radiation by N. Tsoulfanidis and S. Landsberger. Reproduced by permission of Taylor and Francis Group, LLC, a division of Informa plc.)*

and a conduction band of energies separated by the band gap. The valence band is associated with electrons that are bound to sites of the crystal lattice and this band is normally completely filled with electrons. The conduction band refers to electrons having enough energy to be free to move through

the crystal and this band is normally empty. The band gap is formed by the forbidden energy levels which cannot be populated in a pure crystal. The activator which is added to the crystal is chosen in such a way that it creates additional energy levels within the forbidden band gap. This includes the activator's ground state and the associated excited states (see Fig. 2.5).
As a charged particle passes through the crystal either ionization or excitation will take place. In ionization the incident particles transfers sufficient energy to an electron in the valence band to raise it into the conduction band creating a vacancy in the valence band called a hole. The electron in the conduction band as well as the hole in the valence band can move through the crystal freely. In case of excitation less energy is transferred from the incident particle to the electron in the valence band and an electron-hole pair is created which is still electrostatically bound together. This is called exciton and it corresponds to an elevation of the electron to an energy level in the so-called excitation band. The upper level of this thin band coincides with the lower level of the conduction band (see Fig. 2.5).
The transition from an electron in the conduction band back to the valence band does not lead to the emission of scintillation light because the typical band gap is too large to result in a photon in the visible range. For scintillation light to be created first energy has to be transferred from the host crystal to the activator in order to excite the activator. An activator atom is raised to one of its excited states through the absorption of an exciton or the successive capture of an electron and a hole. If the transition of the activator from the excited state to its ground state is allowed and the result is a photon with a wavelength in the visible range of the electromagnetic spectrum this contributes to the scintillation. Thus, it is the transition of activator atoms rather than the excitation and de-excitation of crystal atoms which results in the light emitted by an inorganic scintillator.

2.2.2 Organic Scintillators

Organic scintillator materials are aromatic compounds which consist of planar molecules formed by benzenoid rings and are available as monocrystals, liquid or plastic scintillators. A plastic scintillator can be regarded as a solid solution of organic scintillators. It is produced by dissolving organic scintillators in a solvent which is then polymerized. The plastic scintillator used in this work is based on polyvinyltoluene.
In contrast to the scintillation process in inorganic crystals, which requires the regular crystalline lattice, the fluorescence process in organic scintillators is the result of transitions within individual molecules. Thus, the scintillation process in organic scintillators is independent of its physical state.

Many organic scintillators in practical use today are based on organic molecules which feature the so-called π-electron structure shown in Fig. 2.6. The scintillation process in organic scintillators can be explained using this energy level structure in organic molecules. As displayed in Fig. 2.6 singlet (spin 0)

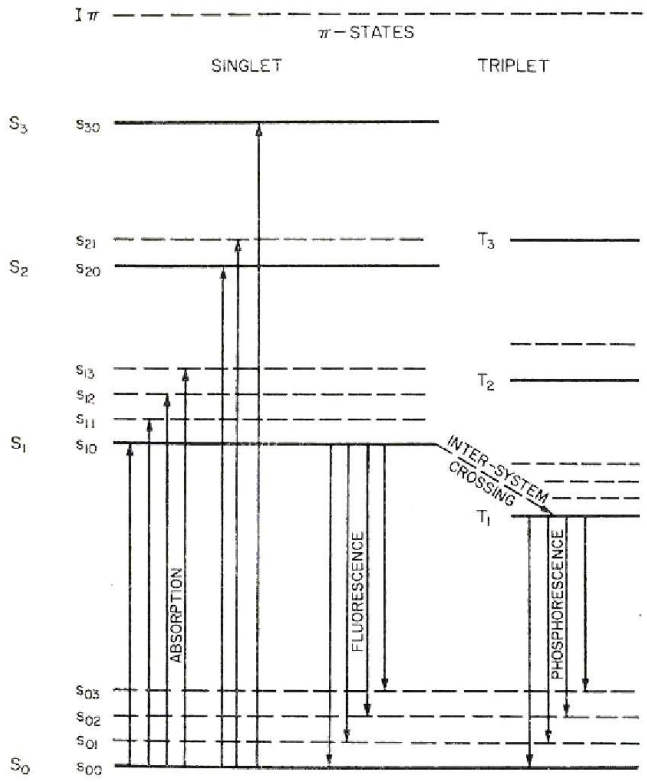

Figure 2.6: *Schematic view of the energy level structure of an organic molecule with π-electron structure (Reprinted from Birks, 1964, Copyright (1964), with permission from Elsevier)*

and triplet states (spin 1) are possible for the electron configuration of the molecule, but for the prompt fluorescence only the singlet states play a role. The state S_0 corresponds to the ground state of the molecule whereas S_1, S_2 and S_3 represent excited states. Each of these states is subdivided into many vibrational states which are denoted by a second subscript. Thus, the lowest ground state of the molecule is S_{00} and the lowest excited state is S_{10}.
When energy is absorbed by the molecule, for example by the kinetic energy of a charged particle, the electron configuration is raised to one of the excited states. This transition is indicated by the arrows labeled with 'Absorption' in Fig. 2.6. The higher excited states as well as the associated vibrational states with excess energy are populated only for a comparably short time and

thus the overall effect of exciting a molecule is the transition of the molecule from the S_0 to the S_{10} state. The de-excitation from this lowest excited state to one of the ground states results in prompt fluorescence and thus scintillation. This process is indicated by the arrows 'Fluorescence'. When comparing the absorption and the fluorescence process in Fig. 2.6 it becomes clear that organic scintillators can be transparent for their own scintillation light because the energy released in the de-excitation is always smaller than the minimum energy required for excitation (expect for the direct excitation from S_{00} to S_{10}).
It is desired that the scintillation efficiency, which is the fraction of incident energy that is converted into scintillation light, is as high as possible. Unfortunately, other de-excitation modes exist for the molecule which do not involve the emission of scintillation light. In these processes the excitation energy is mainly converted into heat. All processes involving radiationless de-excitation are summarized under the term *quenching*.
For further information see Knoll (2000) and Brooks (1979). The latter gives a very detailed description on the scintillation process in organic scintillators.

2.3 Phoswich Detectors

In this work a so-called *Phoswich detector* is developed. This type of detector consists of at least two dissimilar scintillators which are optically coupled to one another and to a common photomultiplier tube (in the following referred to as PMT). To be able to distinguish the pulses from the different scintillators usually materials with very different decay times of their light output are chosen and the data are analysed via pulse shape analysis. This technique is also applied in this work and will be discussed in detail in Chapter 3 and Chapter 4. The PMT is used to detect as well as amplify the light emitted by the scintillators. It also converts the detected light into a current pulse which is then analysed by the read-out electronics. In the following section the functional principle of a PMT is described.

2.3.1 Photomultiplier Tubes

A photomultiplier tube is an evacuated tube usually made of glass which consists of the following components: an entrance window, the photocathode, focusing electrodes, an electron multiplier made of a number of electrodes called dynodes and an anode. The PMT shown in Fig. 2.7 is a head-on type with a linear-focused dynode structure. The processes through which the PMT converts the incident light into a current pulse can be explained as fol-

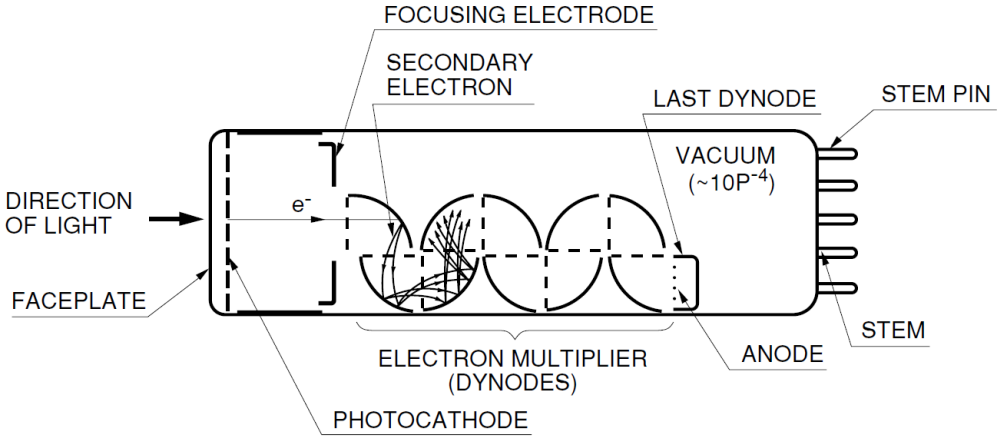

Figure 2.7: *Principle sketch of a photomultiplier tube (taken from Hamamatsu/PMT-handbook, 06.01.2013, Copyright 2006 Hamamatsu Photonics K. K.; used with permission)*

lows: The light enters the PMT through the entrance window and interacts with the photocathode. The incident light excites electrons in the photocathode which then migrate to the surface and are emitted into the vacuum, in case they have enough energy to overcome the potential barrier between the material of the photocathode and the vacuum. This process is know as *external photoelectric effect*. The focusing electrodes accelerate and focus the emitted photoelectrons so that they reach the first dynode. Initially the kinetic energy of the photoelectrons is very low but the dynodes are held at a high positive potential, so that the photoelectrons gain considerable energy in the acceleration between the dynode stages. The dynodes are made of a substrate electrode and a coating on the surface which consists of a secondary emissive material. These special materials chosen for the dynodes allow that the energy deposited by the accelerated electrons results in the reemission of more than one secondary electron from the surface of the dynode. The process of secondary electron emission can be compared to the emission of photoelectrons, the difference is that in the case of secondary electrons the electrons of the dynode are excited by energetic electrons rather than photons. At each of the dynode stages the multiplication of the photoelectrons is repeated. Finally the secondary electrons emitted from the last dynode are collected by the anode which outputs the electron current to an external circuit (see Hamamatsu/PMT-handbook, 06.01.2013). The PMT used for the developed Phoswich detector in this work is the PMT R5070A produced by Hamamatsu (see Hamamatsu/R5070A, 21.09.2012), which is a compact

head-on type PMT with a 10-stage linear-focused dynode structure.
For more detailed information on photomultiplier tubes please refer to Hamamatsu/PMT-handbook (06.01.2013).

2.4 Radiation Environment in Near Earth's Space

Cosmic rays were discovered by Victor F. Hess in 1912 during seven manned balloon flights. His measurements with electrometers showed that after the intensity of ionizing radiation decreased when leaving the ground, it started to increase with altitude (see Hess, 1912). The decrease of the ionizing radiation could be explained by the absorption of the terrestrial radiation in air but the subsequent increase was unexpected. Since Hess did not find any difference in the measurements between day and night time he could rule out the Sun as the source of the additional radiation.
Today we know that the increase in ionizing radiation he measured is caused by the interaction of cosmic rays with the constituents of the Earth's atmosphere, leading to the complex radiation field of secondary cosmic rays in the atmosphere which consists of charged and neutral particles.

2.4.1 Galactic Cosmic Rays

Galactic cosmic rays are highly energetic fully ionized particles with a composition of ~ 98 % nuclei and ~ 2 % electrons and positrons. The nuclear component is divided into ~ 87 % hydrogen, ~ 12 % helium and ~ 1 % heavier nuclei (Simpson, 1983). Galactic cosmic rays have energies of 10^7 eV up to 10^{20} eV with a maximum at around 1 GeV and are accelerated by the first-order Fermi mechanism in shock fronts arising in supernova explosions (for further details see e.g. Simpson, 1983; Hörandel, 2008, the latter gives a more detailed description on the origin of galactic cosmic rays).
On their way to the Earth's atmosphere the galactic cosmic rays are influenced both by the heliospheric magnetic field as well as by the terrestrial magnetic field. These influences is discussed briefly in the next two sections.

2.4.2 Modulation by the Heliospheric Magnetic Field

The heliosphere is the local plasma bubble in which our solar system is embedded. It is formed when the solar wind, a permanent stream of ionized particles which flows radially away from the Sun, interacts with the local

interstellar medium. The Sun is a magnetic star and as the magnetic field is frozen into the solar wind it is carried outwards into the heliosphere. A global magnetic structure is created within the heliosphere which is called the heliospheric magnetic field.
The galactic cosmic rays arrive nearly isotropically at the heliosphere but on their way to Earth their intensity is modulated by the heliospheric magnetic field. Various processes contribute to the modulation such as scattering, drift effects, convection and adiabatic deceleration. For further details on the mechanisms of the modulation of galactic cosmic rays in the heliosphere see e.g. Potgieter (1998) and references therein and for the implication of the modulation see e.g. Heber (2001); Heber et al. (2009).
The intensity of the solar wind and therefore the strength of the heliospheric magnetic field depends on the activity of the Sun which follows an 11-year-cycle. Depending on the strength of the heliospheric magnetic field the intensity of galactic cosmic ray particles below a few GeV/nucleon is altered. Figure 2.8 shows the unmodulated spectrum of cosmic ray protons as well as the modulated spectra for solar minimum (red curve) and solar maximum conditions (blue curve). The unmodulated spectrum is denoted by LIS which stands for Local Interstellar Spectrum. This figure clearly shows that the modulation of the spectrum is stronger during solar maximum. Thus,

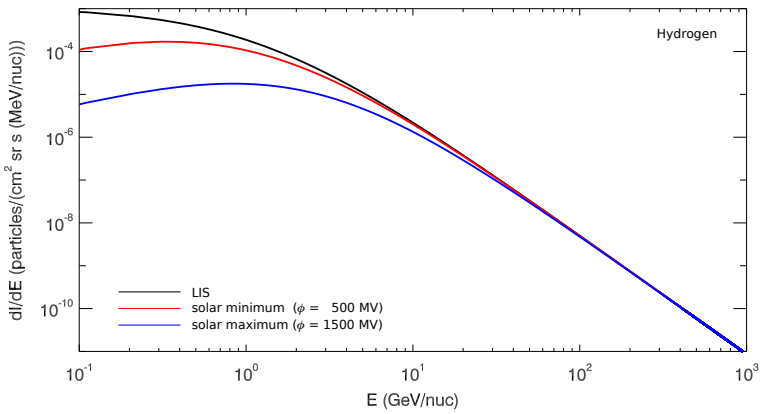

Figure 2.8: *Differential intensity spectra for galactic cosmic ray protons: the unmodulated spectrum called LIS (Local Interstellar Spectrum) shown in black and the modulated spectra for solar minimum (red) and solar maximum conditions (blue) (Herbst, 2013)*

the heliospheric magnetic field serves as a shielding for the Earth against incoming galactic cosmic rays. During solar maximum, when the solar activity

is high, the strong heliospheric magnetic field leads to a stronger modulation of the galactic cosmic rays. This results in a lower flux of galactic cosmic rays at Earth. During solar minimum the situation is vice versa. Figure 2.9 shows the anti-correlation between the galactic cosmic rays at Earth and the solar activity. The red curve represents the count rates per second of the Kiel neutron monitor which serve as a measure for the intensity of galactic cosmic rays at Earth (for information on the use of neutron monitors to determine the intensity of galactic cosmic rays on Earth please refer to Simpson, 2000). The green curve shows the observed monthly sun spot numbers during the same time period. Sun spots are known to be regions of the Sun with a high magnetic activity, thus a high number of sun spots corresponds to high solar activity. When comparing the red and the green curve in Fig. 2.9 it becomes evident that the intensity of galactic cosmic rays on Earth is anti-correlated to the solar activity.

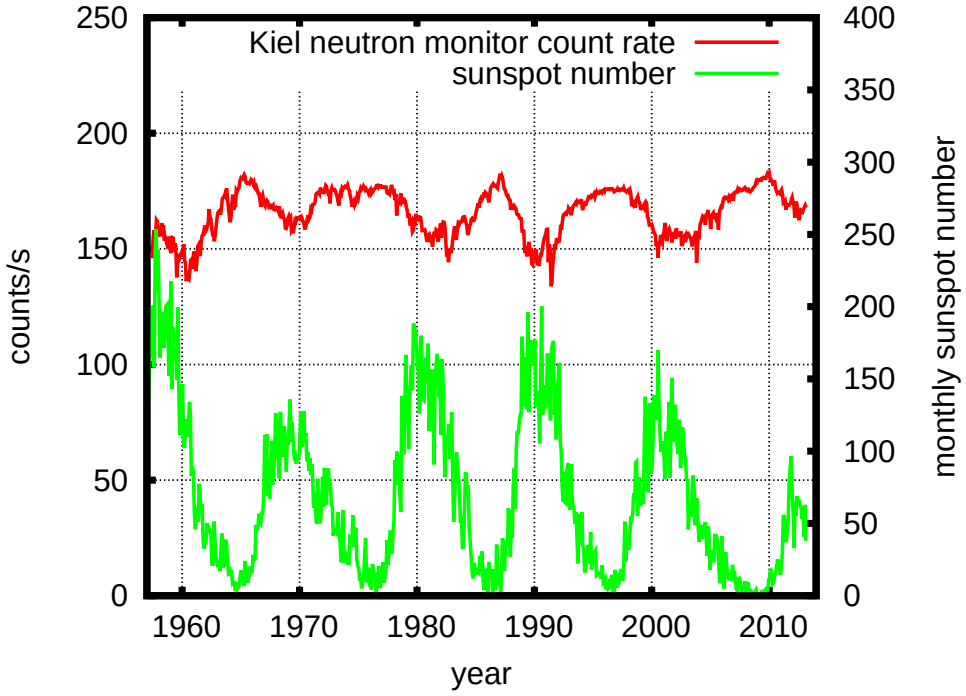

Figure 2.9: *The red curve shows the count rates per second from the Kiel neutron monitor (data taken from NMDB, 27.03.2013) as a measure for the galactic cosmic ray intensity at Earth and the green curve shows the observed monthly sun spot numbers (data taken from SIDC-team, 1957-2013) as a measure for the solar activity*

2.4.3 Influence of the Earth's Magnetic Field

Before a galactic cosmic ray particle finally reaches the Earth's atmosphere it has to penetrate the Earth's magnetic field first. However, charged particles which enter a magnetic field are deflected by the Lorentz force. The ability of a charged particle to penetrate a magnetic field is given by its rigidity which is represented by its momentum divided by its charge. For each position in the Earth's magnetosphere and each direction to this position a rigidity threshold exists. Particles with a momentum per charge less than this threshold cannot reach the given position. This threshold is called the *geomagnetic cutoff rigidity* because a spectrum of incoming particles will be 'cut off' below the energy corresponding to this threshold. For particles arriving at the Earth from vertical direction the cutoff rigidity is highest near the equator where the particles move perpendicular to the magnetic field lines. The lowest cutoff rigidities are found near the magnetic poles where the particles' motion is parallel to the magnetic field lines.
This is illustrated in Fig. 2.10 which displays the cutoff rigidities for incoming particles from the vertical direction at an altitude of 20 km (see Herbst, 2012). For the computation the so-called backward-trajectory tracing method was used. Figure 2.10 shows that the highest cutoff rigidities are found over India whereas the values found at the poles are so low that almost all incoming charged particles can penetrate the Earth's magnetic field.
The latitude dependence of the galactic cosmic ray particle flux is a direct consequence of the geomagnetic cutoff. An increased particle flux is found for increasing geomagnetic latitudes.

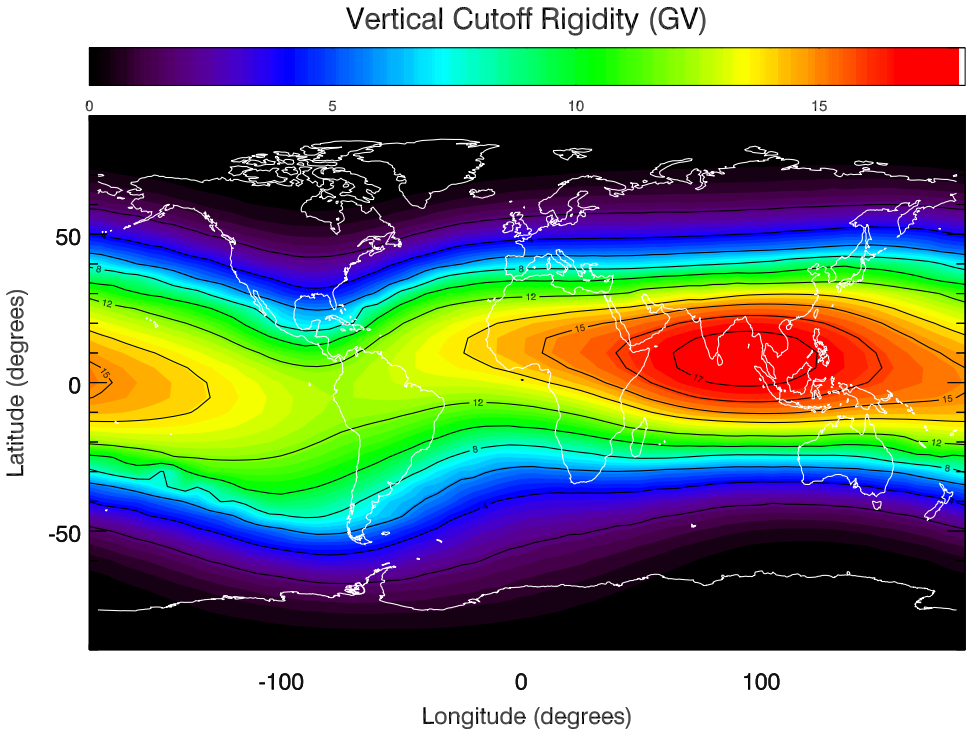

Figure 2.10: *Computed vertical cutoff rigidities at an altitude of 20 km (taken from Herbst, 2012)*

2.4.4 Secondary Cosmic Rays

Once galactic cosmic rays reach the Earth's atmosphere they interact with molecules and atoms of the atmosphere leading to a complex interaction cascade. Since nitrogen and oxygen are the most abundant constituents of the Earth's atmosphere, a typical first interaction is that of a galactic cosmic ray proton with a nitrogen or oxygen nucleus. In such a collision nucleons and mesons, mainly pions are emitted as the first secondary particles. The target nuclei are highly excited in these interactions and de-excite under the emission of neutrons and protons as well as light nuclei, mainly α-particles. If the energy of the primary proton is high enough it will continue to interact with other targets in the atmosphere. The high energy secondary particles also undergo further interactions.
The heavy nuclei of the galactic cosmic rays will be fragmented when interacting with the Earth's atmosphere. This happens at higher altitudes than the first interaction for protons because of the short interaction length for heavy nuclei.

Figure 2.11 shows the development of an interaction cascade in the Earth's atmosphere for a single proton impinging on the top of the atmosphere. As

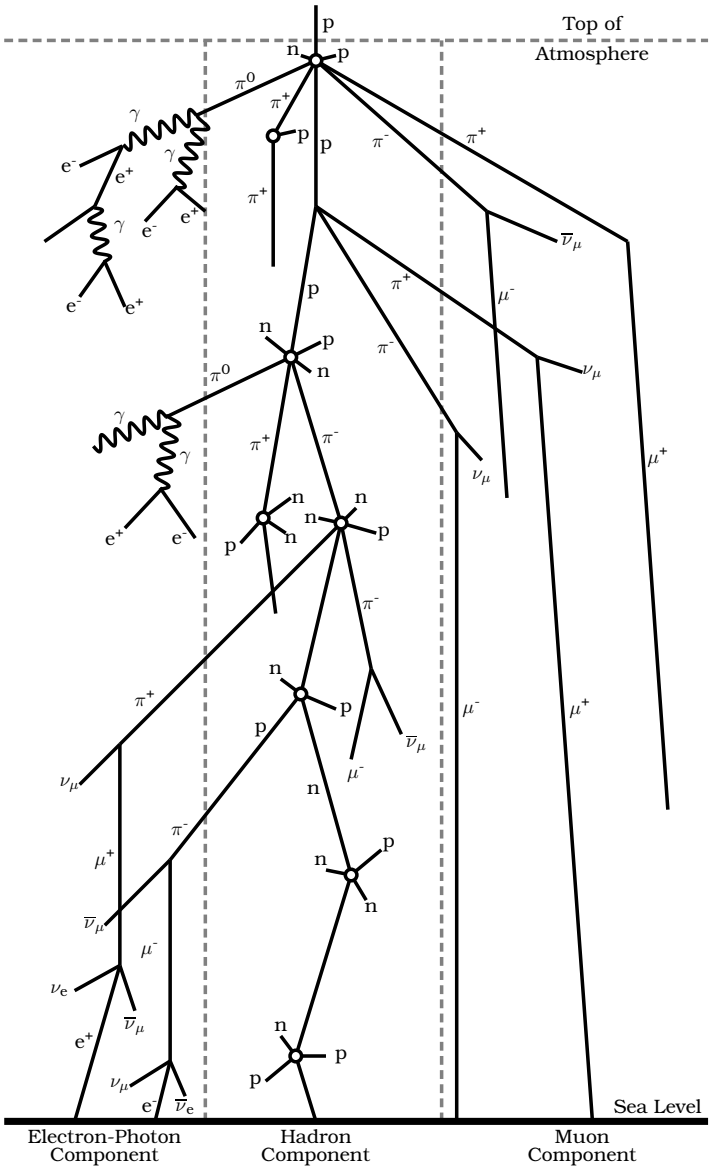

Figure 2.11: *Schematic view of the development of a cascade in the Earth's atmosphere at the example of a galactic cosmic ray proton with a nucleus of the Earth' atmosphere (Reprinted from Grieder, 2001a, Copyright (2001), with permission from Elsevier)*

displayed one can distinguish between three different components of the cas-

cade: the electron-photon (also know as the electromagnetic) component, the hadronic component and the muon component. The above described interactions lead to the development of the hadronic cascade which consists mainly of protons, neutrons as well as pions. For the development of the other two components of the cascade the creation of neutral and charged pions in the hadronic component is very important.
The neutral pions trigger the development of the electromagnetic component. They decay under the emission of two energetic γ-rays which then interact mostly via pair production. The produced electrons and positrons further interact producing bremsstrahlung. This leads to the development of the electromagnetic component which consists of electrons, positrons and γ-rays.
The muon component results from the decay of charged pions. Muons have a very short life time of only 10^{-6} s but because of their relativistic velocities they are able to reach sea level before they decay and thus contribute to the radiation field at sea level. Some of the muons do decay in the atmosphere and their decay products are neutrinos, electrons and positrons which then contribute to the electron-photon component. For more detailed information on the development of the interaction cascade in the Earth's atmosphere see e.g Allkofer (1975); Allkofer and Grieder (1983).
The above described production of secondary cosmic rays in the Earth's atmosphere leads to an increased particle flux with increasing atmospheric depth. After reaching a maximum at about 20 km the particle flux decreases again. This maximum of ionizing radiation was first discovered by Pfotzer (Pfotzer, 1936) and is called *Pfotzer maximum*. Above this maximum the production of secondary particles predominates whereas below this maximum decay and absorption processes dominate over the production of secondaries. For this work the secondary neutrons produced in the hadronic component of the cascade are of special interest. The neutrons produced in the Earth's atmosphere can be divided into low energy and high energy neutrons according to the processes by which they are created. Low energy neutrons have less than 10 MeV and they are created in the nuclear evaporation of excited atmospheric nuclei. High energy neutrons are produced in peripheral collisions and in charge exchange reactions (see Grieder, 2001b). Figure 2.12 shows a measured and a computed neutron spectrum at an altitude of 12 km in the Earth's atmosphere. Shown here is the differential intensity versus the neutron energy. The energies go up to 100 GeV but the intensity decreases rapidly with increasing energy.

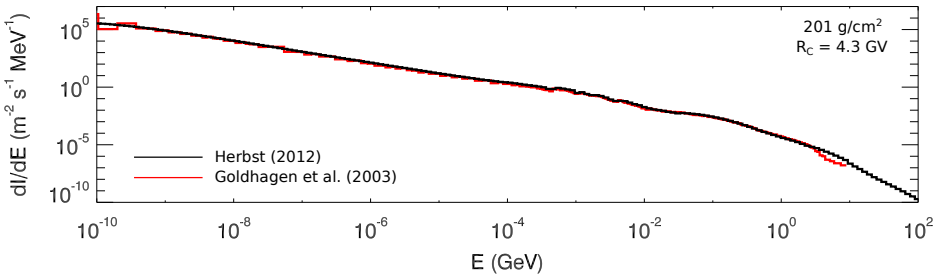

Figure 2.12: *Measured and computed neutron spectrum at an altitude of 12 km (Herbst, 2013), (measured data see Goldhagen et al., 2003)*

2.4.5 Solar Cosmic Radiation

Apart from the solar wind, which is constantly emitted from the Sun, so-called Solar Energetic Particle Events (SEPs) occasionally happen. These SEPs are associated with outbursts of electromagnetic radiation from the Sun and sometimes energetic particles are accelerated to more than 1 GeV. If the source of these particles is magnetically well connected to the Earth these particles lead to a high energy particle flux in the upper atmosphere of the Earth. However, an SEP which is well connected and produces such high energy particles that these can be measured on ground (so-called Ground Level Events (GLEs)) is very rare. During the measurements taken in this work no GLE happened, thus the solar energetic particle component can be neglected.

2.5 Dosimetry

The field of dosimetry deals with the measurement of ionizing radiation in matter and tissue. This is of great importance because human beings do not have an organ to sense radiation despite the fact that exposure to radiation can be very harmful for humans. When exposed to radiation living cells can be damaged because through the interaction of ionizing radiation the DNA may be altered leading to cell death or mutation of the cell. Especially an imperfectly repaired damage may result in cancer.
This section introduces basic dose and dose related quantities as they are defined by the International Commission on Radiation Units and Measurements (ICRU) in their report 84 (ICRU, 2010) and the International Commission on Radiological Protection (ICRP) in their publications 60, 92 and 103 (ICRP, 1991, 2003, 2007). Furthermore the importance of neutrons in dosimetry and

their contribution to the dose in different altitudes in the Earth's atmosphere is discussed.

2.5.1 Basic Quantities in Dosimetry

The basic physical quantity describing the effect of ionizing radiation on matter is the *absorbed dose* D which is defined as (ICRU, 2010):

$$D = \frac{\mathrm{d}\bar{\epsilon}}{\mathrm{d}m} \tag{2.10}$$

with $\mathrm{d}\bar{\epsilon}$ the mean energy imparted to matter of mass $\mathrm{d}m$ by ionizing radiation.
The unit of the absorbed dose D is gray (Gy) which is J/kg. Absorbed dose is used independently from the type of ionizing radiation and it provides an average value of the energy absorbed within the mass $\mathrm{d}m$. Because ionizing radiation imparts energy to a material by the interaction of charged particles with single molecules or atoms, the energy transferred to the mass $\mathrm{d}m$ will not be equally distributed. It may rather vary significantly within $\mathrm{d}m$ depending on the type of radiation, which is due to their different ionization density. This is not taken into account in the quantity of absorbed dose. However, when the influence of ionizing radiation on tissue is of concern, it is important to account for the effect that different types of radiation cause different distributions of energy within the mass $\mathrm{d}m$, because this may decide if and how much dose is delivered to an individual cell. To account for the effects of different radiation types on tissue the quantity *dose equivalent* H is introduced. It is defined as the absorbed dose D at a point in tissue multiplied by a dimensionless *quality factor* Q at that point (ICRU, 2010):

$$H = Q \cdot D = \int Q(L) D_L dL \tag{2.11}$$

where D_L is the distribution of the dose D in the linear energy transfer (LET) L and $Q(L)$ the quality factor as a function of L in water. The unit of H is also J/kg, but to distinguish dose equivalent H from absorbed dose D the unit for H is named sievert (Sv).
The linear energy transfer (LET) L is defined as the radiation energy loss of charged particles per unit length of a path through matter (ICRP, 2007):

$$L = \frac{dE}{dl} \tag{2.12}$$

with the mean energy dE which is lost by a charged particle due to interaction with the target material and dl the distance in matter which the particle traverses. L has the unit J/m but it is usually given in keV/μm.
The quality factor Q is defined depending on the linear energy transfer (LET) L of charged particles in water (ICRP, 2007):

$$Q(L) = \begin{cases} 1 & L < 10 \text{ keV}/\mu\text{m} \\ 0.32 \cdot L - 2.2 & 10 \text{ keV}/\mu\text{m} \leq L \leq 100 \text{ keV}/\mu\text{m} \\ \frac{300}{\sqrt{L}} & L > 100 \text{ keV}/\mu\text{m} \end{cases} \tag{2.13}$$

The factor $Q(L)$ has been introduced to characterise the biological effectiveness of different types of radiation. This difference in the biological effectiveness originates from the different ionisation density along the tracks of charged particles (ICRP, 2007).
For charged particles which are directly ionizing particles it is possible to measure the linear energy transfer L and thus calculate the corresponding quality factor Q. For indirectly ionising radiation such as photons and neutrons it is rather complicated to measure L and to determine the resulting Q because all secondary radiation which is created in the interaction with matter has to be taken into account.
In the field of dosimetry two different types of quantities exist. The above defined quantity dose equivalent H is a so-called operational quantity which is a measurable quantity. On the other hand there are protection quantities which are not directly measurable (see e.g. European Commission, 1996). In addition to the dose equivalent H the ICRP recommended a new quantity for radiation protection in their publication 60 (ICRP, 1991) which is called *equivalent dose* H_T:

$$H_T = \sum_R w_R \cdot D_{T,R} \tag{2.14}$$

with H_T the equivalent dose in tissue or organ T, w_R the dimensionless radiation weighting factor for radiation R and $D_{T,R}$ the average absorbed dose due to radiation R in tissue T.
Unlike the quality factor $Q(L)$ which depends on the linear energy transfer L describing the effect of the radiation in matter, the radiation weighting factor w_R is defined based on quality and type of the external radiation field. The quantity H_T as a so-called protection quantity is used to define dose limits in radiation protection. This quantity is in principle immeasurable because for its determination it is necessary to subdivide the absorbed dose into all the different components $D_{T,R}$ and relate them to the corresponding component of the external radiation field in order to multiply them with the appropriate radiation weighting factor w_R. Nevertheless a comparison of $Q(L)$ and w_R

is helpful for the determination of the dose equivalent H for neutrons and γ-rays. For photons and neutrons a mean quality factor $\bar{Q}$ (definition see ICRP (1991)) can be determined which was found to give consistent values with the radiation weighting factors w_R. In fact, especially for neutrons, the radiation weighting factors w_R were chosen so that they essentially agree with the values of $\bar{Q}$ (ICRP (2003); note that in this publication $\bar{Q}$ is named q^*). The ICRP publication 92 (ICRP, 2003) also states that w_R was introduced to serve as a simplified concept to replace the quality factor $Q(L)$ in practice and that it was intended that w_R is largely consistent with $Q(L)$. Thus, the radiation weighting factors w_R recommended in ICRP (1991) may be used as an approximation of the quality factors $Q(L)$ for photons and neutrons. They are summarized in table 2.1. For a detailed description of the concepts of $Q(L)$ and w_R and the comparison of these two factors please refer to the ICRP publication 92 (ICRP, 2003), especially to chapter 4.

The selection of both the quality factors and the radiation weighting factors

Type of Radiation	Radiation Weighting Factor w_R
photons (all energies)	1
neutrons $<$ 10 keV	5
neutrons 10 keV to 100 keV	10
neutrons $>$ 100 keV to 2 MeV	20
neutrons $>$ 2 MeV to 20 MeV	10
neutrons $>$ 20 MeV	5

Table 2.1: *Radiation weighting factors w_R as recommended by the ICRP (ICRP, 1991)*

is based on the relative biological effectiveness (RBE) of the different radiation types which is determined experimentally and is correlated with the linear energy transfer L. The linear energy transfer is used to characterize the properties of energy deposition along a track of a charged particle and ionizing radiation can be divided into low-LET radiation, such as photons and electrons, and high-LET radiation including secondary charged particles from neutron interaction and α-particles. As listed in table 2.1 low-LET radiation is associated with lower radiation weighting factors, and thus lower biological effectiveness, than high-LET radiation. For a more detailed description of the quantities introduced in this section refer to ICRP (1991, 2003, 2007), ICRU (2010) and references therein.

Neutrons can be more harmful to tissue than for example photons, because neutrons belong to the high-LET radiation, which is expressed by rather high values of w_R, depending on the energy of the neutron. Thus, it is clear, that

it is important to carefully distinguish between neutrons and for example γ-rays when the dose in a mixed radiation field is to be determined.
The absorbed dose D is the quantity which can be measured with the instrument developed in this work. To calculate the dose equivalent H knowledge about the primary neutron energy is required. This information could be gained from unfolding the measured energy deposition spectra of the instrument using a technique developed in the dissertation of J. Köhler (Köhler, 2011) but this is beyond the scope of this work.

2.5.2 Contribution of Neutrons to the Dose in the Earth's Atmosphere

Human beings are always exposed to ionizing radiation originating from natural sources. One of the contributors to the natural radiation exposure is the cosmic radiation discussed in Section 2.4. The other main source are terrestrial radionuclides which exist everywhere in the environment: in the Earth's crust, in air, water, food, building materials for houses and even inside the human body. Among these terrestrial sources radioactive radon gas and its decay products play an important role as these contribute significantly to the natural radiation exposure. The worldwide average dose per person from natural sources is 2.4 mSv per year (UNSCEAR, 16.01.14a).
Table 2.2 lists the fractions to which the different natural radiation sources

Source	Worldwide average annual effective dose [mSv]
cosmic rays	0.4
terrestrial gamma rays	0.5
inhalation (mainly radon)	1.2
ingestion	0.3
total	2.4

Table 2.2: *Average dose values caused by natural radiation (UNSCEAR, 16.01.14a)*

contribute to the total annual average dose given in effective dose E. Effective dose E is another protection quantity which is defined as the sum of the equivalent doses H_T for all tissues and organs of the body each weighted with a tissue weighting factor w_T (for the definition of E and values for w_T see ICRP, 1991).
The contribution due to cosmic radiation varies with the altitude in the

Earth's atmosphere which is a result of the complex interaction cascade described in Section 2.4. Figure 2.13 shows the contribution of different cosmic ray particle species to the equivalent dose rate as a function of altitude in the Earth's atmosphere. At sea level, as shown in this figure, the muon com-

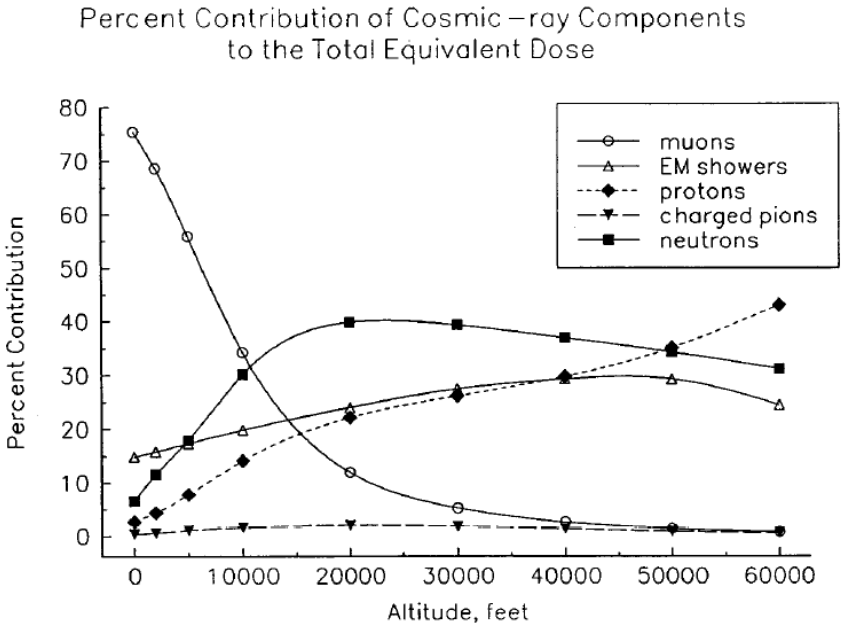

Figure 2.13: *Contribution of different atmospheric cosmic ray particles to the cosmic ray equivalent dose rate in the Earth's atmosphere as a function of altitude (Reprinted from O'Brien et al., 1996, Copyright (1996), with permission from Elsevier)*

ponent dominates with more than 70 % whereas neutrons contribute with less than 10 % to the dose. At typical flight altitudes the main contributors to the dose are neutrons with up to 40 %. Other significant components in aircraft altitudes are protons, electrons and photons. Beyond an altitude of about 50 000 feet (about 15 km) protons start to become more significant than the neutrons but the contribution of neutrons is still above 30 % at an altitude of 60 000 feet (about 18 km). As explained in Section 2.4, the intensity of ionizing radiation increases with increasing altitude from ground level to common flight levels. Thus, aircraft crew and passengers are exposed to a higher level of ionizing radiation and thus higher dose rates than at sea level. The amount by which the dose rates are higher during a flight than on ground depends on various factors such as the flight altitude, the magnetic latitudes along the flight route and the time when the flight takes place according to

the phase of the solar cycle (see Section 2.4). In UNSCEAR (16.01.14b) figure 3 'Measurement results of cosmic ray exposure rate at aircraft altitudes' dose equivalent rates are displayed versus altitude in kilometers for different flight levels and different latitudes for solar minimum and solar maximum conditions. The values for the dose equivalent rates in this figure range between about 1 and almost 10 μSv/h. When comparing the worldwide annual effective dose at sea level caused by cosmic rays which is 0.4 mSv (equals about 0.046 μSv/h) to the values shown in the above mentioned figure the dose rates at flight altitudes are around two orders of magnitude higher than the contribution of cosmic rays to the dose rate on ground, depending on altitude, latitude and solar cycle. Note that the value at sea level is given in effective dose (the protection quantity) whereas the values at flight levels are given in dose equivalent (the operational quantity). Since the protection quantities are not measurable directly, an operational quantity has to be used as an estimation for the protection quantity. Under certain assumptions it is reasonable to use dose equivalent as an estimate for the effective dose (details see European Commission, 1996). For further details on the radiation exposure in flight altitudes see e.g UNSCEAR (16.01.14c), European Commission (1996), Bartlett (2004), Alberts et al. (1997) and references therein.
To summarize, the high biological effectiveness of neutrons as well as their large contribution to the dose rates at flight altitudes and beyond makes it so important to measure and carefully distinguish them from the other components in a mixed radiation field.

Chapter 3

The Phoswich Detector

This chapter describes the development and final set-up of the Phoswich detector PING (**P**hoswich **I**nstrument for **N**eutrons and **G**ammas) including the sensor head and the read-out electronics. The focus of this work is the development of the sensor head.

3.1 Sensor Head

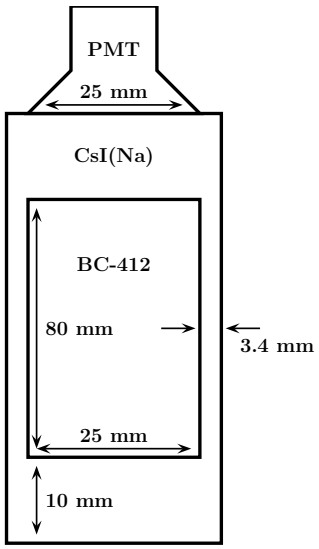

Figure 3.1: *Sensor head of the developed Phoswich detector*

A schematic view of the sensor head is shown in Fig. 3.1. It consists of the inner plastic scintillator made of the material BC-412 by the company Saint-Gobain Crystals (Saint-Gobain/BC-412, 21.09.2012) and an anti-coincidence

made of sodium doped caesium iodide (in the following referred to as CsI(Na)). The dimensions of the BC-412 are 8 cm · 2.5 cm · 2.5 cm and the anti-coincidence has a thickness of 1 cm on the top and the bottom and 0.34 cm on the sides. The main purpose of the developed instrument is to detect neutrons with energies up to 100 MeV and distinguish these from γ-rays. Therefore the dimensions of the inner plastic scintillator have been chosen so that the secondary protons produced by the interaction of 100 MeV neutrons with the plastic scintillator can be stopped within the BC-412. The projected range of 100 MeV protons in a vinyltoluene based plastic scintillator is 7.7 g/cm^2 (see Berger et al., 2005b) and this is equivalent to 7.5 cm in BC-412. Because of its geometry the detector has a preferred direction for high energy neutrons. Thus, only 100 MeV neutrons traversing the sensor head from top to bottom or vice versa can be stopped within the plastic scintillator. The anti-coincidence has to be thick enough in order to be able to identify particles interacting with both scintillators. If the anti-coincidence was too thin the light output for a particle interacting only in BC-412 and a particle traversing both scintillators would be too similar and neutral particles measured in the plastic scintillator could not be distinguished from particles interacting in both scintillators.
The inner plastic scintillator is produced as one single piece but as CsI(Na) is very brittle it is not possible to produce a crystal with such a complex shape needed for this sensor head. Thus, the anti-coincidence is made of 18 single pieces.
The scintillators are optically coupled with the two-component optical transparent adhesive RTV-141 (Rhodorsil, 30.11.2010). Figure 3.2 shows a photo of the scintillators glued together.

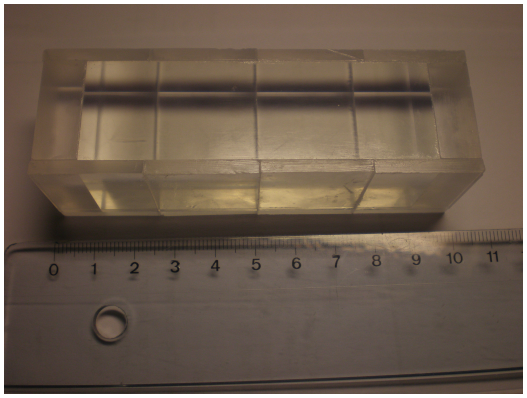

Figure 3.2: *The scintillators for the sensor head attached to each other*

After attaching the scintillators to each other the whole scintillator package is wrapped in two layers of Millipore® (Millipore, 27.11.2012) and Teflon® tape. Millipore® is used as a reflector to reduce the loss of light. The scintillator package is read out by a PMT which is attached to the narrow side of the package with the space-grade encapsulant Dow Corning®93-500 (Dow Corning, 07.12.2012). In Fig. 3.3 photos of the wrapped scintillator package and the assembly of the PMT are shown.

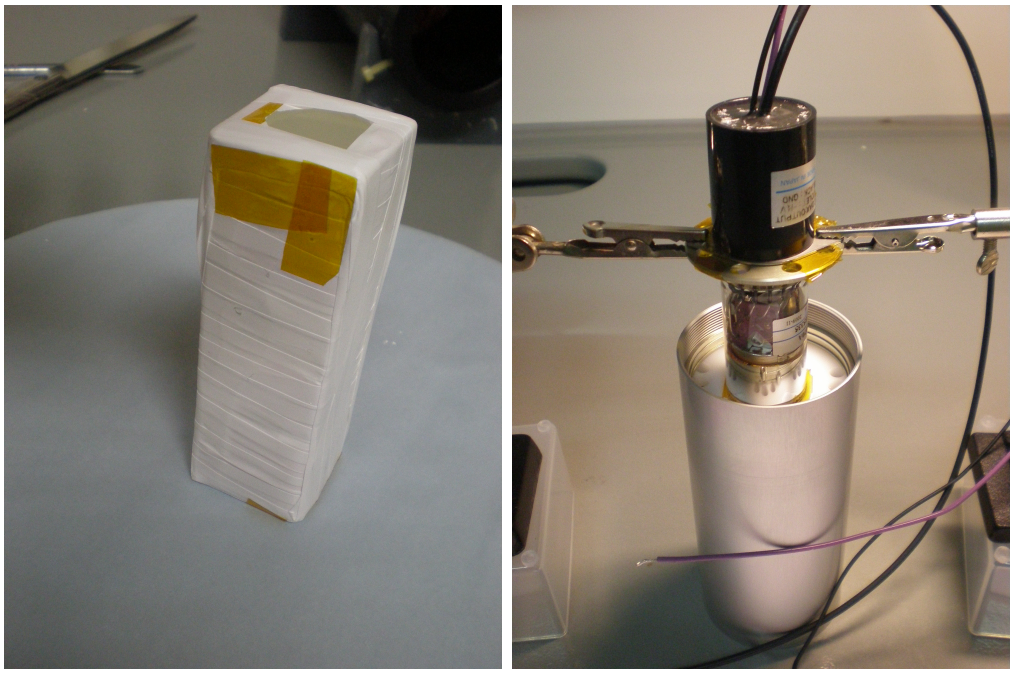

Figure 3.3: *Left panel: the scintillators wrapped in Millipore® and Teflon® tape. Right panel: assembly of the photomultiplier tube*

The PMT that was chosen for this instrument is the R5070A produced by Hamamatsu (Hamamatsu/R5070A, 21.09.2012). It is a compact head-on type photomultiplier tube with a diameter of 25 mm and a spectral response from 300 to 900 nm. Its wavelength of maximum response is at 420 nm which matches the emission spectra of both scintillators. The spectral response of the R5070A is shown in Hamamatsu/R5070A (21.09.2012). The emission spectrum of CsI(Na) reaches from 300 to 600 nm with a maximum at 420 nm (Saint-Gobain/CsI, 21.09.2012) and the one of BC-412 ranges from about 400 to 520 nm with a maximum at 434 nm (Saint-Gobain/BC-412, 21.09.2012). There are two main reasons why these two materials have been chosen for the developed Phoswich detector. As already mentioned the main purpose of the detector is the measurement of neutrons with energies up to 100 MeV

and to distinguish these from γ-rays. The first reason to choose a plastic scintillator surrounded by an anti-coincidence made of CsI is that plastic scintillators are very prominent materials to use for neutron detection while CsI is widely used for γ-ray detection. The plastic scintillator BC-412 which has been chosen for the neutron detection is made of polyvinyltoluene. This is a synthetic polymer which is hydrogen rich. Therefore this material is very effective for fast neutron detection because up to the total energy of the incident neutron can be transferred by the interaction via elastic scattering. Besides the fact that CsI is an excellent material for γ-ray detection due to it's high atomic number Z the advantage of CsI as an anti-coincidence is that CsI is a very bright scintillator. The light yield of CsI is about three times the light yield of BC-412 (calculation see Appendix A). Thus, a particle interacting in both scintillators will yield a much higher light output than a particle only interacting in BC-412.
The above mentioned efficiency of the chosen materials for neutron and γ-ray detection and their different light yield are not the only reason why these two materials have been chosen. Another important advantage of the combination of these two particular scintillator is that they have very different decay times of their light output. In general plastic scintillators have much smaller decay times than inorganic scintillators. While BC-412 is a fast scintillator with a decay time of only 3.3 ns (Saint-Gobain/BC-412, 21.09.2012), CsI(Na) is rather slow with a primary decay time of 630 ns (Saint-Gobain/CsI, 21.09.2012). Thus, BC-412 is two orders of magnitude faster than CsI(Na) and this large difference in decay times makes it possible to distinguish the pulses from the two different scintillators via pulse shape analysis. In Fig. 3.4 a schematic view of the light output (left panel) and the

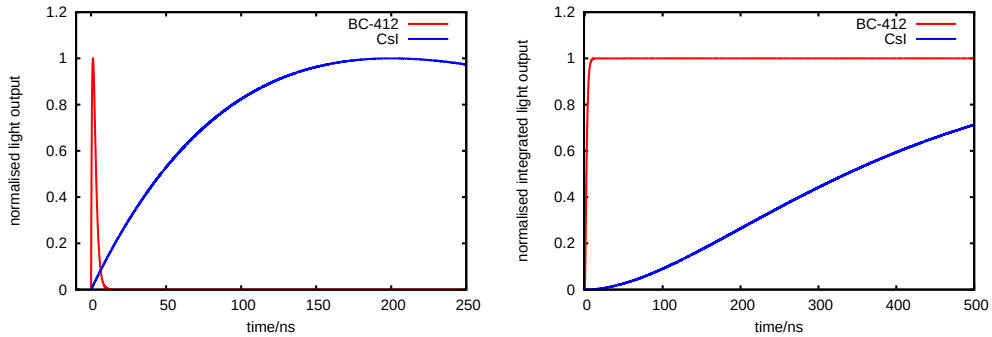

Figure 3.4: *A schematic view of the normalised light output (left panel) and the integrated light output (right panel) of CsI and BC-412*

integrated light output (right panel) is shown for the two scintillators. The

large difference in decay times is clearly visible in both plots. The integrated light output is shown here because in the developed Phoswich detector an integrating preamplifier is used (see Section 3.2). The output pulses from the instrument will have the shape of the integrated light output curves.

3.2 Signal Processing and Read-Out-Electronics

A schematic view of the signal processing in the Phoswich detector is shown in Fig. 3.5. In the developed detector the data handling, processing and storage is done by the IRENA read-out electronics (RENA: Read-out Electronics for Nuclear Applications) which have been developed by the group of Extraterrestrial Physics at the University of Kiel. The read-out electronics include a Charge Sensitive Amplifier (CSA), shapers, Analogue-to-Digital Converters (ADCs), a Field Programmable Gate Array (FPGA), a microcontroller and a Security Disc card (SD-Card).
When ionizing radiation interacts with the instrument energy will be deposited in either the plastic scintillator, the CsI(Na) or in both scintillators. The scintillators re-emit this absorbed energy in form of light. Since the two scintillators are optically coupled only the light output from both scintillators together can be measured by the PMT. Within the PMT the light is converted into an electron current. The output of the PMT is fed into the preamplifier which converts it into a voltage pulse. Afterwards the voltage pulse is processed in two different ways. On the one hand the direct pulse is amplified and then converted by the ADC. On the other hand the pulse is first shaped before being amplified and fed into the ADC. The FPGA samples the ADCs with 3 MHz and always stores the last 64 ADC values for further processing. The result of this processing are four different PHA (Pulse Height Analysis) words. These four parameters will be explained in detail in Chapter 4. One of the PHA words derived from the direct pulse is used for the trigger. In case this PHA word exceeds the predefined trigger level the PHA words for the direct and the shaped signal are sent to the microcontroller. The processor stores the PHA values on the SD-Card or sends them to a PC via USB.
The processing within the FPGA as well as the structure of the data output from the instrument is discussed in detail in Chapter 4. The data are stored in binary format and include PHA words for every event in the detector as well as the time information for the stored event. Additionally housekeeping data including temperature, pressure and front end currents are stored.

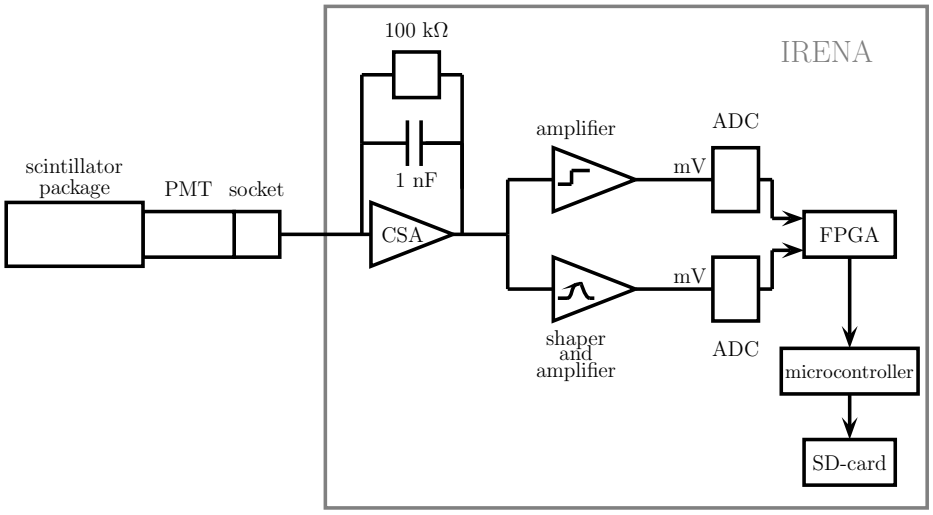

Figure 3.5: *Schematic view of the signal processing in the Phoswich detector*

Two changes had to be made in the standard IRENA system for the application in the Phoswich detector. A different charge sensitive amplifier is used for the Phoswich detector because a lower amplification is needed in order to be able to measure up to 100 MeV. The preamplifier has a feedback capacitor of 1 nF which leads to a lower amplification than normally used for silicon detectors for example. Secondly, a separate high voltage power supply for the PMT was needed. The high voltage DC-DC-converter C4900-01 manufactured by Hamamatsu (Hamamatsu/HV, 23.09.2012) is used to supply the PMT with -867 V and it is placed on a small printed circuit board (PCB) right on top of the IRENA power board.

3.3 The Flight Set-up

The final set-up of the instrument is shown in Fig. 3.6. The cylindrical sensor head which is located in the front is connected to the IRENA electronics via the red high voltage cable and the black signal cable. Below the electronics box a battery pack is located. The dimensions of the whole set up are at the bottom 160 mm · 180 mm and at the top 125 mm · 155 mm. The total height is 230 mm and the total weight is less than 2 kg. The instrument is operated at 24 V and needs 0.11 A. This leads to a power consumption of about 2.6 W.

In Fig. 3.7 the CAD drawing of the flight set-up of the Phoswich instrument

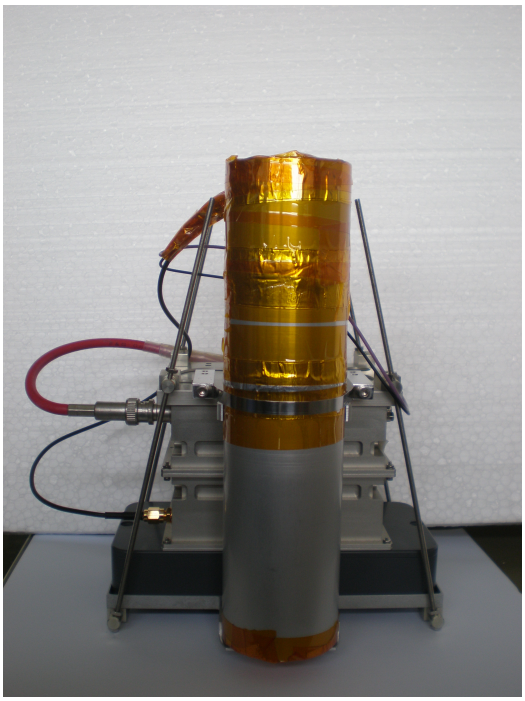

Figure 3.6: *Final set-up of the Phoswich detector; Dimensions are: 160 mm · 180 mm (bottom) and 125 mm · 155 mm (top). The total height is 230 mm*

is shown. The housing of the sensor head and the electronics as well as the frame which joins the different parts is made of aluminium. The battery pack is made of the synthetic material POM (polyacetal) (Seimetz, 2012) and the two belts needed to fixate the sensor head to the aluminum frame consist of high quality-steel (#14305) (Seimetz, 2012).

The Phoswich detector which is developed in this work is a portable device which is designed to measure neutrons in a mixed radiation field and distinguish them from γ-rays. The instrument is also sensitive to charged particles and it is light enough to be flown with a weather balloon.

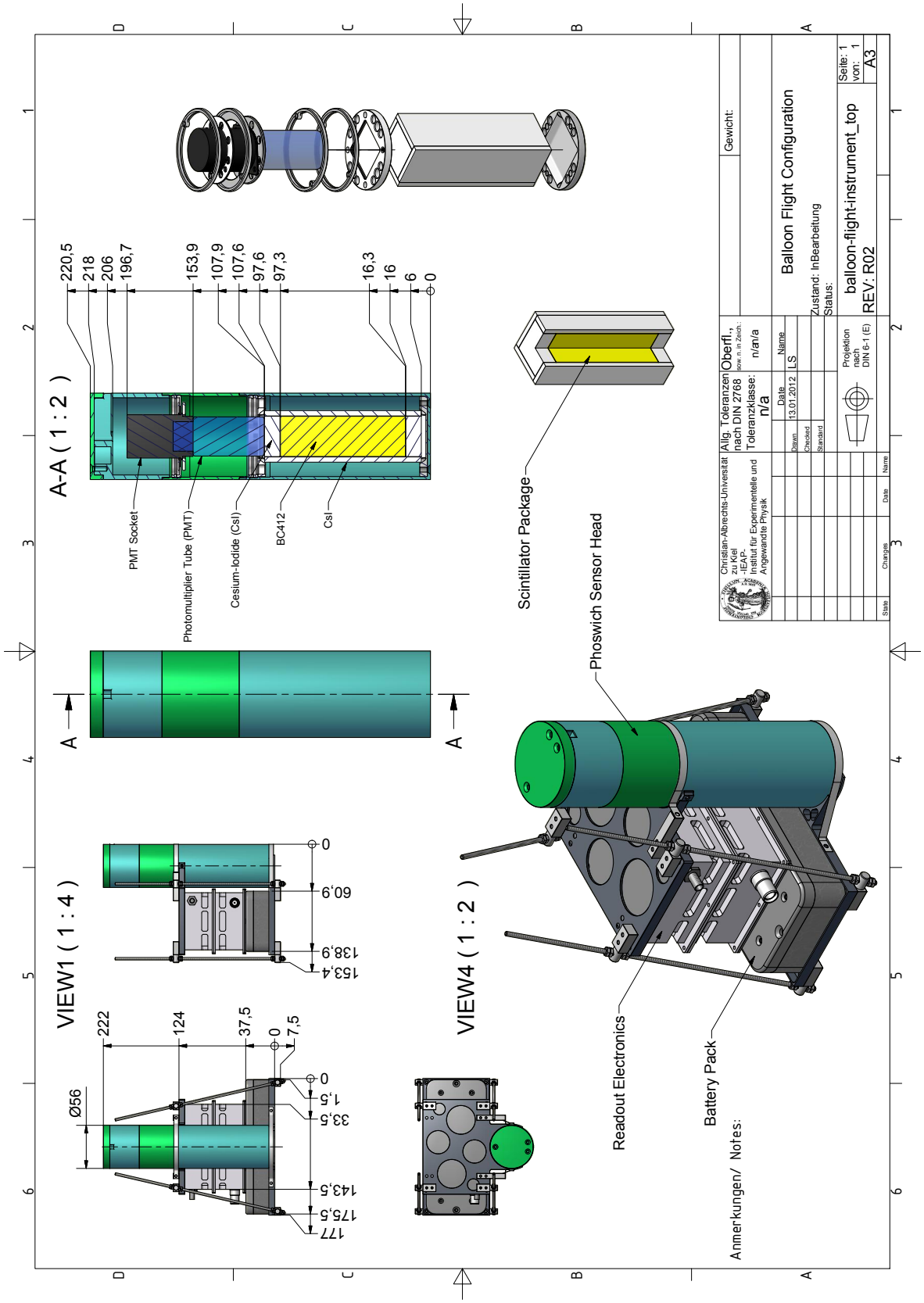

Figure 3.7: *CAD drawing of the developed Phoswich detector (Seimetz, 2012)*

Chapter 4

Data Reduction and Analysis

This chapter discusses the general structure of the output data from the Phoswich detector. The data reduction and the data analysis based on the pulse shape analysis is described.

4.1 Data Structure

The idea of the data analysis for the output signals from the developed sensor head is to classify the output pulses in terms of their shape. One possibility to do this is to measure the output signal in two different time frames: a short one to measure the light from the fast scintillator and a long one to measure all light from both scintillators. A comparison of these two measurements provides information about the pulse shape. This is a method know from nuclear physics and it has been described by e.g McKibben et al. (2008).
In the developed Phoswich detector this is realized with the IRENA read-out electronics which have been developed by the group of Extraterrestrial Physics at the University of Kiel. All the data handling, processing and storage in the developed instrument is done by the IRENA.
The IRENA is a data acquisition system with 18 channels where each channel is sampled by a 12-bit-ADC at 3 megasamples per second (Böttcher, 2011). During the sampling the last 64 samples are always stored in a ring buffer. With each newly measured sample a pulse height and phase reconstruction is initiated which is based on up to 16 selected samples in this ring buffer. The first sample used for this procedure is always the last sample read by the ADC. The other samples used are determined at fixed times before that last sample. The pulse height S and the phase P are calculated as a linear

combination of the selected samples s_i with coefficients a_i and b_i:

$$S = \sum_{i=0}^{15} a_i \cdot s_i \tag{4.1}$$

$$P = \sum_{i=0}^{15} b_i \cdot s_i \tag{4.2}$$

For detailed information on the IRENA system see the internal report by S. Böttcher (Böttcher, 2011).
In the read-out electronics of the Phoswich detector only two of the available 18 channels are needed. For the first channel the output of the preamplifier is fed into the ADC directly which means that the direct pulse is sampled. For the second channel the output of the preamplifier is shaped first before being sampled. In addition to the above described pulse height and phase reconstruction which is done with the shaped pulse, a pulse shape analysis is done using the direct pulse. The two parameters F and N which provide a measure for the slow and the fast fraction of the measured pulse, respectively, are calculated similarly to S and P using the samples $s_{d,i}$ of the direct pulse and the coefficients c_i and d_i:

$$F = \sum_{i=0}^{15} c_i \cdot s_{d,i} \tag{4.3}$$

$$N = \sum_{i=0}^{15} d_i \cdot s_{d,i} \tag{4.4}$$

The direct channel is the one that triggers the measurement. Only when the value F exceeds a certain threshold (in the developed Phoswich detector the threshold is usually set to 40 mV) the calculated values S, P, F and N are stored. The four parameters S, P, F and N are in each case the convolution of the measured pulse with a specific analysis function given by the coefficients a_i, b_i, c_i and d_i. In the following these analysis functions will be referred to as function A, B, C and D.
Figures 4.1 and 4.2 exemplarily show the procedure to calculate the four parameters S, P and F, N, respectively. In Fig. 4.1 the samples of the shaped pulse s_i (dotted red line) and the analysis functions A (green) and B (blue) for the resulting parameters S and P are shown. It is clearly visible that the analysis function A is defined so that S is sensitive to the amplitude of the measured pulse. The analysis function B is defined so that P is sensitive to

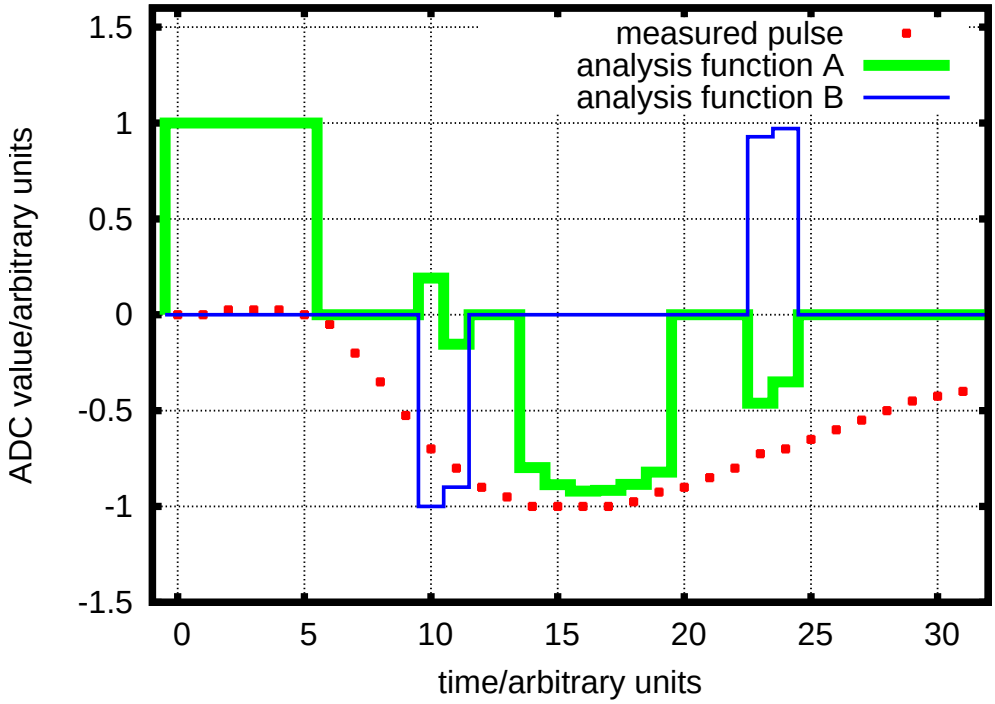

Figure 4.1: *Shaped pulse with analysis function A and B*

the phase. When the measured pulse is convolved with the analysis function A the resulting parameter S is a measure for the energy of the event that occurred in the detector. When the measured pulse is convolved with the analysis function B the resulting parameter P provides the information when the pulse was measured with respect to the ADC clock. This is very important because the determination of the amplitude of the pulse depends on the exact time when the pulse was detected according to the ADC clock.

Figure 4.2 illustrates the similar procedure for the direct pulse. The samples of the pulse $s_{d,i}$ (dotted red line) and the analysis functions C (green) and D (blue) for the resulting parameters F and N are displayed. It is clearly visible that the analysis function C is sensitive to the slow fraction of the pulse whereas the analysis function D is sensitive to the rising part of the pulse. Thus, the convolution of the measured direct pulse with the analysis function C is a measure for the slow fraction of the pulse (the resulting parameter F). The convolution of the measured pulse with the analysis function D yields the parameter N which is a measure for the fast fraction of the measured pulse.

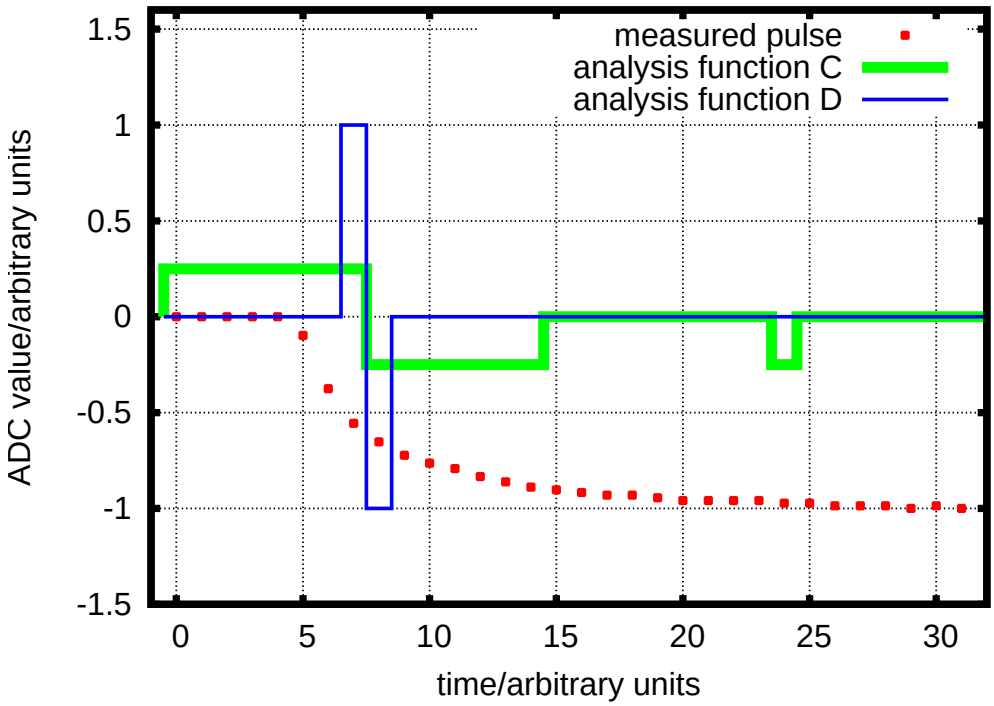

Figure 4.2: *A measured direct pulse with analysis function C and D*

In summary, the four parameters are:

F : direct pulse convolved with the 'slow' analysis function
measure for the slow fraction of the measured pulse

N : direct pulse convolved with the 'fast' analysis function
measure for the fast fraction of the measured pulse

S : shaped pulse convolved with an analysis function sensitive to the amplitude
measure for the energy of the measured pulse

P : shaped pulse convolved with an analysis function sensitive to the phase
measure for the time when the particle was detected

To summarize, the data output of the Phoswich detector consists of two different data streams. The first stream consists of the four parameters F,S,P and N which are stored together with a timestamp for each event which

occurs in the instrument. In addition to these four values it is also possible to store a predefined number of samples s_i and $s_{d,i}$ for every event.

4.2 Data Reduction

The principle idea of the measurements with the Phoswich detector is the assumption that the neutrons will interact primarily with the plastic scintillator and that the γ-rays will interact mainly with the CsI(Na). Thus, to separate the neutrons from the rest of the particles, events happening only in the plastic scintillator have to be separated from events happening only in the CsI(Na) and events in both scintillators. As the plastic scintillator is very fast compared to the CsI(Na) it is expected that a measured neutron is characterized by a rather fast measured pulse. This means a neutron event should have a rather large value for N and a rather small value for F. This leads to a high value of the ratio N/F in case of a neutron event.
A first test to see if events happening only in the plastic scintillator, which are assumed to be mainly caused by neutrons, can be separated from the rest of the particles is to plot the ratio N/F, meaning fast to slow fraction of the pulse versus F. In Fig. 4.3 such a plot is shown. Each point in this plot equals one measured event. In this figure three different measurements are shown: 14.8 MeV neutrons (red), cosmic muons (green) and a measurement with ^{207}Bi which is a γ-ray source (blue). Along the y-axis one can see that the events from the neutron measurement are concentrated at larger values for N/F whereas the events from the other two measurements are located at smaller N/F values. A boundary between these different populations could be defined at about N/F=0.24. Since N/F is the ratio between the fast and the slow fraction of the measured pulse a larger value for N/F means that this pulse has a large fast component. Considering the fact that BC-412 is a very fast scintillator and that this material has a high efficiency for the detection of neutrons most events above 0.24 could be considered as neutron events. The γ-ray and muon measurement cannot be separated easily. Both measurements are spread along the x-axis with the muon measurement reaching up to higher x-values.
This first approach to separate the pure plastic scintillator events from the rest of the particles, which is shown in Fig. 4.3, is only a first test and will be not be used for the further data analysis (please note that the measurements shown in this figure are taken with an earlier stage of the instrument). A better procedure for the separation which will be used for the data analysis is explained in the following.
Even though the parameters F and N are the most important ones for the

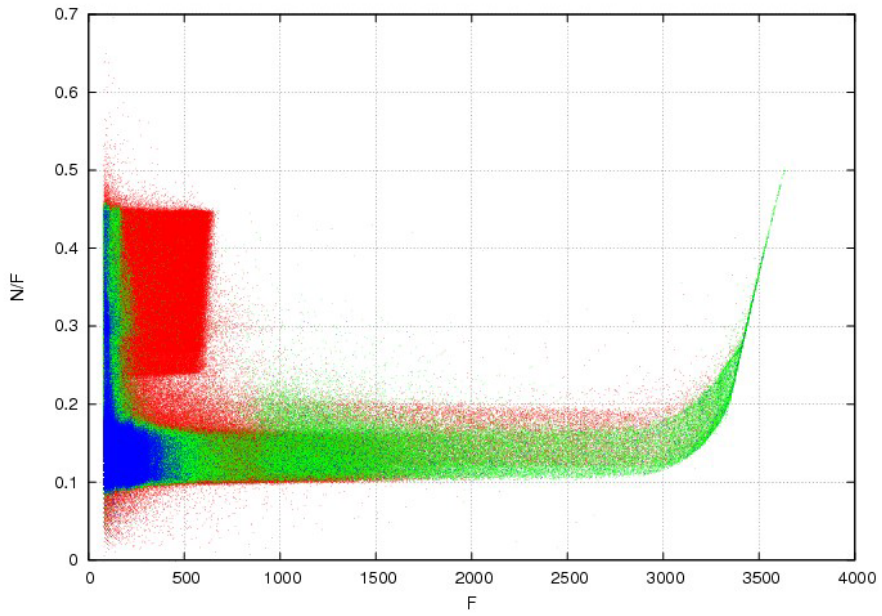

Figure 4.3: *First attempt to separate the neutron events from the rest of the particles. The ratio of the fast to the slow fraction of the pulse (N/F) versus the slow fraction of the pulse (F) is displayed. Three different measurements are shown in comparison: 14.8 MeV neutrons (red), cosmic muons (green) and a measurement with ^{207}Bi (blue).*

pulse shape analysis itself a better separation of the pure plastic events is possible using the parameters S and P in addition to N and F. To visualise not only the ratio of fast to slow fraction of the pulse (N/F) but also the pulse height and phase information of a measured event a 2d-histogram plot of the events as shown in Fig. 4.4 can be used. In Fig. 4.4 the phase P divided by the pulse height S versus the ratio N/F is displayed. Each point in this plot equals one measured event. The data shown here are from a measurement with 14.8 MeV neutrons. Displayed here are the processed data. To sort out non-physical events as well as events that exceed the linear range of the electronics the following conditions were used: prescaler=0, $S/3500 \leq 3250$, $P/S \geq -0.75$ and $P/S < 0.99$. For the data analysis the values F and S are normalised to approximate the pulse height in units of mV. In order to do that S is divided by 3500 and F is divided by 1024. In the following $S/3500$ is referred to as S and $F/1024$ is referred to as F.

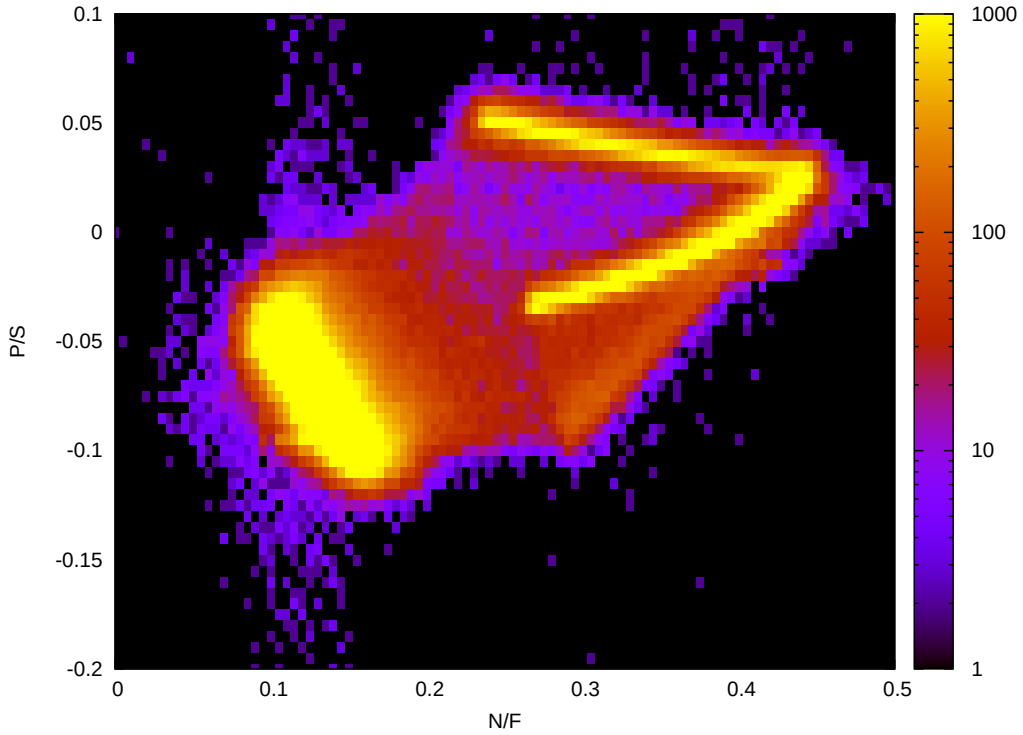

Figure 4.4: *Processed data of the 14.8 MeV neutron measurement*

In Fig. 4.4 four different event populations are visible. There is an oval population on the left side which in the following is referred to as palm. On the right hand side there are three joined populations. In the following these are referred to as upper, middle and lower finger. In other measurements, for example with 100 MeV and 66 MeV, in the measurements on board airplanes and on board stratospheric balloons, an additional branch is seen in the raw data (see Appendix B). This additional branch can be greatly reduced with the above mentioned conditions to sort out non-physical data so that it is merely a tail of the palm. For the data analysis this tail is always treated as belonging to the palm population.
Initially it is not clear why there are four instead of only two distinct populations. Based on the concept of the instrument one would expect to find one population for the events from CsI(Na), one population for BC-412 and some events in between.
The palm is very well separated from the three fingers and lies at small values for N/F, meaning that the slow fraction F of the pulse is large. Since the CsI(Na) scintillator with its long decay time of the light output is a slow

scintillator and the fact that the cross section for γ-rays is large in CsI(Na) many of these events are caused by γ-rays. But when comparing Fig. 4.4 with Fig. 4.3 it is obvious that the palm population also contains events caused by charged particles. This is due to the fact that when a particles interacts with both scintillators the small, fast pulse resulting from the interaction with the plastic scintillator will not change the total resulting signal enough to be differentiated from a pure CsI(Na) interaction.
The three fingers on the other hand lie at larger values for N/F, which means that the fast fraction N of the pulse is large. Taking into account that BC-412 is the fast scintillator and that the efficiency for neutron detection is very high in this material many of the events in the fingers are events caused by neutrons. The design of the sensor head of the instrument alone cannot explain why these three populations occur but their formation can be explained with an effect from the read-out electronics. This will be discussed in Section 4.3.

4.3 Data Classification via Pulse Shape

To verify that the palm events have a different pulse shape than the finger events (meaning that the palm and finger events originate from the two different scintillators) and to clarify whether the finger events are really three different populations, the events from all the four populations have to be investigated separately. The following cuts were used to separate the populations:

$$\begin{aligned} \text{upper finger}: P/S &> -2.55 \cdot N/F + 0.62 \quad \text{and} \\ P/S &> 0.215 \cdot N/F - 0.065 \qquad (4.5) \\ \text{middle finger}: P/S &> -2.55 \cdot N/F + 0.62 \quad \text{and} \\ P/S &< 0.215 \cdot N/F - 0.065 \quad \text{and} \\ P/S &> 0.34 \cdot N/F - 0.145 \qquad (4.6) \\ \text{palm}: P/S &< -2.55 \cdot N/F + 0.62 \qquad (4.7) \end{aligned}$$

These cuts are illustrated in Fig. 4.5.

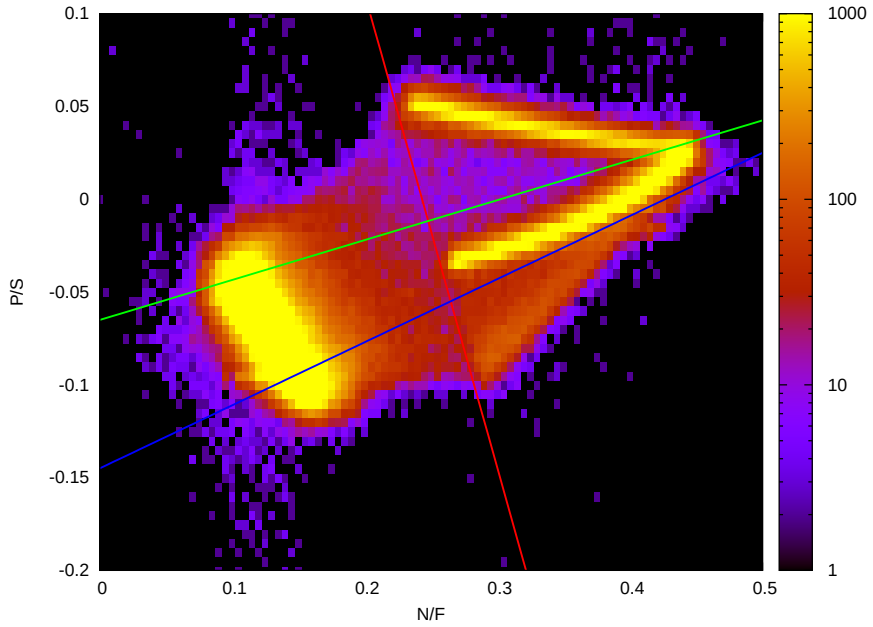

Figure 4.5: *Processed data of the 14.8 MeV neutron measurement with the cuts to separate the different populations*

After the separation of the events into palm, upper, middle and lower finger, the pulses of the events from each population can be compared by plotting the samples of the direct pulse $s_{d,i}$ versus the time. To get a continuous pulse from the discretely measured samples the gaps between the samples have to be filled. This is usually done by using the phase parameter P but in Fig. 4.5 it is visible that the data points cannot be described well with the parameter P because they are tilted and shifted with respect to the P/S=0 axis. The parameter P was not very well selected and thus a new phase parameter has to be found. This is done by first defining a parameter λ which describes the distance from a given data point to the new axis where λ has values from 0 to 1. The definition of λ is shown in Fig. 4.6 for the palm (upper panel) and the finger population (lower panel). The general formula for the parameter λ is:

$$\lambda = \frac{(x - x_1) \cdot (x_2 - x_1) + (y - y_1) \cdot (y_2 - y_1)}{(x_2 - x_1)^2 + (y_2 - y_1)^2} \tag{4.8}$$

with x=N/F and y=P/S.

The values for x_1, x_2, y_1 and y_2 are (see Fig. 4.6):

fingers	palm
x_1=0.26	x_1=0.07
x_2=0.45	x_2=0.2
y_1=-0.025	y_1=-0.015
y_2=0.03	y_2=-0.145

The parameter λ is calculated for each event using formula 4.8. The next step is to make a histogram of λ and integrate this histogram. The ascending slope of the integrated histogram is called $\phi(\lambda)$ and it describes the phase shift of the given event with a value between 0 and 1. This phase shift $\phi(\lambda)$ has to be applied to the timestamps of the samples in order to fill the gaps between the discrete samples and get a a continuous pulse. The histogram and the integrated histogram of λ as well as a fit to the rising part of the integrated histogram are exemplarily shown in Fig. 4.7 for the upper finger events. The equivalent plots for the middle and lower finger events as well as the the palm can be seen in Appendix C.

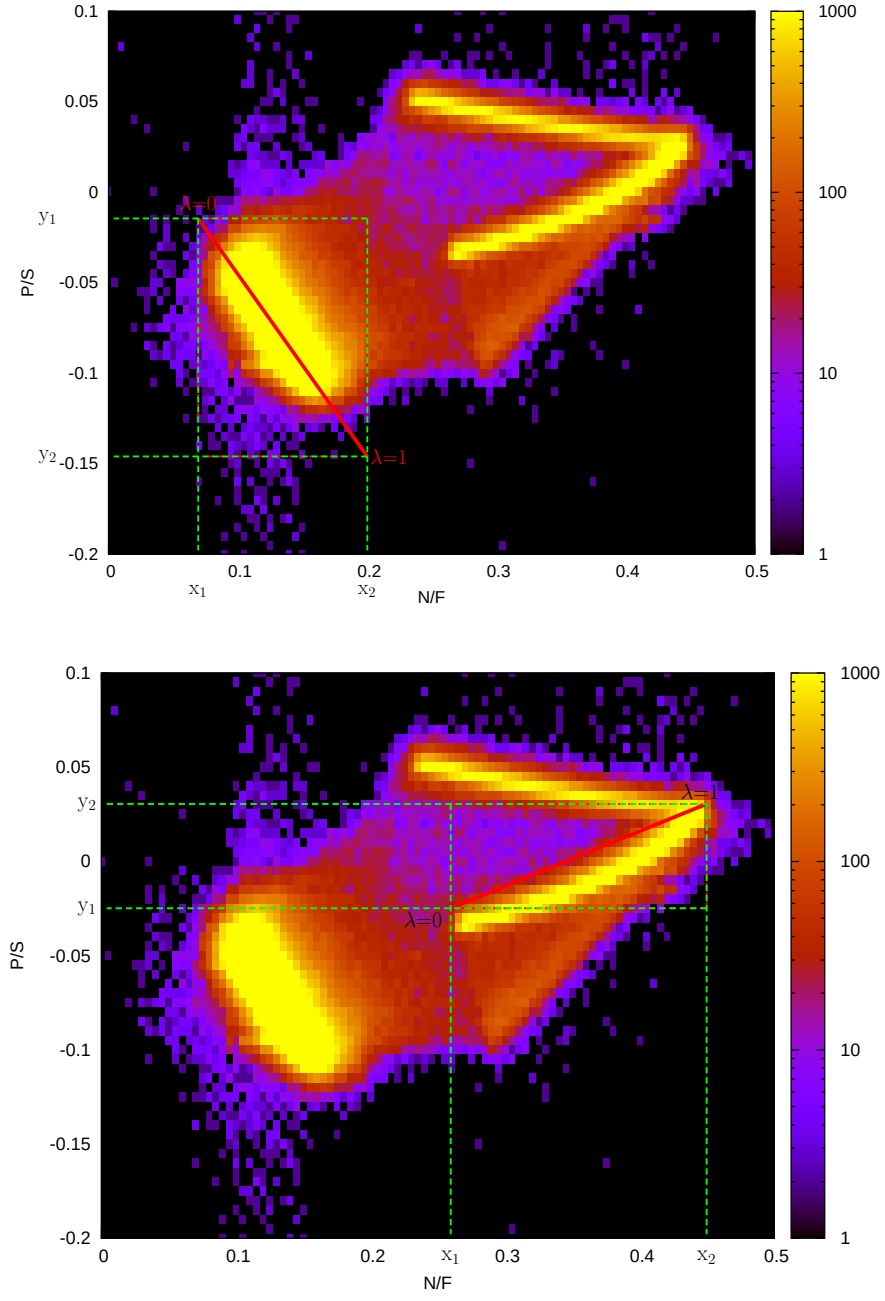

Figure 4.6: *Construction for the calculation of λ for the palm population (upper panel) and finger populations (lower panel)*

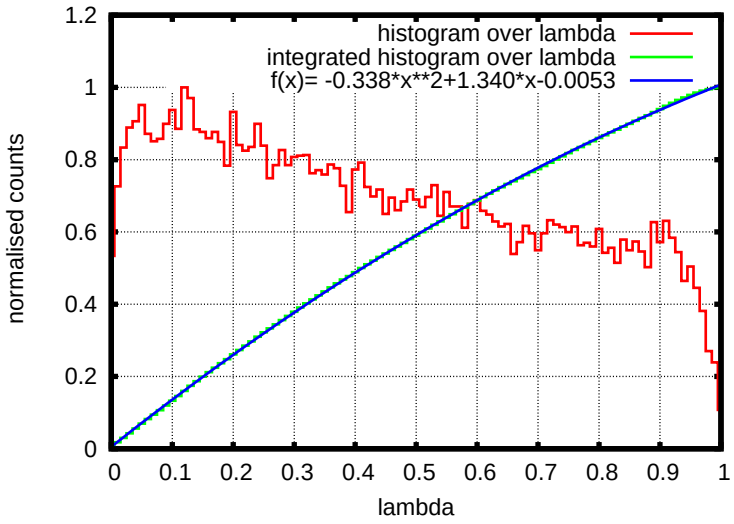

Figure 4.7: *Histogram and integrated histogram of λ for the upper finger events*

In Fig. 4.8 the pulses from the upper, middle and lower finger events are shown. The ADC values of the samples divided by S are plotted versus the time in units of 333 ns. One can clearly see that even though a phase shift $\phi(\lambda)$ has been applied none of the finger populations contains a continuous pulse yet. For the samples in the upper finger a phase shift of 'time+1-0.4 $\cdot$ $\phi(\lambda)$' is used whereas for the middle and lower finger it is 'time+0.6 $\cdot$ $\phi(\lambda)$'. These particular values have been used because it is assumed that the upper and middle finger belong to one population. When the pulses from the three finger populations are compared one can indeed conclude that the events from the upper and the middle finger can be combined. The upper finger samples fit very nicely into the open slots in the middle finger samples. The lower finger events seem to be a different population. The samples of the lower finger do not fit into the upper and middle finger samples. It is assumed that the events located in the lower finger are caused by charged particles which create a signal in both the CsI(Na) and the BC-412 scintillator. This assumption is based on the measurement with ^{137}Cs (see Appendix *D*). In this measurement one can see a lot of palm events which is expected because ^{137}Cs is a γ-ray source. But one can also see a population that goes from the palm towards and into the lower finger. This could for example be Compton electrons which leave the CsI(Na) and enter the BC-412. Therefore, it is concluded that the lower finger does not contain neutron events.

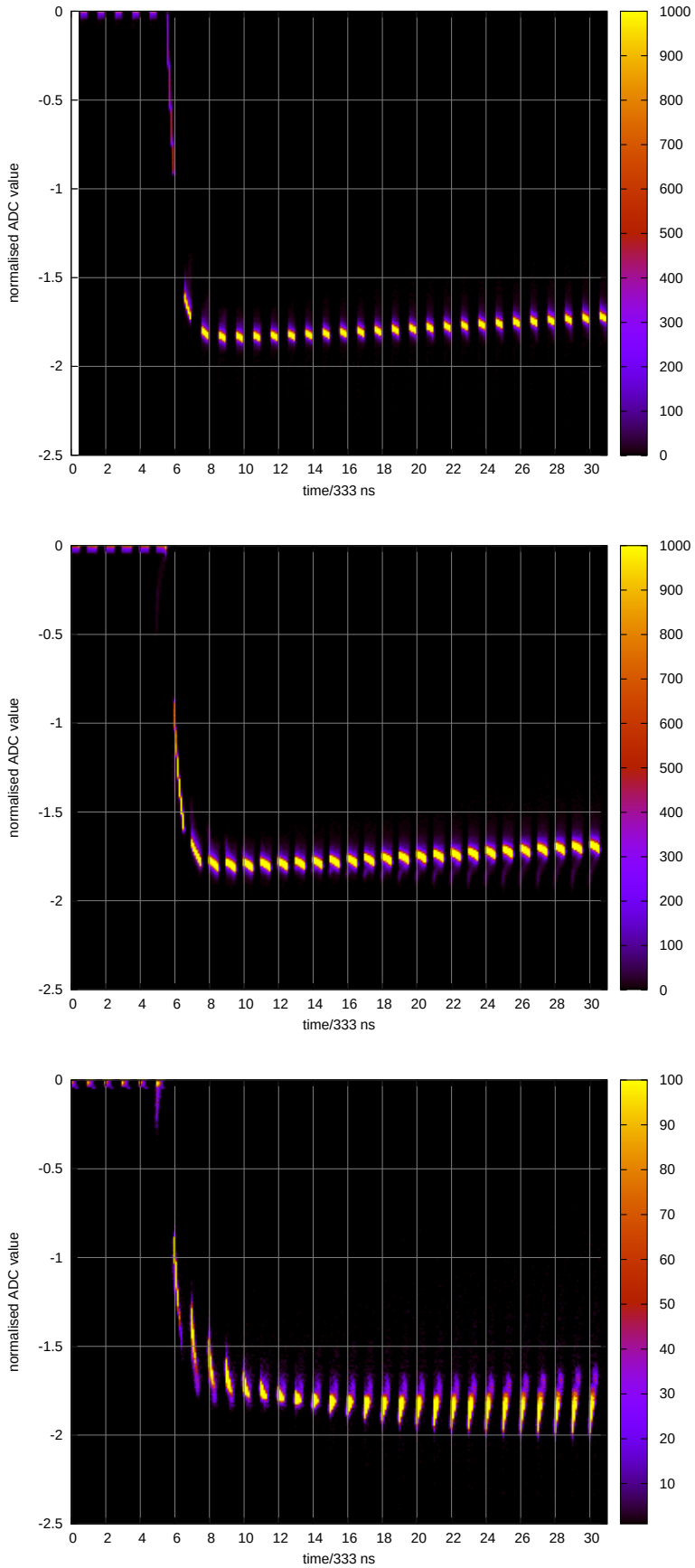

Figure 4.8: *Pulses of the upper, middle and lower finger events. Samples are plotted versus the time including the phase shift*

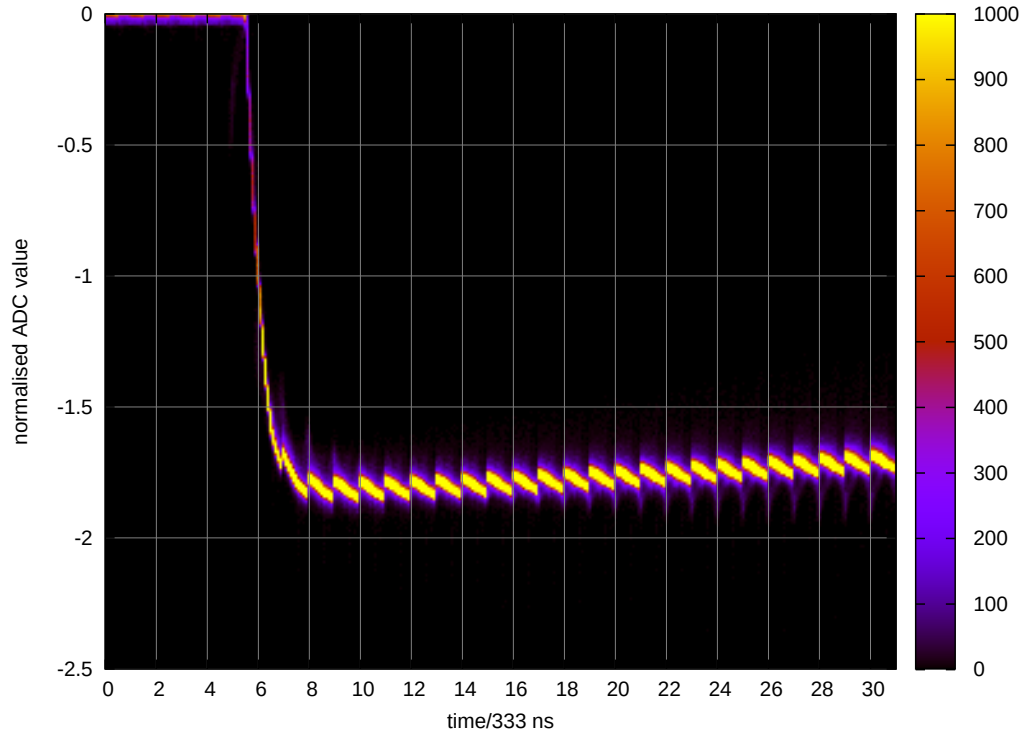

Figure 4.9: *The combination of the upper and middle finger samples*

The combination of the upper and middle finger samples is shown in Fig. 4.9. As seen in this figure the result of the combination is a continuous pulse. Thus, the upper and middle finger events are from the same population. The only difference is that the arrival time of the pulse is not the same. If the pulse arrived before time=6 it is in the upper finger whereas if it arrived after time=6 it is in the middle finger.
In summary, the upper and middle finger events can be combined to one population which contains the events happening only in the plastic scintillator. Because of the fact that the plastic scintillator has a low atomic number Z and that it is hydrogen rich it is more effective for neutron detection than for γ-ray detection. Thus, it is assumed that the events located in the upper and middle finger are mainly neutron events. The palm population contains many γ-rays events but also events caused by charged particles. The lower finger most probably contains mainly charged particles. For the further data analysis the lower finger events are not taken into account.

4.3.1 Phase Correction for the Pure Plastic Events

In Fig. 4.9 where the combination of the samples from the upper and the middle finger are shown it is visible that the samples do not join at the transitions between one sample and the next. This is due to the fact that the reconstructed pulse height S depends on the phase (meaning when the pulse was measured according to the ADC clock). To correct for this effect a phase correction of the pulse height S is needed. A general procedure for this correction is explained in Böttcher (2011). However, the phase correction for the pulses of the Phoswich instrument has been done slightly different. The first step for the correction is to find a fit function to the samples. This is done in Fig. 4.10.
The function that was used for the fit is the following:

$$f(x) = -1.7 \cdot (1 + 0.04 \cdot (x - 25)) \tag{4.9}$$

The value 0.04 in equation (4.9) means that the samples have to be corrected by 4 %. Please note that this function is slightly different for different data

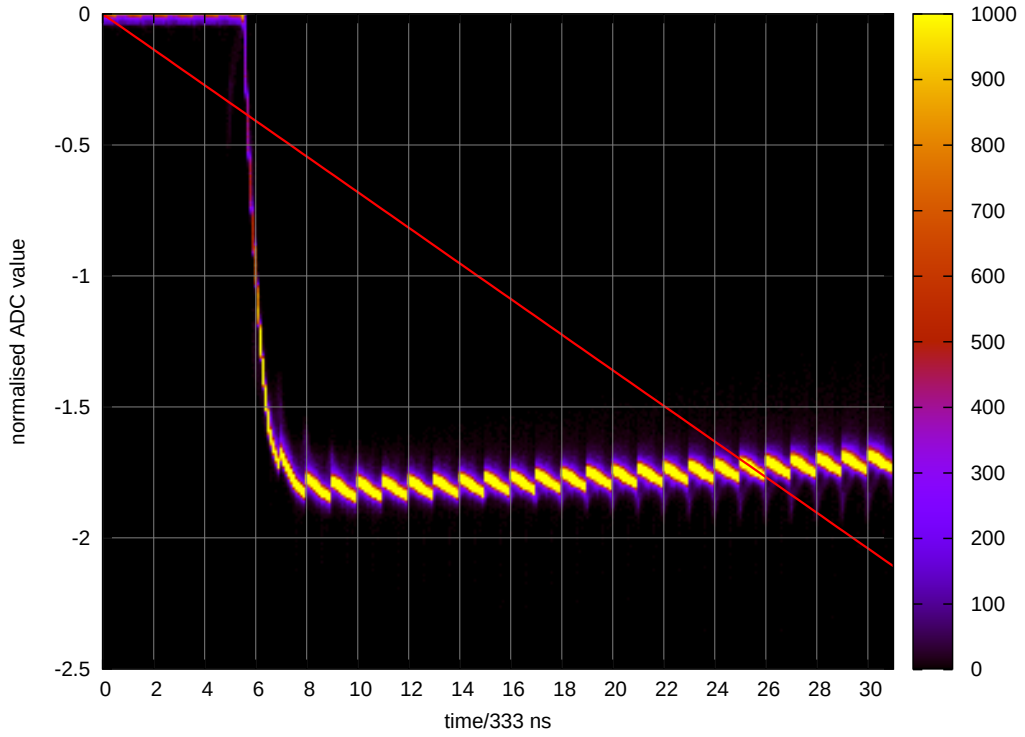

Figure 4.10: *Combination of upper and middle finger samples with a fit to the samples*

sets. However, for almost all measurements a correction with 4 % has been found. This phase correction is applied in the following way: instead of using the ADC value devided by S to plot the pulses, the ADC values are now divided by the phase-corrected S which is:

$$S \cdot (1 + 0.04 \cdot (1 - 0.4 \cdot \phi(\lambda))) \quad \text{for the upper finger events} \tag{4.10}$$

$$S \cdot (1 + 0.04 \cdot (0.6 \cdot \phi(\lambda))) \quad \text{for the middle finger events} \tag{4.11}$$

That means for the phase correction of the pulse height the phase shift of the upper and middle finger events also has to be taken into account. When the phase correction is applied to the samples the result is not only the smooth pulse. Another reason for this phase correction is to achieve a better resolution in the energy spectra, because with this correction the energy of each event can be calculated more accurately.
In Fig. 4.11 the phase corrected pulse from upper and middle finger is seen in the upper panel. This is the final pulse from all events happening only in the plastic scintillator. In the lower panel of the same figure the pulse from the palm events is shown. For the samples of the palm events the phase shift is 'time-$\phi(\lambda)$'. But as seen in this figure no phase correction is needed for the palm events.
Comparing the two pulses in Fig. 4.11 clearly shows that the pulses from the two populations are differing a lot. The pulse from the palm events is rather slow compared to the pulse of the upper and middle finger events which is rather fast. As the palm events are associated with the events happening in CsI(Na) only and the events in the upper and the middle finger with events in the BC-412, it is clear that events from the two different scintillators can be separated according to their pulse shape.

Finally the conditions to separate pure plastic scintillator events, which are assumed to be mostly caused by neutrons, from the rest of the particles are:

$$\begin{aligned} \text{pure plastic upper finger}: P/S &> -2.55 \cdot N/F + 0.62 \quad \text{and} \\ P/S &> 0.215 \cdot N/F - 0.065 \end{aligned} \tag{4.12}$$

$$\begin{aligned} \text{pure plastic middle finger}: P/S &> -2.55 \cdot N/F + 0.62 \quad \text{and} \\ P/S &< 0.215 \cdot N/F - 0.065 \quad \text{and} \\ P/S &> 0.34 \cdot N/F - 0.145 \end{aligned} \tag{4.13}$$

$$\text{pure CsI(Na)}: P/S < -2.55 \cdot N/F + 0.62 \tag{4.14}$$

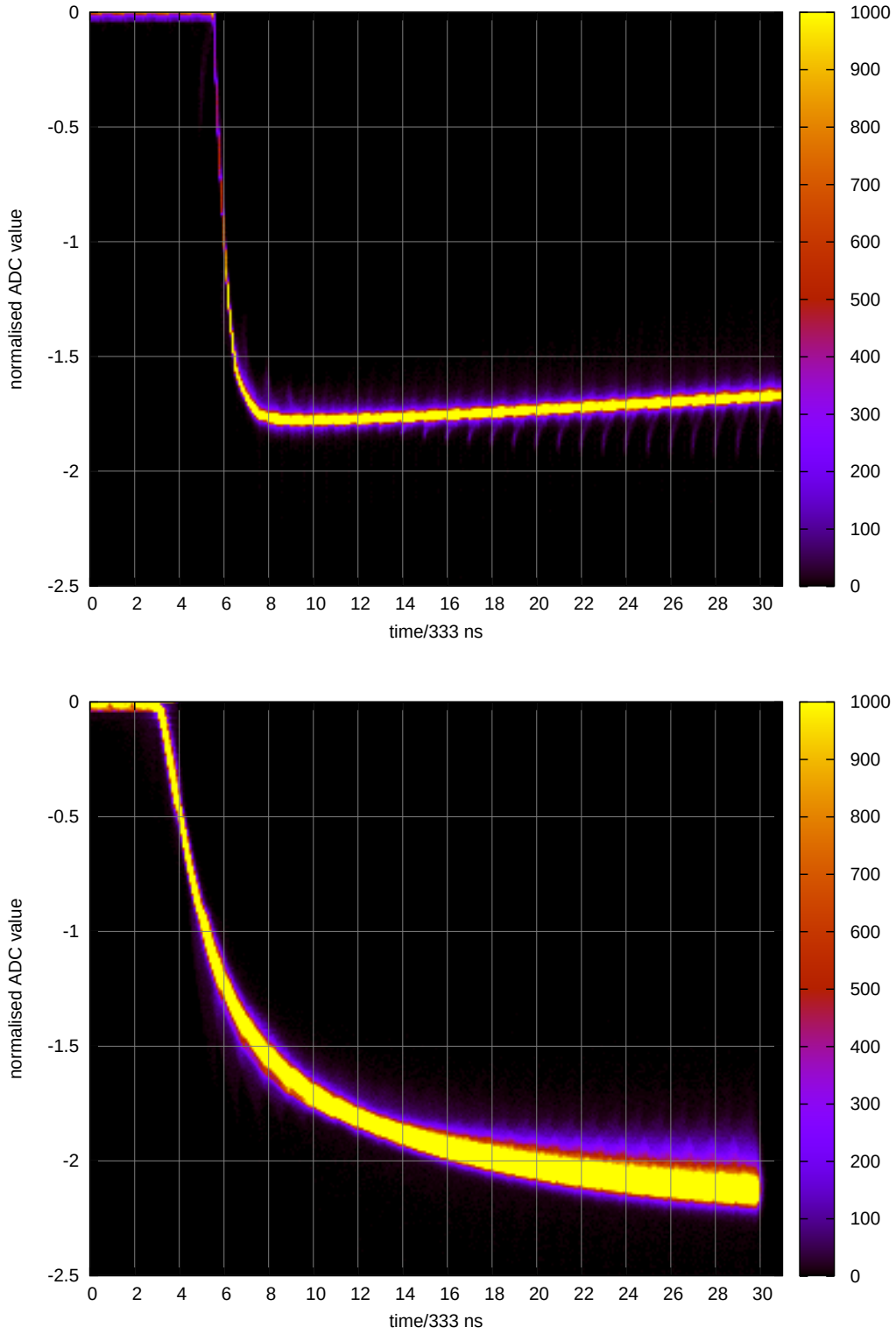

Figure 4.11: *Upper panel: the phase corrected pulse from the pure plastic scintillator events. Lower panel: the pulse from the events of the palm population*

Chapter 5

Calibration

In this chapter the results of the calibration measurements with monoenergetic neutrons and γ-rays are discussed. For the spectra of the neutron measurements shown in this chapter only the events contained in the upper and middle finger are used and the phase correction of the pulse height has been applied. For the spectra of the γ-ray measurements only the palm event are used. As mentioned in Chapter 4 no phase correction is needed for the palm events. At the end of this chapter the response of the plastic scintillator to γ-rays is briefly discussed.

5.1 Calibration With Neutrons

The Phoswich detector has been calibrated with five different neutron energies. Neutrons with energies of 5 MeV, 14.8 MeV and 19 MeV were used at the Physikalisch Technische Bundesanstalt (PTB) in Braunschweig, Germany.
At the iThemba Laboratory for Accelerator Based Sciences, Somerset West, South Africa, measurements with monoenergetic neutrons of 66 MeV and 100 MeV were performed. The position of the sensor head in these measurements was always parallel to the beam and it was positioned in such a way that the neutron beam entered the sensor head at the side where the PMT is located.
In Fig. 5.1 all the measured neutron spectra are shown. All five spectra show the typical neutron edge which is formed when the total energy of the incoming neutron in deposited in the detector. In the 66 MeV and the 100 MeV measurement there is an additional peak in the spectrum at lower energies. It is assumed that these peaks are formed by the nuclear reaction C(n,d) (Röttger, 2012) where the neutron is captured and a deuterium is

emitted. In this reaction an energy of 15 MeV is released which means that the corresponding peaks lie at 51 MeV and 85 MeV, respectively. Later in this section when the neutron energy calibration is discussed, the assumption regarding these additional peaks is verified. The figures 5.2, 5.3 and 5.4 show

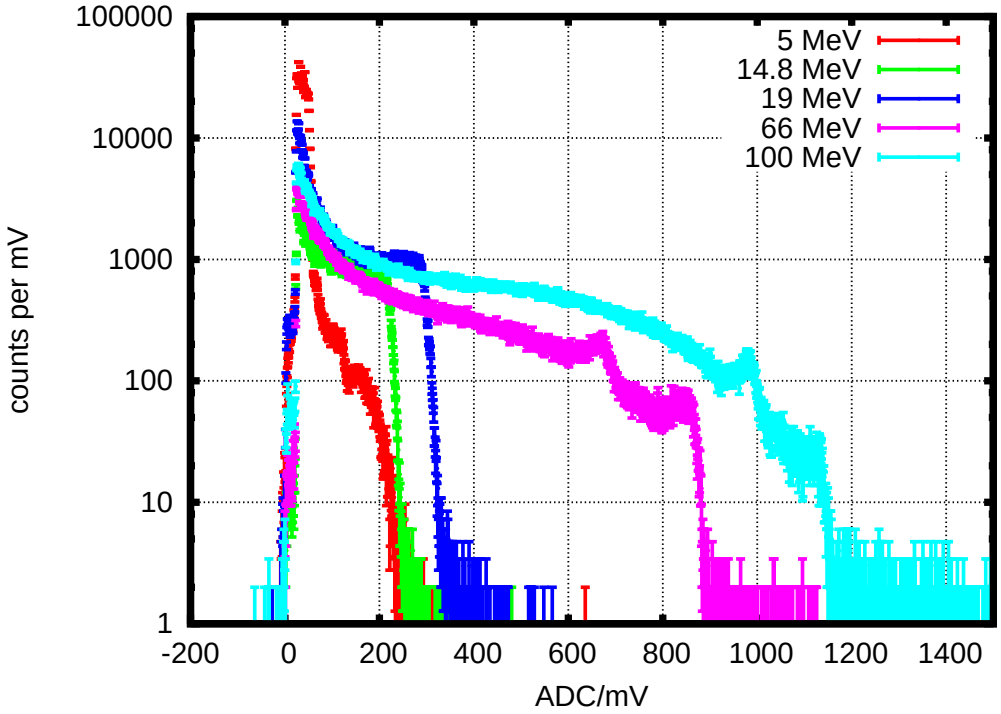

Figure 5.1: *Neutron spectra with 5 MeV (red), 14.8 MeV (green), 19 MeV (dark blue), 66 MeV (pink) and 100 MeV (light blue) neutrons*

the neutron spectra of 5 MeV, 14.8 MeV, 19 MeV, 66 MeV and 100 MeV, respectively. The edges in the neutron spectra can be described by the error function, which is the integration of the normalized Gaussian distribution. Thus, the following fit function has been used to fit the neutron edges:

$$f(x) = \frac{a}{2} \cdot \mathrm{erf}\left(\frac{b-x}{c^2}\right) + d \tag{5.1}$$

with

erf : errorfunction
a : amplitude of the spectrum on the left side of the neutron edge
b : position of the neutron edge
c : measure for the width of the neutron edge
d : amplitude of the spectrum on the right side of the neutron edge

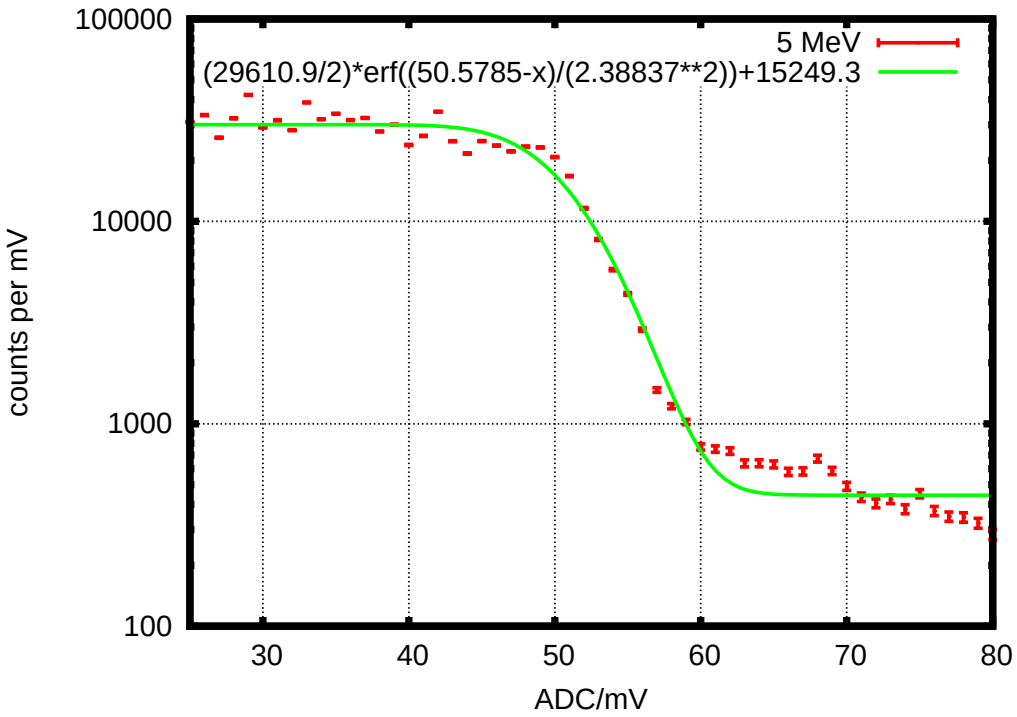

Figure 5.2: *5 MeV neutron spectrum with fit to the neutron edge*

The positions of the different neutron edges are summarized in Table 5.1. The errors listed here are the errors for the neutron edge positions b given by the fit programme that was used. Note that for the neutron calibration measurements the background was not taken into account because it is very low in the regions of the spectra where the neutron edges are located. For the 5 MeV, 14.8 MeV and 19 MeV measurements the background is about two

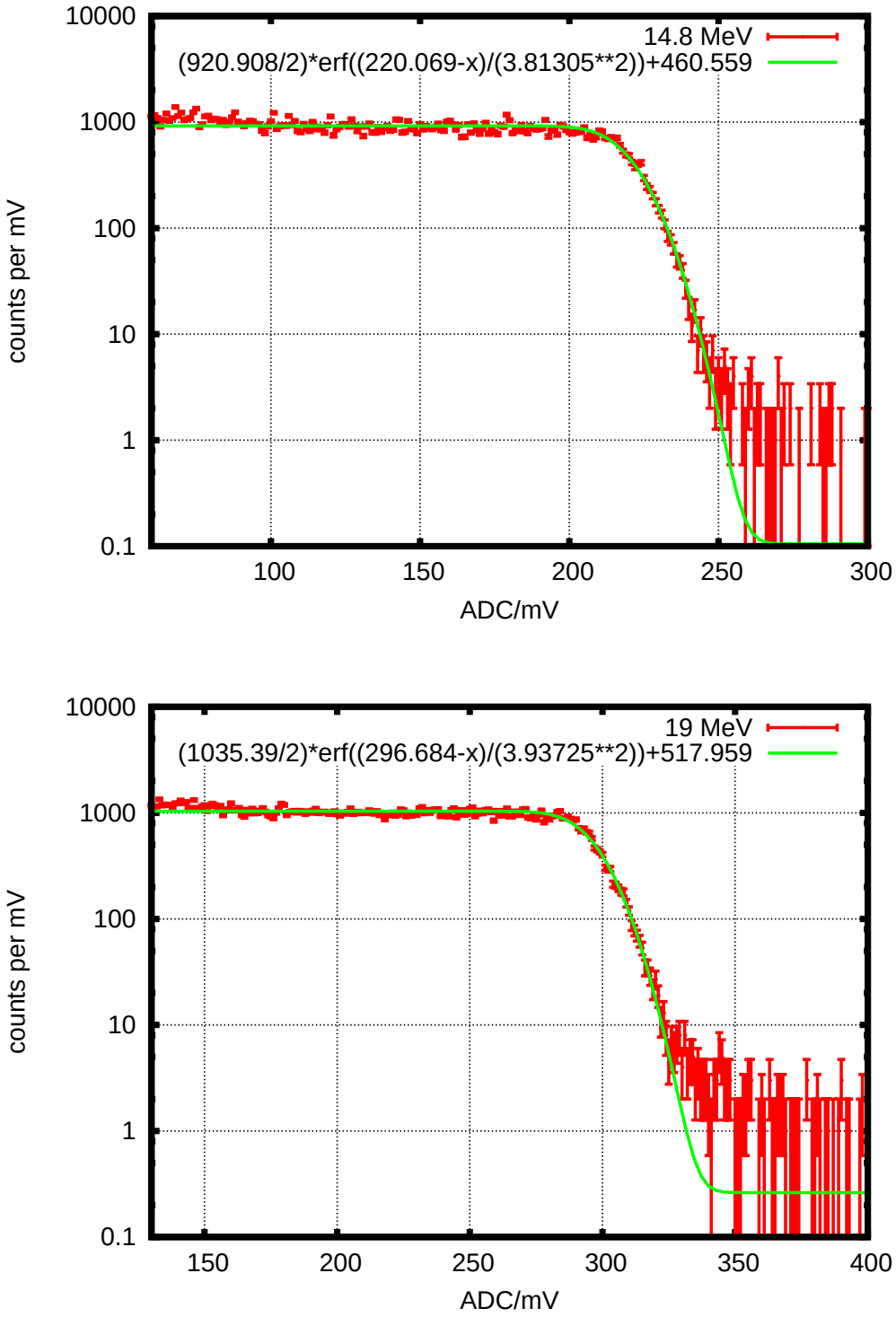

Figure 5.3: *14.8 MeV (upper panel) and 19 MeV (lower panel) neutron spectrum with fit to the neutron edge*

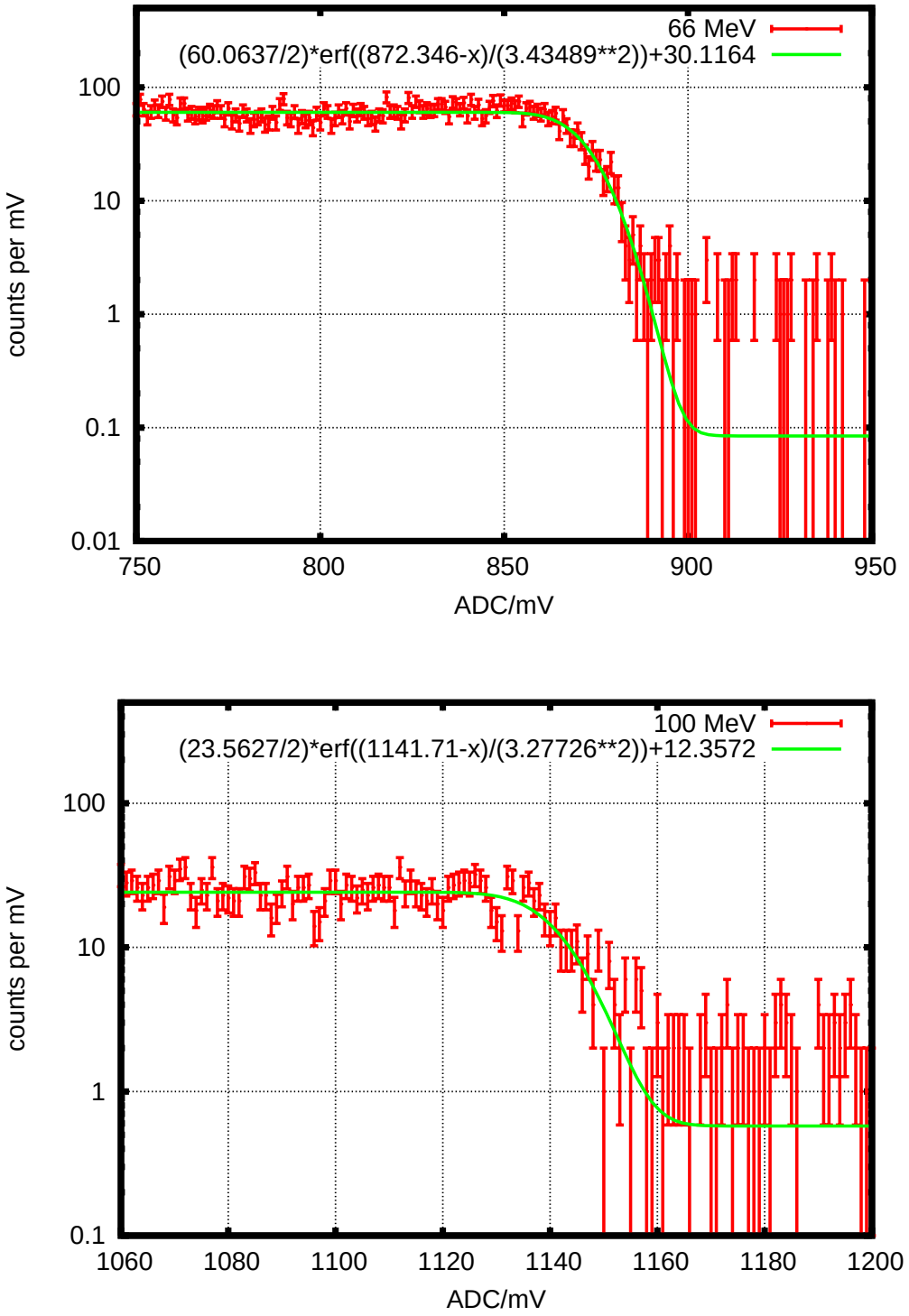

Figure 5.4: *66 MeV (upper panel) and 100 MeV (lower panel) neutron spectrum with fit to the neutron edge*

Energy [MeV]	Voltage at ADC [mV]	Error [mV]
5	50.6	± 0.3
14.8	220.1	± 0.5
19	296.7	± 0.3
66	872.3	± 0.5
100	1141.7	± 1.0

Table 5.1: *Energies and neutron edge positions for the neutron calibration*

orders of magnitude smaller than the neutron measurement. Thus, it does not effect the position of the neutron edges. For the 66 MeV and 100 MeV measurements the background is only about one order of magnitude smaller than the neutron spectrum in the region of the neutron edge. But when the position of the neutron edge is determined with and without subtraction of the background the difference in the position is only 0.3 % and 0.2 %, respectively.

The calibration curve for the neutrons in the plastic scintillator is non-linear and the function which is used to fit the data is the following:

$$y = \frac{A \cdot x}{1 + B \cdot x} + C \tag{5.2}$$

In Fig. 5.5 equation (5.2) is used to fit the points for the neutron calibration. This yields the following fit function:

$$y[\text{mV}] = \frac{(20.7 \pm 0.6) \cdot x[\text{MeV}]}{1 + (0.0073 \pm 0.0005) \cdot x[\text{MeV}]} - 50.0 \pm 5 \tag{5.3}$$

The resulting formula for the energy calibration is:

$$\text{energy}[\text{MeV}] = \frac{\text{voltage}[\text{mV}] + 50.0}{20.7 - 0.0073 \cdot \text{voltage}[\text{mV}] - 0.365} \tag{5.4}$$

It is assumed that all the measured neutron edges which have been used for the neutron calibration are caused by recoil protons. Thus, the energy calibration function given in equation (5.4) describes events in the plastic scintillator which involve elastic scattering of neutrons at hydrogen nuclei. This calibration function is only valid for energies up to 100 MeV, the extrapolation to higher energies is not allowed because it has no physical justification. All events in the plastic detector that result in larger energy deposits result from reactions other than elastic scattering and do not follow this energy calibration function, but since the detector efficiency for neutrons drops down

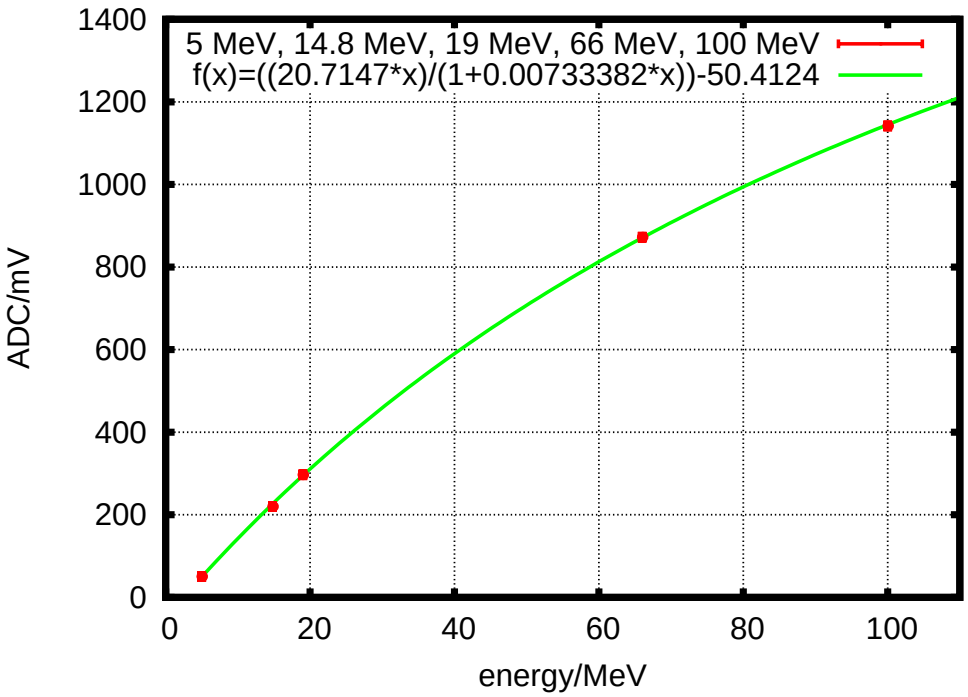

Figure 5.5: *Neutron calibration curve: measured voltages at the ADC in mV plotted versus the energies of the incident neutrons*

significantly above 100 MeV not many events with energy deposits above 100 MeV occur.

The two additional peaks in the 66 MeV and 100 MeV neutron spectra with the energies 51 MeV and 85 MeV are roughly located at 670 mV and 980 mV, respectively. In Fig. 5.6 these two additional points are plotted together with the neutron calibration function. They agree reasonably well with the calibration function which is an indication that the assumption that the additional peaks originate from the neutron capture reaction C(n,d) is correct. However the additional peaks lie under the calibration curve. This can be explained because as mentioned above the calibration curve describes recoil protons and in the reactions that cause the 51 MeV and 85 MeV peak heavier recoil particles are measured. These particles are more affected by quenching and thus less light will be produced for the same amount of incident energy which leads to a lower measured voltage.

The threshold for neutrons in the plastic scintillator is 25 mV which equals 3.74 MeV. Therefore the energy range for neutrons in the BC-412 scintillator goes from 3.74 MeV to 100 MeV.

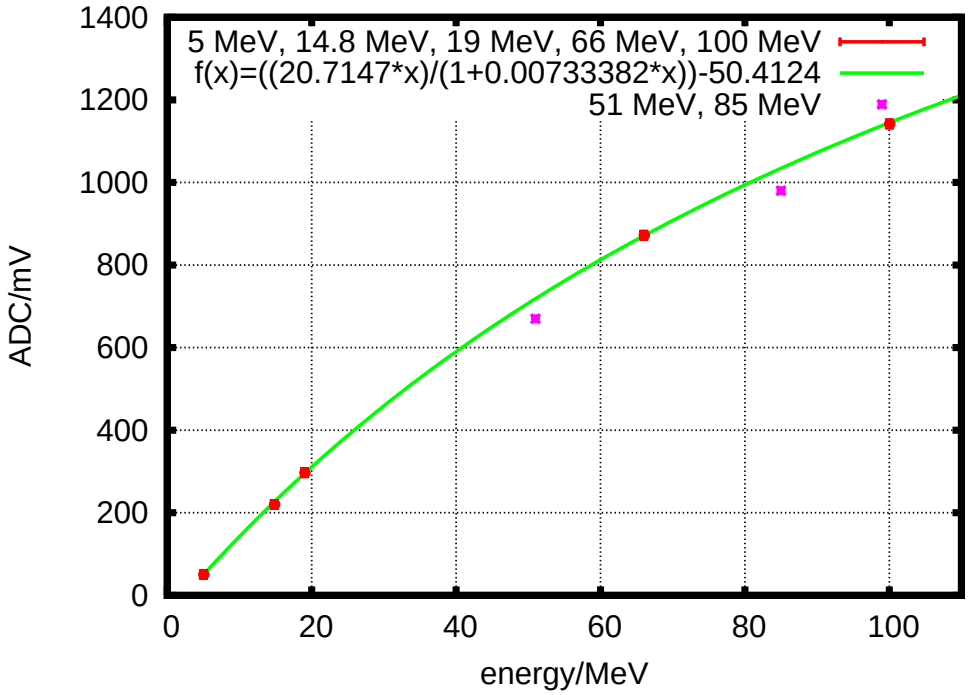

Figure 5.6: *Neutron calibration curve with the two additional points at 51 MeV and 85 MeV*

5.2 Calibration With γ-Rays

The γ-ray calibration with the sources bismuth (^{207}Bi), caesium (^{137}Cs) and cobalt (^{60}Co) was performed at the University of Kiel. For these measurements the sensor head was in a horizontal position with the sources in a distance of 10 cm parallel to the sensor head.
For the energy calibration first the background caused by the γ-ray source itself and the inherent radioactivity from the CsI(Na) scintillator is subtracted from the measured spectrum. In the resulting spectra a fit using the Gaussian distribution is applied to the photopeaks:

$$f(x) = c \cdot \exp\left(-0.5 \cdot \frac{(x-a)^2}{b^2} \right) \tag{5.5}$$

with the peak position a, b: the standard deviation σ and the amplitude c.
As an example this procedure is shown for the measured ^{207}Bi spectrum in Fig. 5.7. Here the measured spectrum is displayed in red, the background given by an exponential function is shown in green, the resulting spectrum

in blue and the fit to the photopeak in pink. In Figs. 5.8 and 5.9 the spectra

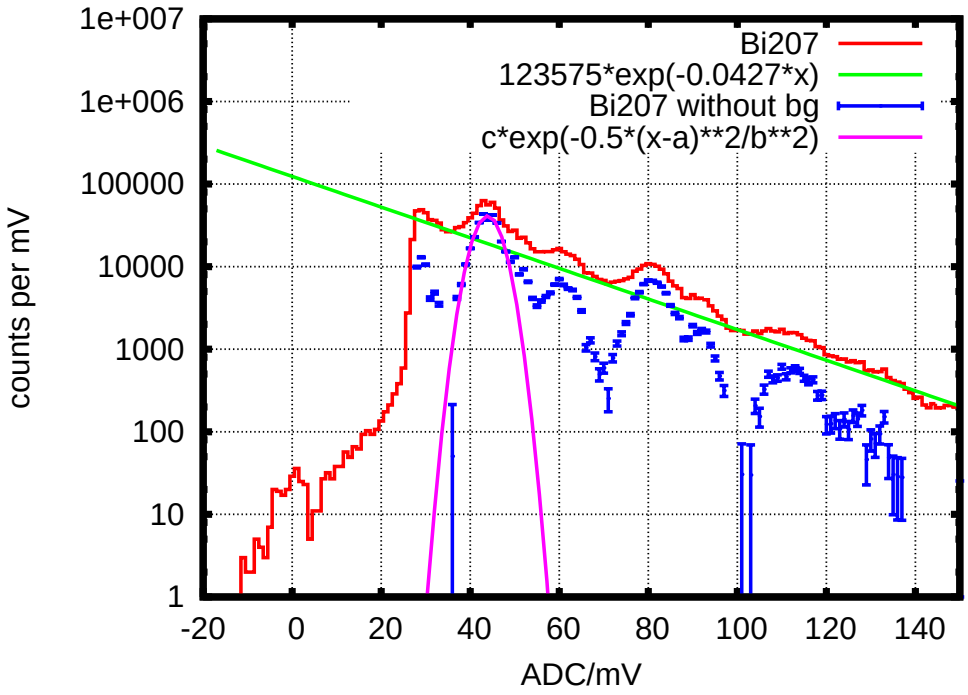

Figure 5.7: *^{207}Bi spectrum (red), background (green), spectrum without background (blue) and the fit to the first photopeak (pink)*

for ^{207}Bi, ^{137}Cs and ^{60}Co are displayed, respectively. In the lower panel of Fig. 5.9 a background spectrum is shown. This spectrum features only the photopeaks originating from the inherent radioactivity of CsI(Na). In the ^{207}Bi spectrum there are three other features which are not used for the calibration. The two features at about 65 mV and 94 mV have energies of about 854 keV and 1246 keV, respectively and can be identified as the Compton edges belonging to the second photopeak of ^{207}Bi and the ^{40}K photopeak. The peak at 108 mV is the ^{40}K photopeak from the inherent radioactivity. This peak is the one that is used for the calibration in the lower panel of Fig. 5.9.
In the ^{137}Cs spectrum there seems to be an additional peak above 661.657 keV but in the literature no energies higher than the 661.657 keV photopeak can be found for ^{137}Cs (NuDat2, 15.11.2012). When plotting the spectrum with a linear y-axis it becomes clear that the additional peak is more than one order of magnitude smaller that the photopeak at 661.657 keV.

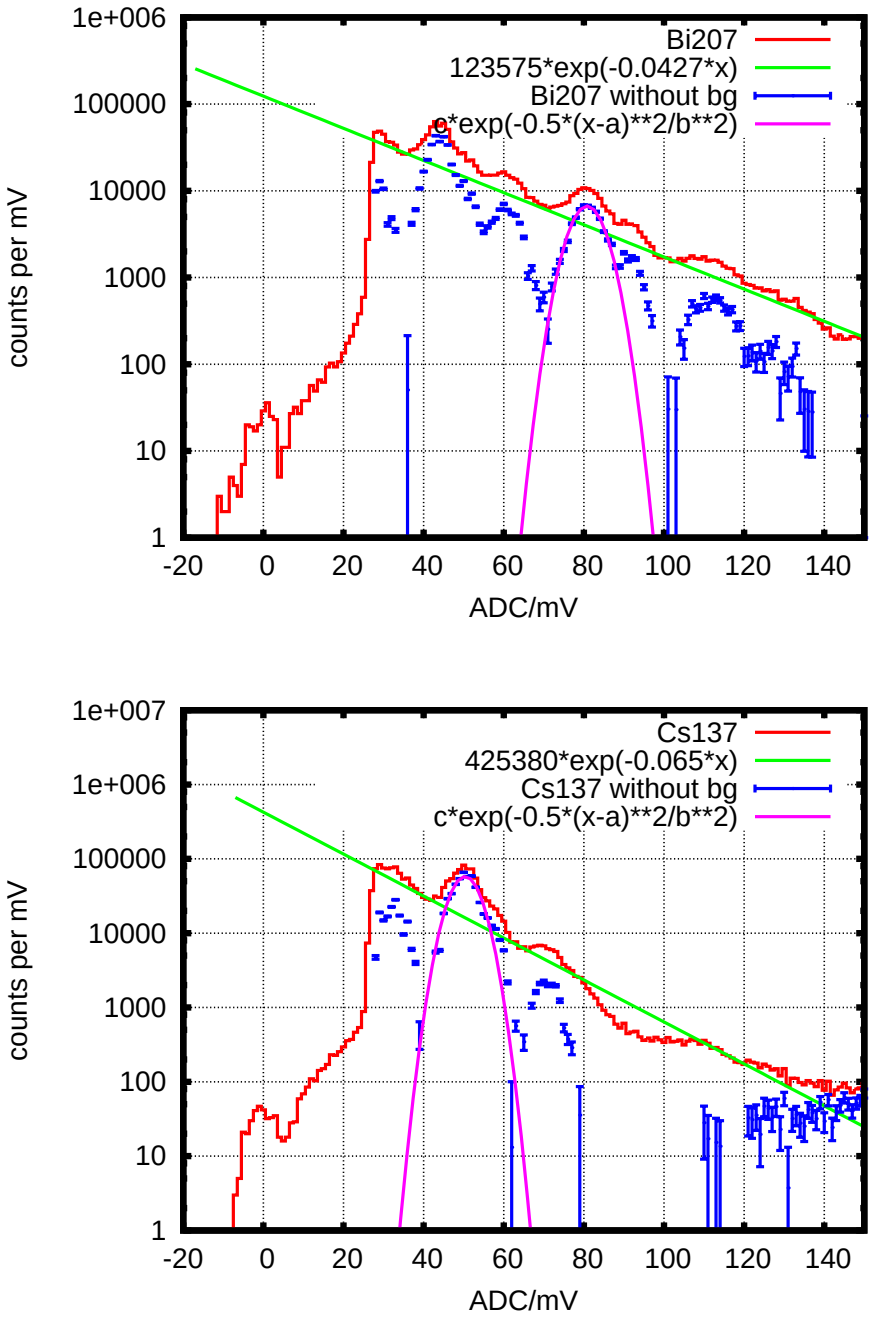

Figure 5.8: *Upper panel:* ^{207}*Bi spectrum (red), background (green), spectrum without background (blue) and the fit to the second photopeak (pink). Lower panel: the same for the* ^{137}*Cs spectrum*

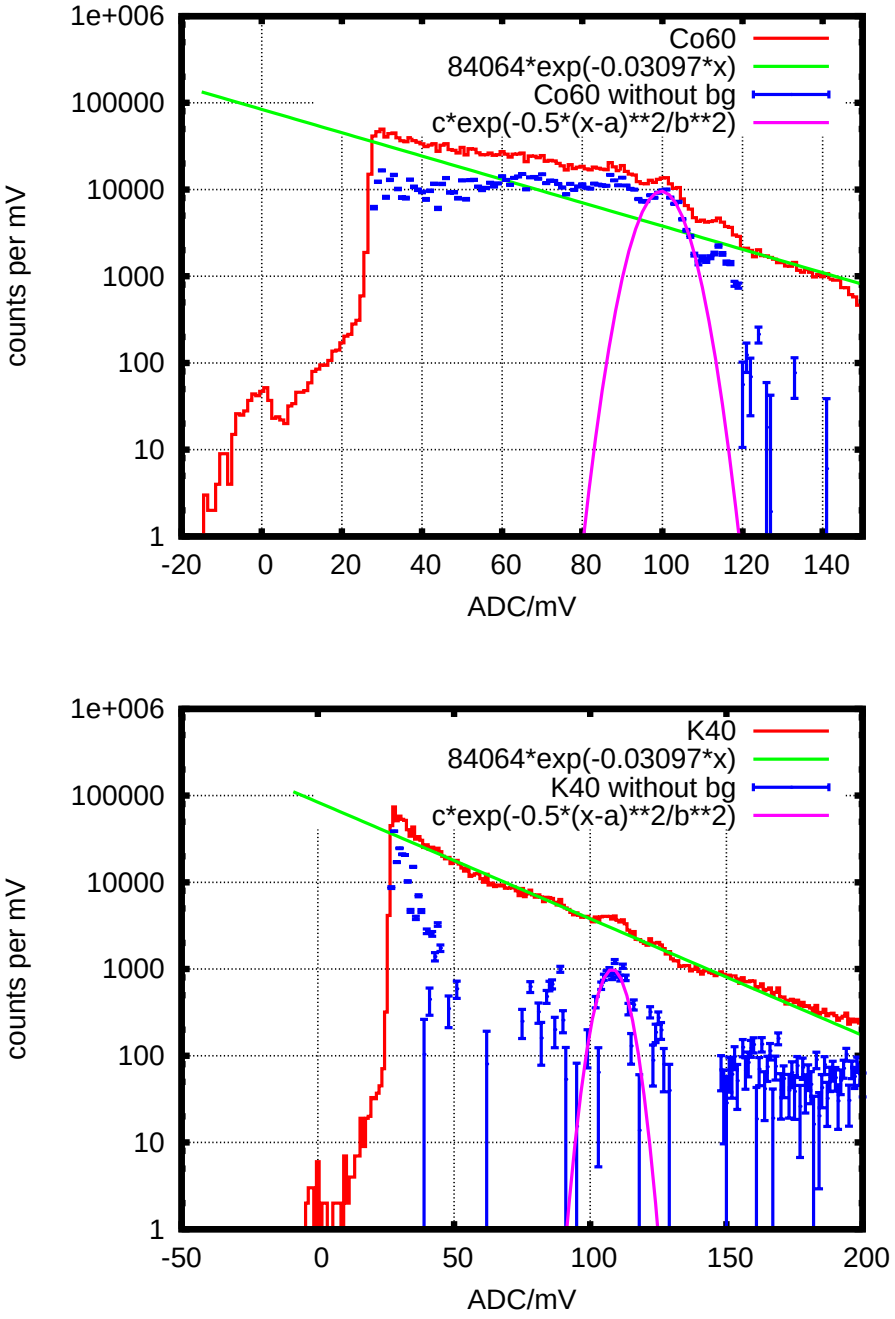

Figure 5.9: *Upper panel:* ^{60}Co *spectrum (red), background (green), spectrum without background (blue) and the fit to the second photopeak (pink). Lower panel: background measurement with the photopeak of* ^{40}K *which originates from the inherent radioactivity of CsI(Na)*

The positions of the different γ-ray photopeaks used for the energy calibration are listed in Table 5.2. The errors given here are the errors for the positions a provided by the fit programme that was used. The energies of

Energy [keV]	Source	Voltage at ADC [mV]	Error [mV]
569.698	^{207}Bi	43.91	$\pm$ 0.11
661.657	^{137}Cs	50.36	$\pm$ 0.20
1063.656	^{207}Bi	80.81	$\pm$ 0.13
1332.492	^{60}Co	99.7	$\pm$ 0.3
1460.822	CsI(Na)	108.1	$\pm$ 0.7

Table 5.2: *Energies and photopeak positions for the γ-ray calibration*

the photopeaks can be found in the NuDat2 database (NuDat2, 15.11.2012). In Fig. 5.10 the calibration curve for γ-rays is shown. Fitting the data with

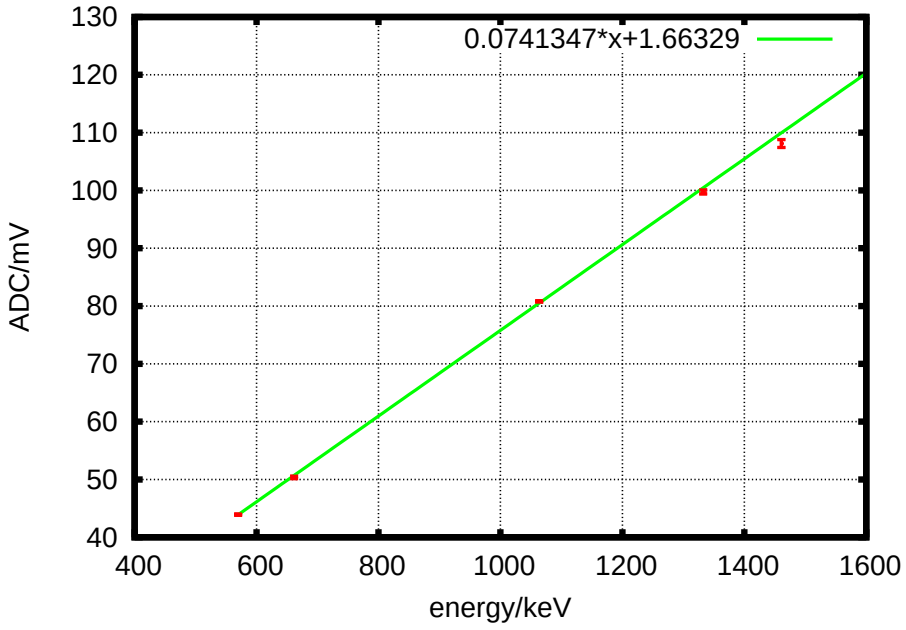

Figure 5.10: *γ-ray calibration curve: measured voltages at the ADC in mV plotted versus the energies of the incident γ-rays*

a linear function yields the following:

$$y[\text{mV}] = (0.0741 \pm 0.0007) \cdot x[\text{keV}] + (1.7 \pm 0.6) \tag{5.6}$$

The voltage to energy calibration for γ-rays in CsI(Na) then is:

$$\text{energy [keV]} = (\text{voltage[mV]} - 1.7)/0.0741 \tag{5.7}$$

Thus, the energy range for γ-rays in the CsI(Na) scintillator is from about 328 keV (equals 25 mV) to 44 MeV (equals 3250 mV).

5.3 Response of the Plastic Scintillator to Gamma Rays

As discussed in the previous chapters the plastic scintillator is sensitive to neutrons because of its hydrogen content whereas the CsI(Na) is sensitive to γ-rays because of its high atomic number Z. However, this does not imply that the plastic scintillator will not respond to γ-rays at all. Figure 5.11 shows the spectra of events only in the plastic scintillator for the three measurements with γ-ray sources (^{207}Bi, ^{137}Cs and ^{60}Co) and the background measurement (containing γ-rays originating from ^{40}K) used for the calibration in Section 5.2. γ-rays with energies between about 300 keV and 30 MeV will most probably interact with the plastic scintillator via Compton scattering, thus the spectra in the plastic scintillator feature mainly the Compton continuum including the Compton edge. The energies of the Compton edges corresponding to the γ-ray energies used for the calibration in Section 5.2 can be calculated using equation (2.8) and are summarized in table 5.3.

The Compton edge of ^{40}K can be identified in the background spectrum

Energy of photopeak [keV]	Source	Energy of Compton Edge [keV]
569.698	^{207}Bi	393.307
661.657	^{137}Cs	477.334
1063.656	^{207}Bi	857.642
1332.492	^{60}Co	1118.101
1460.822	^{40}K	1243.357

Table 5.3: *Energies of photopeaks and Compton edges*

in Figure 5.11 at about 58 mV. As the ^{40}K-γ-rays originate from the inherent radioactivity of CsI(Na), this Compton edge should be found in all the measurements in Figure 5.11. It seems to be the case that there is an edge

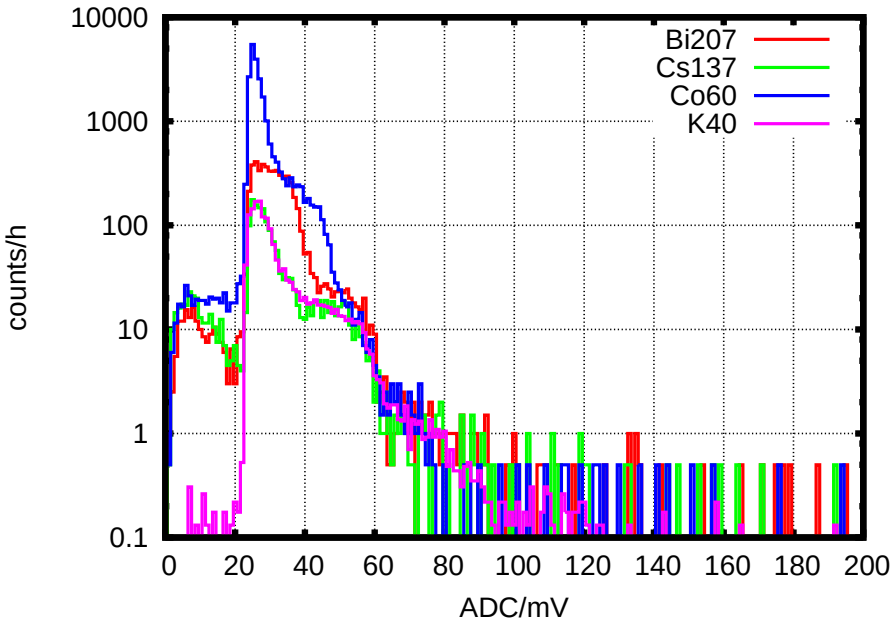

Figure 5.11: *Spectra of events only in the plastic scintillator for the background measurement (containing γ-rays originating from ^{40}K) and measurements with ^{207}Bi, ^{137}Cs and ^{60}Co*

in all four measurements at around 58 mV to 60 mV. Assuming that the response of the plastic scintillator to γ-rays in the energy range up to a few MeV is roughly linear, the edge in the spectrum of ^{207}Bi at about 38 mV can be identified as the Compton edge corresponding to the 1063.656 keV-γ-rays. The Compton edges of the 569.698 keV-γ-rays (^{207}Bi) as well as the Compton edge of the 661.657 keV-γ-rays (^{137}Cs) cannot be found in the spectra because they are below the threshold. ^{60}Co emits γ-rays at energies of 1332.492 keV and 1173.228 keV (the latter were not used for the calibration in Section 5.2). In the ^{60}Co spectrum in Figure 5.11 the two Compton edges are not well separated, instead only one edge is visible which most probably results from the overlap of the two.

In order to get an estimate of how much the γ-rays contribute to the total signal measured in the plastic scintillator the response of the plastic scintillator, as part of the Phoswich detector, to neutrons and γ-rays has been simulated (Marquardt, 2012, 2013) with GEANT4. The results of the simulation are displayed in Figure 5.12. Shown here is the number of particles recorded in the plastic scintillator normalized to the number of all incident particles versus the energy of the incoming particle. Figure 5.12 shows that

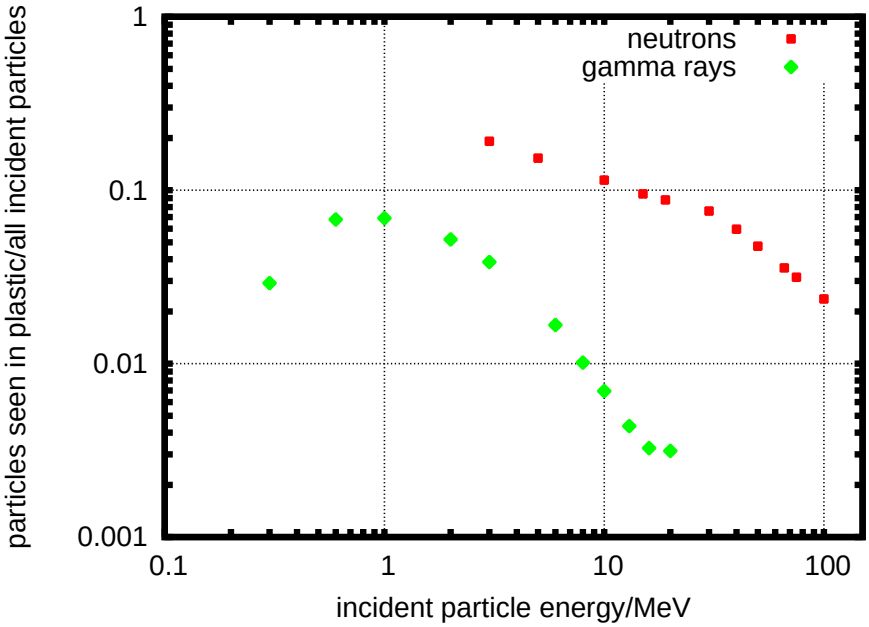

Figure 5.12: *Simulated response of the plastic scintillator, as part of the Phoswich detector, to neutrons and γ-rays (Marquardt, 2012, 2013)*

both the response to neutrons as well as to γ-rays decreases with increasing incident energy, but it is clearly visible that the response of the plastic scintillator to neutrons is greater than that to γ-rays. For an incident energy of 3 MeV the detection probability for neutrons is already five times as high as for γ-rays and for an incident energy of 10 MeV it is even more than 16 times as high. The simulation results show that γ-rays cannot be neglected in the response of the plastic scintillator but their significance decreases rapidly with increasing energy.

Chapter 6

Test Measurements

When performing a balloon flight in the Earth's atmosphere there are certain constraints that have to be taken into account. At an altitude of approximately 30 km the pressure drops down to about 10 mbar while the ambient temperature can reach a minimum of about - 55°C. Thus, in preparation for the balloon flights the Phoswich detector has to be tested under low pressure and low temperature conditions. In this chapter the necessary test measurements for the balloon flight with the Phoswich detector are discussed.

6.1 Low Pressure Conditions

Since the photomultiplier in the Phoswich detector is powered with - 867 V bias voltage, corona discharges could occur when measuring under low pressure conditions. That would jeopardize the measurements on board the balloon. To qualify the instrument for the low pressure conditions during a balloon flight tests inside a vacuum chamber were performed at the University of Kiel.
The Phoswich detector was placed in the vacuum chamber and the pressure was reduced to about 1 mbar while the data were recorded online. It became obvious that the instrument was not performing nominally because the count rate was reduced while decreasing the pressure. The count rate even dropped down to zero count, so that the measurement stopped.
To investigate why the count rate was reduced and the measurement terminated the high voltage was monitored while reducing the pressure. It was found out that the high voltage broke down. Thus, the reduction in count rates and the termination of the measurement were due to a loss of high voltage. Corona discharges can cause a loss of high voltage. There are three different locations within the instrument where these could occur: at the high

voltage power supply unit, at the high voltage connector which connects the high voltage cable with the read-out electronics and between the PMT and the socket.

6.2 Countermeasures Against Corona Discharges

When performing a measurement with an open electronics box in the vacuum chamber one could see that discharges occurred at the high voltage power supply. To avoid these discharges the high voltage DC-DC-converter was encapsulated with the silicone adhesive Nusil CV-1152 (Nusil Silicone Technology, 09.02.2011). Because the high voltage still broke down the connector for the high voltage was sealed with Teflon® tape. It was wrapped around the inner conductor to achieve better insulation between high voltage and ground. The pictures in 6.1 show the coating with Nusil on the left side and where the high voltage connector is sealed on the right side.
The instrument still did not work nominal under low pressure conditions and connecting the PMT permanently to the socket with the space-grade encapsulant Dow Corning®93-500 (Dow Corning, 07.12.2012) was not successful.

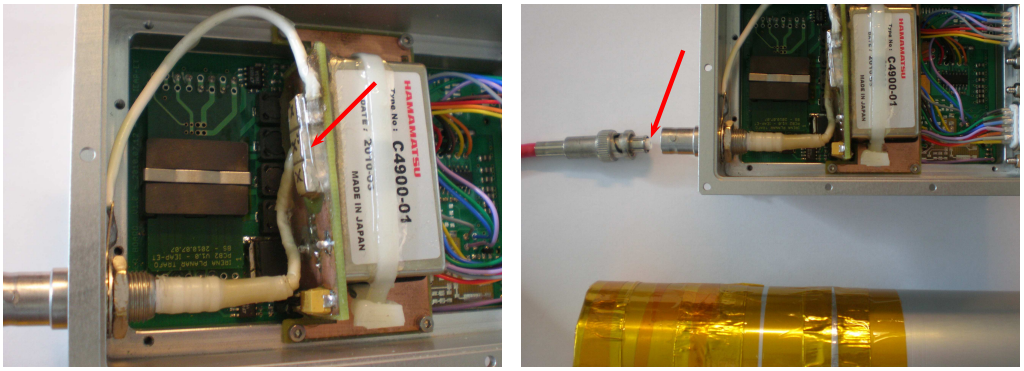

Figure 6.1: *Left side: The arrow indicates where the high voltage power supply is coated with Nusil (Nusil Silicone Technology, 09.02.2011). Right side: the arrow indicates where the high voltage connector is sealed*

The solution to avoid any corona discharge was to seal the whole sensor head in order to maintain standard pressure inside the housing. This was done by sealing the threads and the cable feedthrough with the sealant Teroson

Terostat-IX, aluminium tape and Kapton® tape. After all these countermeasures had been taken no discharges occurred.

6.3 Thermal Vacuum

To test the Phoswich detector under low pressure and low temperature conditions measurements inside a thermal vacuum chamber were performed. For these measurements the instrument was insulated with 3 cm of polystyrene and placed on top of the cooling plate inside the thermal vacuum chamber. The insulated detector was covered by a shroud to ensure cooling from all sides. In Fig. 6.2 the thermal vacuum chamber with the instrument inside can be seen. During the whole test the data were recorded via UBS and on the SD card.

Figure 6.2: *The thermal vacuum chamber with the cooling plate and the insulated instrument. The shroud is lying in front of the chamber*

At the beginning of the test the pressure inside the chamber was reduced to about 10 mbar while the cryostat cooled down the cooling plate to -50°C. In Fig. 6.3 a time profile of the measurement is shown. Displayed here is the count rate of the instrument via USB and SD card as well as two pressure

curves. The blue line shows the pressure of the vacuum chamber itself and the pink line indicates the pressure recorded by the pressure sensor of the instrument. As this pressure sensor is situated inside the read-out electronics it is a bit behind the pressure of the chamber. However, during the first four hours of the measurement this effect was only 5 mbar at most. Only when the thermal vacuum chamber is aerated again the pressure sensor of the instrument lags behind.
Note that the count rates shown in this chapter are from the raw data because the aim here is only to show that the instrument basically works under low pressure and low temperature conditions.

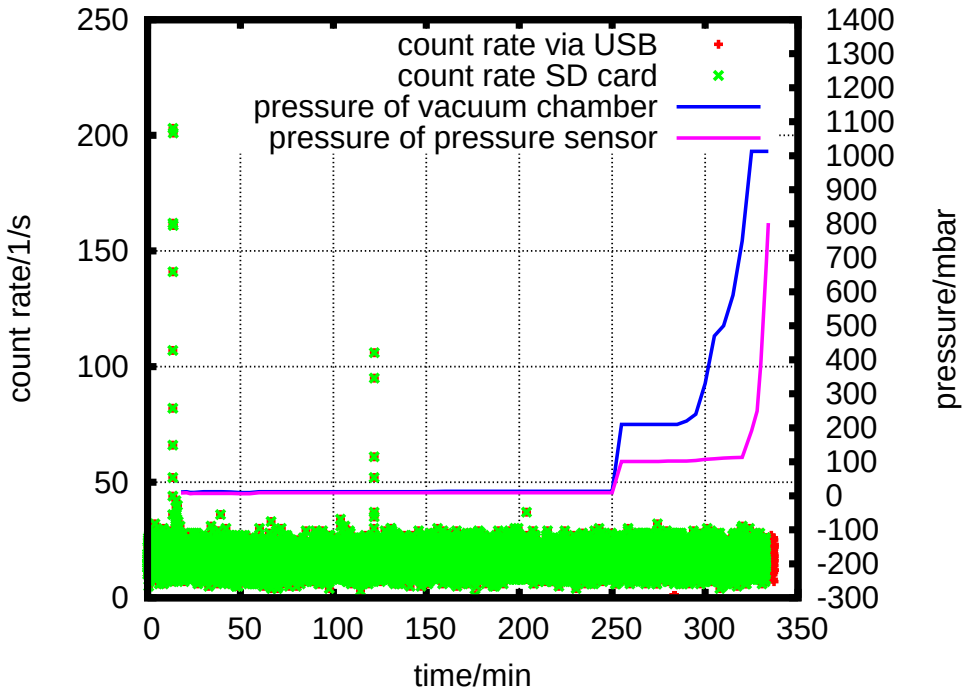

Figure 6.3: *Time profile of the thermal vacuum measurement. Shown here are count rates via USB and on the SD card as well as the pressure of the chamber itself and the pressure recorded by the pressure sensor of the instrument*

When comparing the count rates via USB and SD card it is obvious that they are identical except for the last four minutes of the measurement which is as expected because writing on the SD card is stopped when the pressures rises above 800 mbar. This was implemented to protect the SD card during

the descent phase of the balloon flight in case the SD card moves inside the card holder during impact.
More important to point out in Fig. 6.3 is that the count rate of the instrument was stable during the whole test measurement regardless of the pressure changes. In the first part of the test the instrument measured successfully at about 10 mbar for almost four hours. This is the pressure where the probability for corona discharge is highest. Then the pressure was raised to about 200 mbar for 40 minutes before it was increased to standard pressure again. The detector showed stable count rates with two exceptions where the count rate abruptly increased. The reason for this are electrostatic discharges which happen when for example the vacuum pump is turned on. In summary the count rates of the Phoswich detector were not affected by any change in ambient pressure.

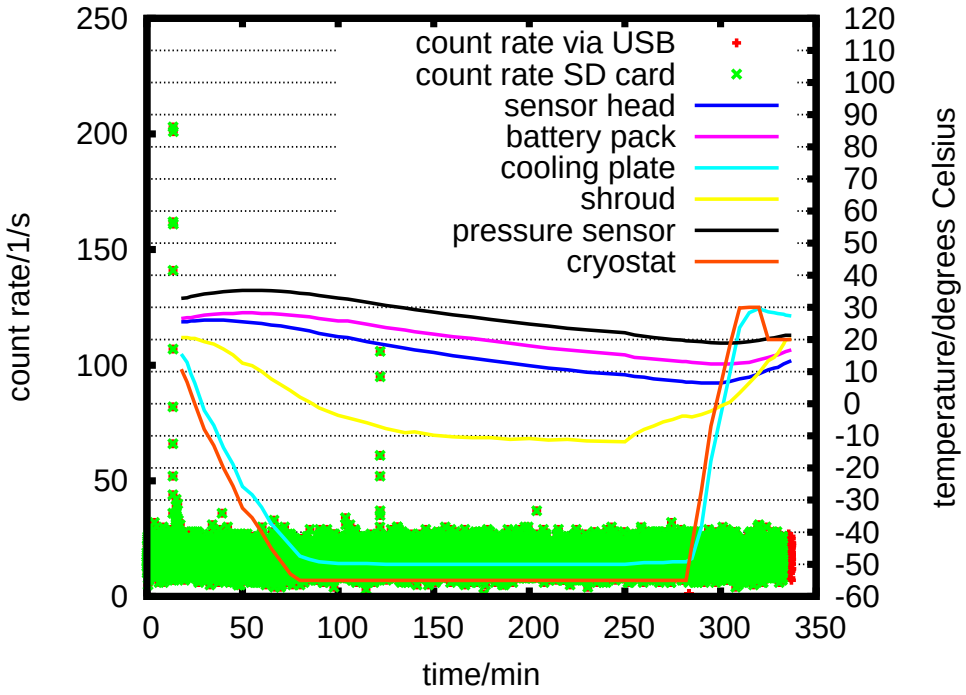

Figure 6.4: *Time profile of the thermal vacuum measurement. The count rates via USB and on the SD card are shown. In addition temperatures recorded at five different locations as well as the temperature of the cryostat are displayed*

In Fig. 6.4 the time profile of the measurement is shown again. In addition

to the count rates the temperatures recorded at five different locations as well as the temperature of the cryostat are shown here.
The four temperatures at the sensor head, the battery pack, the cooling plate and the shroud have been measured with a temperature sensor PT1000 (see e.g. Rinck Electronic GmbH, 08.10.2012). The temperature referred to as 'pressure sensor' is the temperature measured by the temperature sensor integrated in the pressure sensor of the instrument. The temperature indicated as 'cryostat' is the temperature with which the cryostat cools the cooling plate.
Fig. 6.4 clearly shows that the count rate of the instrument does not change with changing ambient temperature. The detector was cooled with - 50°C for three hours and the part of the instrument that cooled down most was the sensor head. But with a minimum of about 6.5°C its temperature stayed well above 0°C.

In summary the Phoswich detector was tested under conditions similar to the conditions in the stratosphere for more than five hours with four hours of low pressure conditions and a period of cooling with - 50°C for three hours. The count rate of the instrument was constant for the whole time regardless of the changing pressure and changing temperature.
In this test the instrument was insulated with 3 cm of polystyrene and it did not get too cold. In the stratosphere the instrument will be cooled with the same low temperature from all directions. This could not be realized in the thermal vacuum chamber because the shroud reached only about -10°C instead of - 50°C. Thus the insulation for the instrument will be increased to 5 cm of polystyrene for the balloon flight.

Chapter 7

Measurements on Board Aircraft

After the Phoswich detector had been calibrated and tested under stratospheric conditions, measurements on board aircraft were performed to test the instrument in the atmospheric radiation field. This chapter describes these measurements and shows how the dose rates for the events in the different scintillators are calculated. In July 2011 measurements on board an aircraft have been performed on a flight from Hamburg to the Canary Islands and back. The Phoswich instrument was switched on at about 15 minutes after the start and measured during both flights as well as during the stopover. In Fig. 7.1 the processed data of this measurement are displayed analogue to the plot in Fig. 4.4. It is clearly visible that the processed data from the flight contain the additional branch which was mentioned in Chapter 4 and is discussed in Appendix *B*. The additional branch is treated as belonging to the events in CsI(Na).

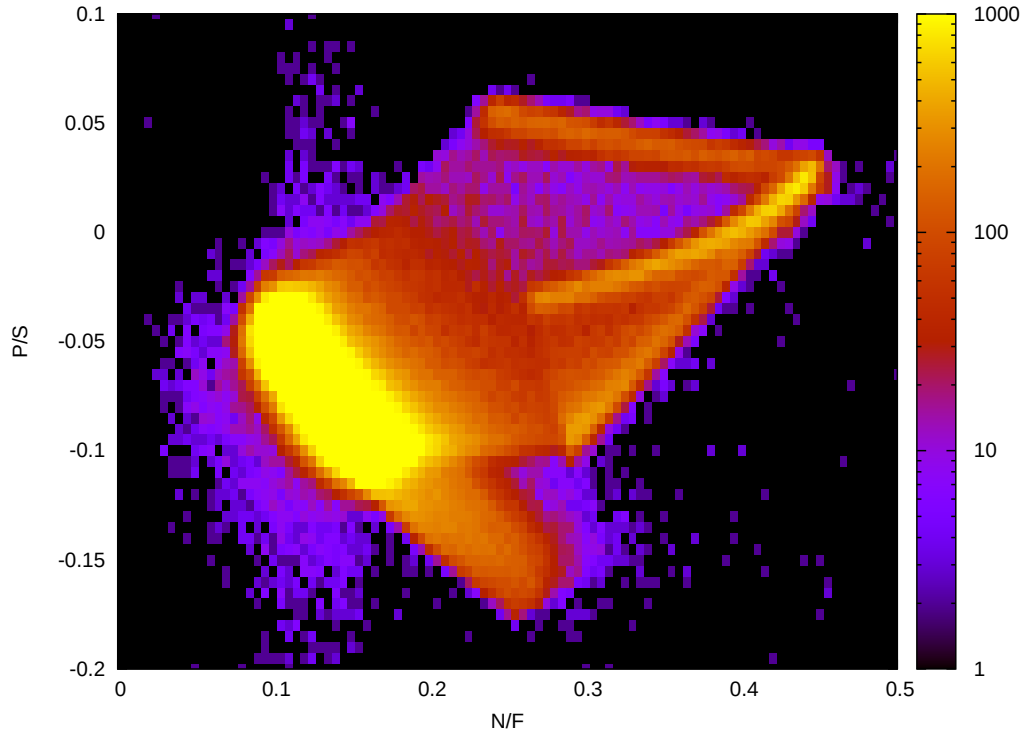

Figure 7.1: *Processed data of the flight measurement on the route Hamburg-Canary Islands-Hamburg*

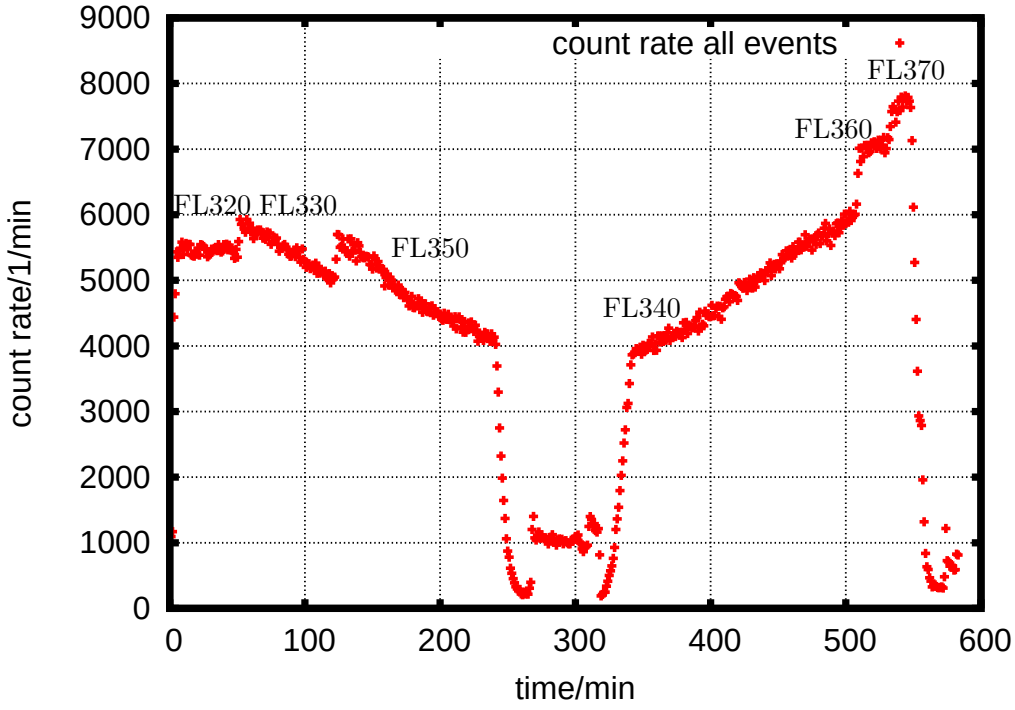

Figure 7.2: *Count rates profile from all events in the instrument. The numbers indicate the flight levels*

In Fig. 7.2 the count rate profile for the flight Hamburg-Canary Islands-Hamburg is shown. These count rates are calculated from all events of the instrument, meaning that no separation between events in the different scintillators has been applied yet. Plotted here are counts per minute versus the time in minutes. In addition to the count rates the flight levels, which are a standard altitude used in aviation, are given. The flight level is a pressure altitude which expresses the altitude in hundreds of feet. Therefore, flight level FL340 equals an altitude of 34000 feet. The characteristic count rate profile seen in Fig. 7.2 is caused by two different effects: on the one hand it is visible that the count rate increases with increasing flight level. This is due to the fact that the shielding effect of the residual atmosphere decreases with increasing altitude. Thus, the intensity of secondary particles is higher at higher altitudes (up to the Pfotzer maximum at approximately 20 km (see Section 2.4.4)) which leads to higher count rates at higher altitudes. On the other hand it can be observed that the count rate decreases with decreasing latitude. This is caused by the shielding effect of the Earth's magnetic field which is strongest at the magnetic equator and becomes less at higher latitudes (see Section 2.4.3). The fact that at lower latitudes more incoming

particles are deflected by the Earth's magnetic field due to the Lorentz force leads to decreasing count rates at lower latitudes.
Between the two flights and at the end of the return flight the count rate first decreases when leaving ground before increasing with increasing altitude. This is caused by terrestrial radiation which features strong γ-ray photopeaks (see e.g GeoExplo Ltda., 22.11.12). Because the CsI(Na) scintillator is very sensitive to γ-rays the count rate increases considerably on ground.
To determine the dose rates of events in CsI(Na) and events in BC-412 the processed data in Fig. 7.1 first have to be separated as explained in Chapter 4. The cuts used to separate events in BC-412 from events in CsI(Na) in the flight data are very similar to the ones applied for the 14 MeV neutron data in Chapter 4. After the separation of the particles, separate count rates can be calculated for events in BC-412 and events in CsI(Na) which are illustrated in Fig. 7.3. Please note the different axes since the count

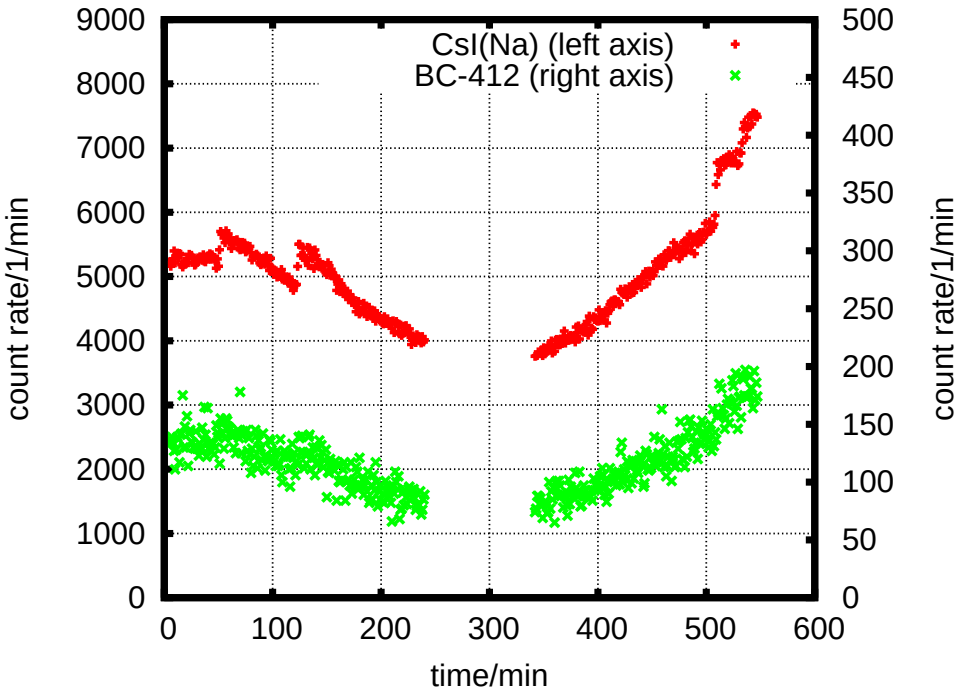

Figure 7.3: *Count rates of events in CsI(Na) and BC-412 at flight altitudes*

rates of events in BC-412 are more than one order of magnitude smaller than those of the events in CsI(Na).
Fig. 7.4 shows spectra of the events in CsI(Na) and BC-412 for all the flight levels shown in Fig. 7.2 compared to a measurement on ground.

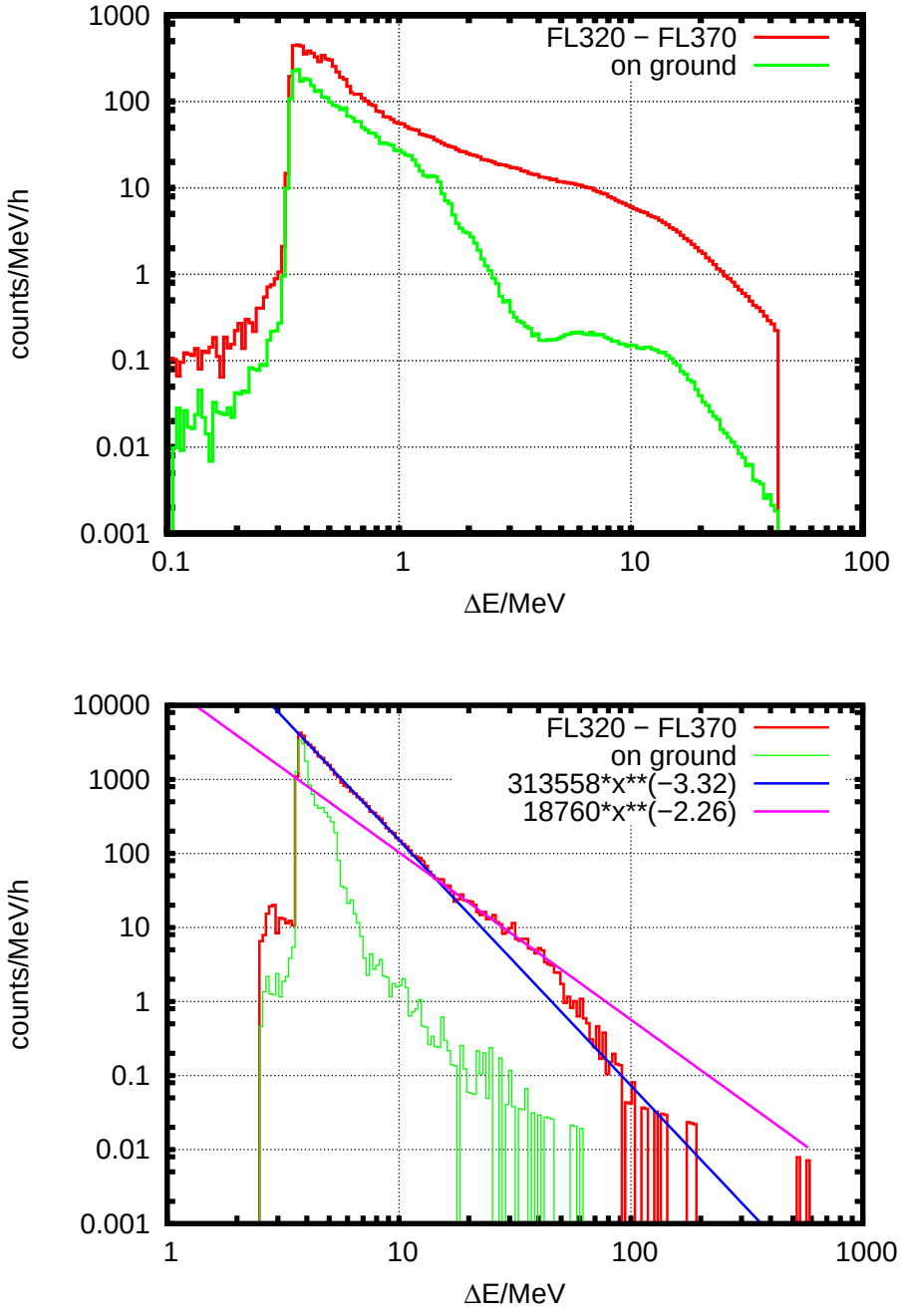

Figure 7.4: *Upper panel: Spectra of events in CsI(Na) for a measurement on ground and for the flight levels shown in Fig. 7.2. Lower panel: Spectra of events in BC-412 for the same measurements as in the upper panel*

The upper panel of Fig. 7.4 shows the spectra for events in CsI(Na) and the lower panel the ones for events in BC-412. Displayed are the counts per energy and per hour. The measurement on ground is similar to the one used for the energy calibration of the CsI(Na) with γ-rays. Thus, the ground spectrum of events in CsI(Na) shown in the upper panel of Fig. 7.4 can be compared to the spectrum shown in the lower panel of Fig. 5.9 and the ground spectrum of events in BC-412 shown in the lower panel of Fig. 7.4 can be compared to the spectrum denoted as 'K40' in Fig. 5.11. The only difference of the measurement used for the calibration and the measurement used for the comparison with the spectra from the flight levels is that the latter was performed with the sensor head in a vertical position which is the same position the instrument normally has during flight.
As described in Chapter 5 the ground measurement features mostly γ-rays originating from the inherent radioactivity of CsI(Na). Therefore, the ground spectrum of events in CsI(Na) displayed in the upper panel of Fig. 7.4 shows the photopeak of ^{40}K at 1.46 MeV which was used for the calibration. The broad distribution between 4 and roughly 15 MeV in this spectrum is most probably caused by cosmic muons. For the energy conversion of the events in CsI(Na) the calibration function for γ-rays given in equation (5.7) is used. The spectra of events in CsI(Na) contain mainly γ-rays and charged particles since charged particles cannot be distinguished easily from γ-rays (refer to Section 4.2 for details).
As mentioned above the ground spectrum of events in BC-412 shown in the lower panel of Fig. 7.4 corresponds to the spectrum referred to as 'K40' in Fig. 5.11. In the description of Fig. 5.11 it is mentioned that the ground spectrum of events in BC-412 features mainly Compton electrons. For the ground spectrum in the lower panel of Fig. 7.4 all events in BC-412 were converted into energy using the neutron calibration function in equation (5.4). This means all events were treated as if they were neutron events. As neutron and γ-ray events have different energy scales in the plastic scintillator the result of converting all events in BC-412 into energy via the neutron calibration function is that the Compton edges discussed in Section 5.3 appear at higher energies in the spectrum than at the energies which have been calculated for the Compton edges (see table 5.3). However, by displaying this ground spectrum of events in BC-412, converted into energy using the neutron calibration function for all events, in comparison with a spectrum at all flight levels as done in the lower panel of Fig. 7.4 it becomes clear until which energy γ-rays influence the spectrum of events in the BC-412 scintillator. The spectrum for all flight levels has been fitted with a power law in the areas from 4 MeV to 15 MeV and between 15 MeV and 50 MeV. The index of the spectrum changes at about 15 MeV from -3.3 to -2.3 (see fit parameters in

the lower panel of Fig. 7.4).
In Fig. 7.5 the spectra for events in BC-412 are shown again and the spectrum for all flight levels is divided into four different regions. Below 15 MeV the spectrum is influenced by γ-rays which are incorrectly identified as neutrons. In the region between 15 MeV and 50 MeV the contribution of γ-rays is negligible and thus it is assumed that in this region the spectrum contains only neutrons. Above 50 MeV the index of the spectrum changes again but in this case it is not an effect of different particle species but rather an effect of the detector response which decreases considerably in this region (see Fig. 5.12 for the detector response to neutrons and γ-rays). Figure 7.5 clearly shows that there are also a few events above 100 MeV. As discussed in Chapter 5 the neutron calibration function given in equation (5.4) is not valid for events with energies higher than 100 MeV (see Section 5.1 for details). Thus, these events are not taken into account for the calculation of the dose in BC-412.

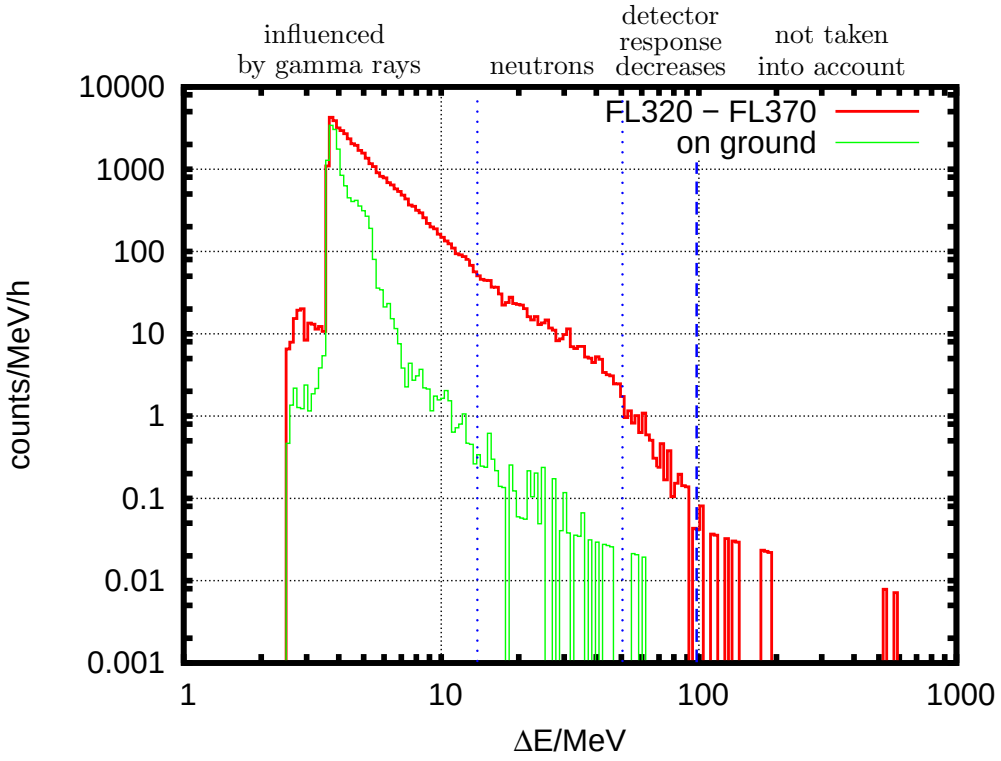

Figure 7.5: *Description of the four different regions in the spectrum of events in BC-412 for the flight levels FL320 to FL370*

After the separation of the events in the BC-412 from the events in CsI(Na), dose rates can be calculated. In Fig. 7.6 the calculation chains for dose rates of events in BC-412 and events in CsI(Na) are displayed. For each species the events are first converted into energy and into dose before the separate dose rates are derived. For the events in BC-412 the neutron calibration function (equation (5.4)) is used and for the energy conversion of the events in CsI(Na) equation (5.7) is applied. For the calculation of the absorbed

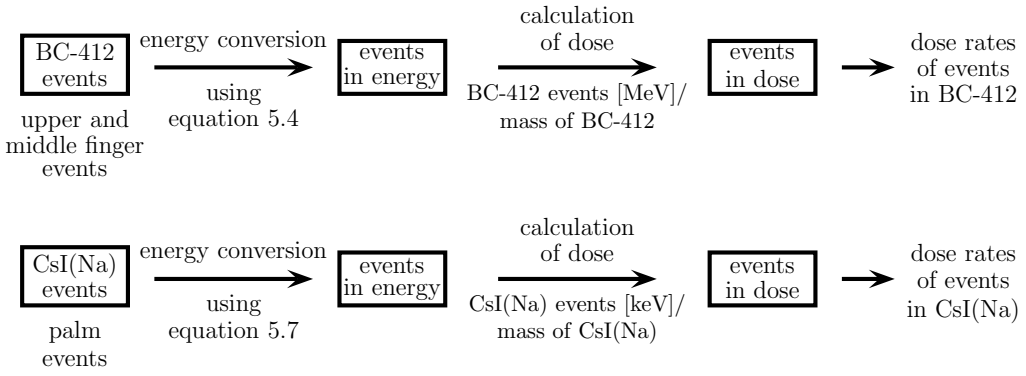

Figure 7.6: *The calculation chains for dose rates of events in BC-412 and events in CsI(Na)*

dose the simplified assumption that the events in BC-412 only interact with the plastic scintillator and that the events in CsI(Na) only interact with the CsI(Na) is made. Thus, when calculating the absorbed dose for the BC-412 events only the mass of the BC-412 scintillator (51.6 g) is taken into account. For the calculation of the absorbed dose of the events in CsI(Na) only the CsI(Na) with a mass of 230.56924 g is considered.

In Fig. 7.7 the separate dose rates for the events in CsI(Na) and events in BC-412 are shown. The dose rates in μGy/h are plotted versus the time in minutes. The same characteristic features as described for the count rate profile in Fig. 7.2 can be observed in the dose rate profile of the events in CsI(Na). The dose rates for events in CsI(Na) range from 0.81 to 1.70 μGy/h at flight altitudes whereas the ones for BC-412 events are only about 0.07 to 0.30 μGy/h. To verify if the measured dose rates are in the right order of magnitude the values are compared with other dose rate measurements on board aircraft. Measurements with the DOsimetry TELescope DOSTEL (developed at the University of Kiel) have been performed on board aircraft before (see e.g. Beaujean et al., 1999). This silicon based instrument is most sensitive to charged particles but also to γ-rays. As mentioned in Chapter 4 the events in CsI(Na) contain not only γ-rays but also charged particles, thus the dose rates in CsI(Na) can be compared to the DOSTEL measurements.

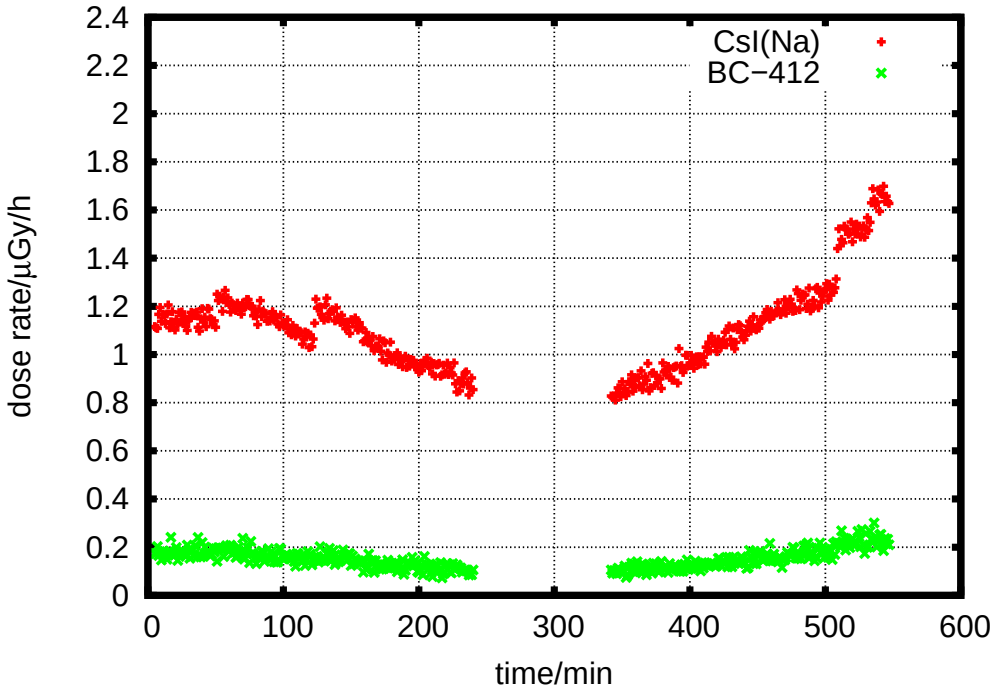

Figure 7.7: *Dose rates for events in CsI(Na) and BC-412*

Beaujean et al. (1999) measured dose rates for a flight from Frankfurt to Mauritius and back. The dose rates in silicon range from about 0.5 to about 2 μGy/h for different flight levels between FL310 and FL390. To be able to compare the results of the two different instruments the absorbed dose has to be converted into dose in water. The conversion factor between silicon and water, which accounts for the different stopping powers of electrons in the two materials, is 1.2 (according to Beaujean et al., 2005). To find a conversion factor for dose in CsI to dose in water is not simple. In the CsI(Na) scintillator mainly primary electrons, electrons as secondary particles from the γ-ray interactions and protons are measured. An upper limit for the conversion factor can be calculated with the stopping power of 2 GeV protons. With a stopping power of 2.021 MeV·cm^2/g in water and 1.238 MeV·cm^2/g in CsI the resulting conversion factor is about 1.63. The stopping powers for protons can be found on the web page of the National Institute of Standards and Technology (see Berger et al., 2005c). Multiplying the DOSTEL dose rates with 1.2 the resulting dose rates in water are 0.6 to 2.4 μGy/h. For the Phoswich detector the measured dose rates in CsI(Na) multiplied by 1.63 result in dose rates in water from 1.32 to 2.77 μGy/h. Thus, the measured

dose rates in CsI(Na) are comparable with the DOSTEL dose rates.
To verify if the measured dose rates of events in the plastic scintillator are in a reasonable range they are compared to the dose rates measured by the neutron dosimeter NEUDOS which was developed in the dissertation of S. Burmeister (Burmeister, 2006). In Burmeister (2006) neutron dose rates on the flight from Hamburg to Fuerte Ventura and back are shown. At flight levels between FL270 and FL360 the measured neutron dose rates range from 0.4 to over 1 μSv/h. With a quality factor of 7.03 (see Burmeister, 2006) these are converted into absorbed doses of 0.06 to 0.142 μGy/h. As mentioned earlier in this section the dose rates of events in the BC-412 measured by the Phoswich detector range from 0.07 to 0.30 μGy/h and thus are in the same order of magnitude as the neutron dose rates measured by NEUDOS. However, this is only a rough estimation because the energy ranges of the two instruments are not exactly the same.
As explained in Chapter 4 not all of the measured raw data are taken into account for the data analysis. In case of the dose rates of events in CsI(Na) only the palm events are considered whereas for the dose rates of events in BC-412 only the events of the upper and the middle finger are taken into account. Thus, the sum of the dose rates from events in CsI(Na) and events in BC-412 shown in this chapter are not the total absorbed dose. However, for the data from the flights Hamburg-Canary Islands and back the correction of the raw data reduces the amount of data by about 6 % and the events in the lower finger are only 1 % of the total data. In total about 7 % of the raw data are not taken into account for the dose rate measurements. Since the events in the lower finger cannot be classified into palm or finger events up to now, it is not possible to convert these events into energy and estimate how much they would contribute to the total dose.

Chapter 8

Stratospheric Balloon Flights

This chapter describes two stratospheric balloon flights which were performed with the developed Phoswich detector. The detector was flown on board a stratospheric weather balloon in cooperation with the Deutscher Wetterdienst (German Meteorological Service, DWD) and on board a BEXUS balloon in cooperation with the German Aerospace Center (Deutsches Zentrum für Luft- und Raumfahrt, DLR) and the Swedish National Space Board (SNSB).

8.1 Balloon Flight on Board a Weather Balloon

In August 2011 a stratospheric balloon flight was performed in cooperation with the Deutscher Wetterdienst (German meteorological service, DWD) in Lindenberg, Germany. The Phoswich detector was placed in a polystyrene box with 5 cm thick walls and then attached to the weather balloon. The weather balloon was filled with helium gas and rose with an ascent rate of about 5 to 6 m/s. Because of the diminishing ambient pressure the balloon expanded while rising until it burst. Fig. 8.1 shows the start of the balloon. Just below the balloon itself the orange parachute is located which is needed to limit the descent speed once the weather balloon has burst. Below the parachute the polystyrene box with the Phoswich detector is located. The duration of the balloon flight was approximately 150 minutes and according to the GPS sensor (provided by the DWD) on board the balloon, a maximum altitude of 29.6 km was reached after about 126 minutes. The balloon was launched in Lindenberg (south of Berlin) and landed at 52.469460° N/15.363970° E in Poland. The GPS data for this balloon flight were provided by the DWD (Naebert, 2011). During the flight the temperature was recorded at two different locations inside the instrument. The

Figure 8.1: *Start of the balloon flight*

temperature sensor which belongs to the pressure sensor integrated in the instrument measured temperatures between 33.4°C and 20.7°C during the balloon flight. The other temperature sensor is located on the preamplifier board. This sensor recorded temperatures between 29.2°C and 18.8°C. Thus, the insulation with 5 cm of polystyrene was enough to keep the instrument warm for the duration of the balloon flight.
The processed data for the balloon flight look similar to the flight data from the measurements on board aircraft shown in Fig. 7.1. The balloon flight data show the same additional branch and as in the aircraft flight data it is treated as belonging to the events in CsI(Na).

In Fig. 8.2 the count rate and pressure profile for the balloon flight is shown. Displayed here are the count rates from all events in the instrument (meaning from both scintillators). The pressure shown here is the pressure recorded by the pressure sensor of the Phoswich instrument which could be used as a measure for the altitude of the balloon. About 100 minutes after the start of the measurement a noise peak was visible in the processed data.

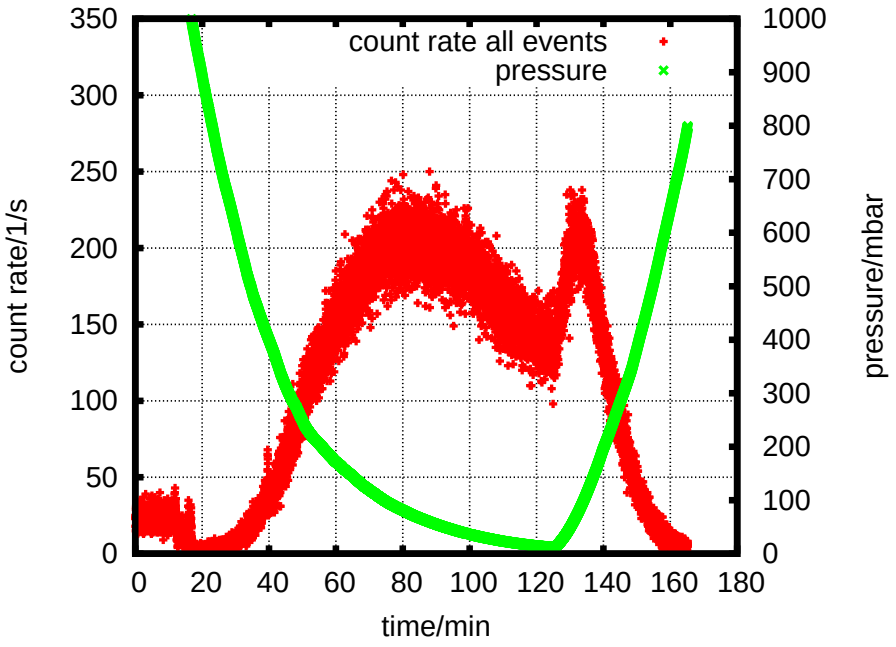

Figure 8.2: *Time profile of the balloon flight: The count rates of all events and the pressure measured by the pressure sensor of the Phoswich detector are plotted versus time in minutes*

This noise peak is excluded in the further data analysis. The uncorrected data are shown in Fig. *F*.1 in Appendix *F*. Figure 8.2 clearly shows that the instrument recorded two maxima in the count rates during the flight. These are the two passages through the Pfotzer maximum, one during the ascend and one during the descend phase. Since the passage through the maximum during the ascent phase of the balloon lasts longer (speed during ascent phase about 5 to 6 m/s) than during the descend phase (speed during descend phase about 21 m/s) the first maximum is broader than the second one.

8.1.1 Determination of the Pfotzer Maximum

The location of the Pfotzer maximum can be determined by correlating the measured count rates with either the altitude in kilometers measured by the GPS sensor or with the pressure measured by the pressure sensor integrated in the Phoswich detector. The correlation with the pressure is the more interesting case because the pressure is a direct measure for the residual atmo-

sphere which describes the shielding by the atmosphere above the detector. Since the pressure sensor was lagging behind during the test measurements shown in Chapter 6, the pressure measurement might not be entirely reliable. Thus, the first attempt to determine the Pfotzer maximum is to use the altitude measured by the GPS sensor.

In Fig. 8.3 the count rate profile is shown in correlation with the altitude in

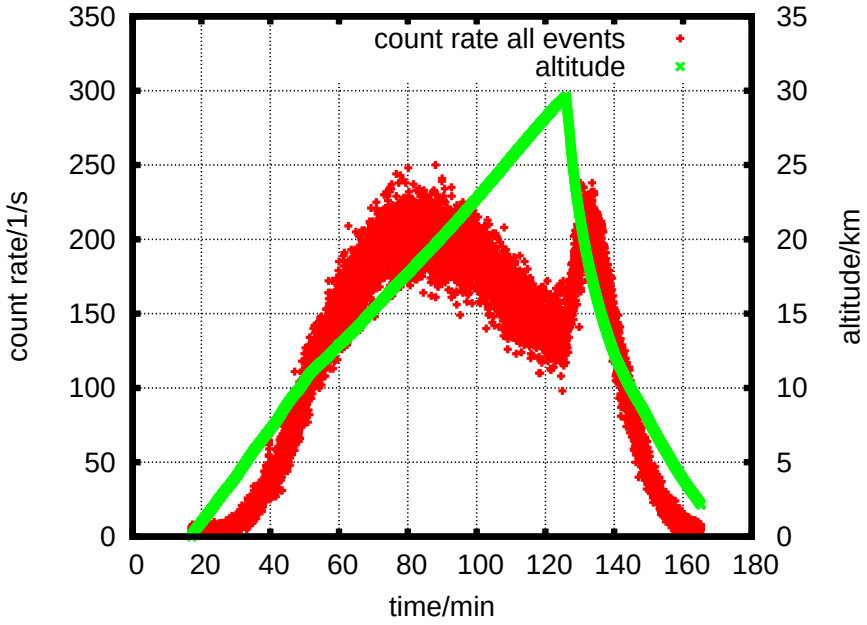

Figure 8.3: *Time profile of the balloon flight: Count rates of all events and altitude in kilometers versus time in minutes*

kilometers. The correlation between the two independent measurements with the Phoswich detector and with the GPS sensor can be done with an accuracy of 30 seconds when synchronising the starting times of both measurements. In Fig. 8.4 the count rates are plotted versus the altitude in kilometers. In this plot the count rates from the whole balloon flight are used which means that both crossings through the Pfotzer maximum are considered. The lower panel of Fig. 8.4 shows the same data as the upper panel of Fig. 8.4 but in the range from 30 km to 12.415 km. A cubic function was found to be sufficient to describe the data in this altitude range. The following fit function was found $f(x)=0.072 \cdot x^3-5.3 \cdot x^2+123 \cdot x-706$. Calculation the maximum of this fit function yields an altitude of 18.47 km at the maximum of the count rates.

In the upper and lower panel of Fig. 8.5 the same determination of the

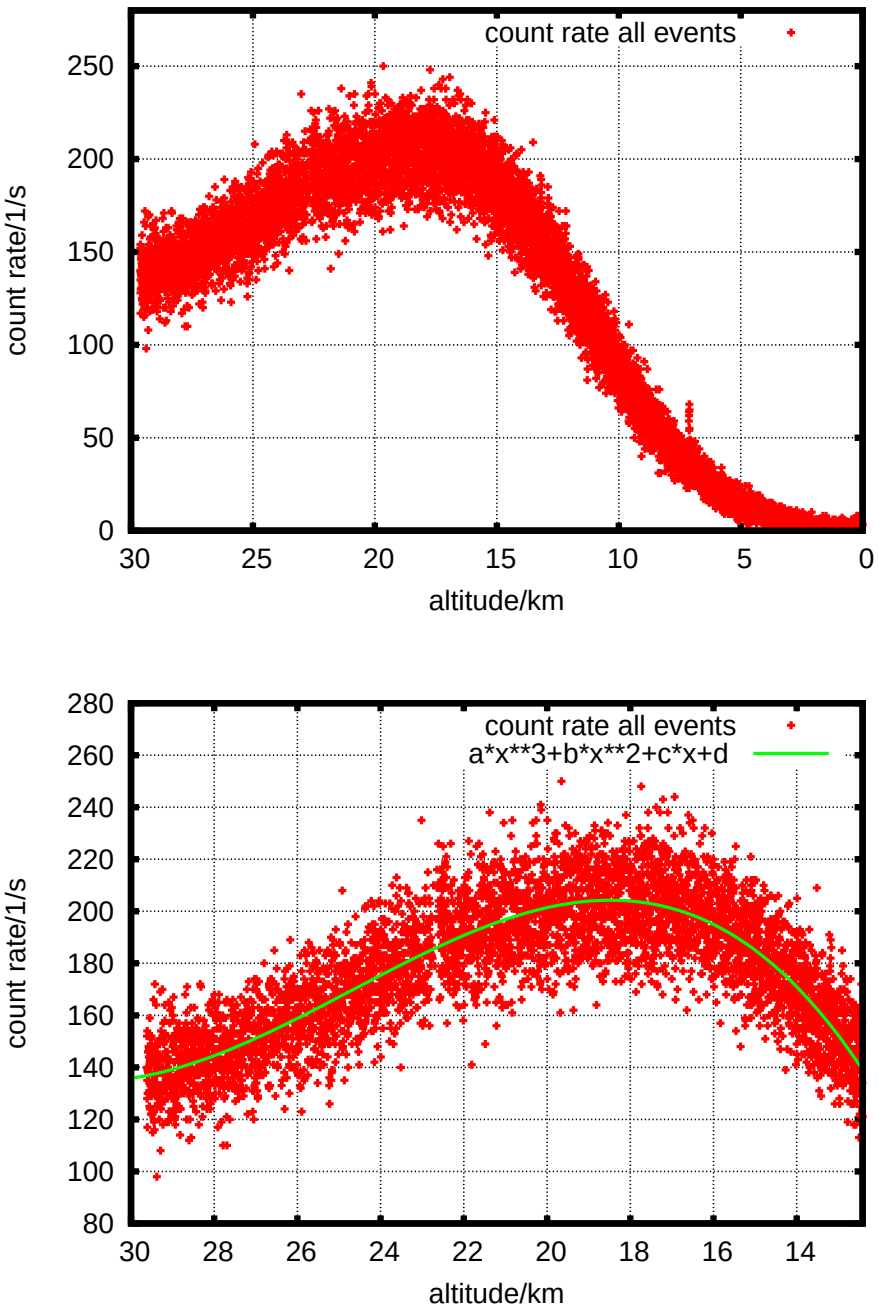

Figure 8.4: *Upper panel: Count rates per seconds versus altitude in kilometers measured by the GPS sensor. Lower panel: The same data as in the upper panel but in the range between 30 km and 12.415 km with a cubic fit*

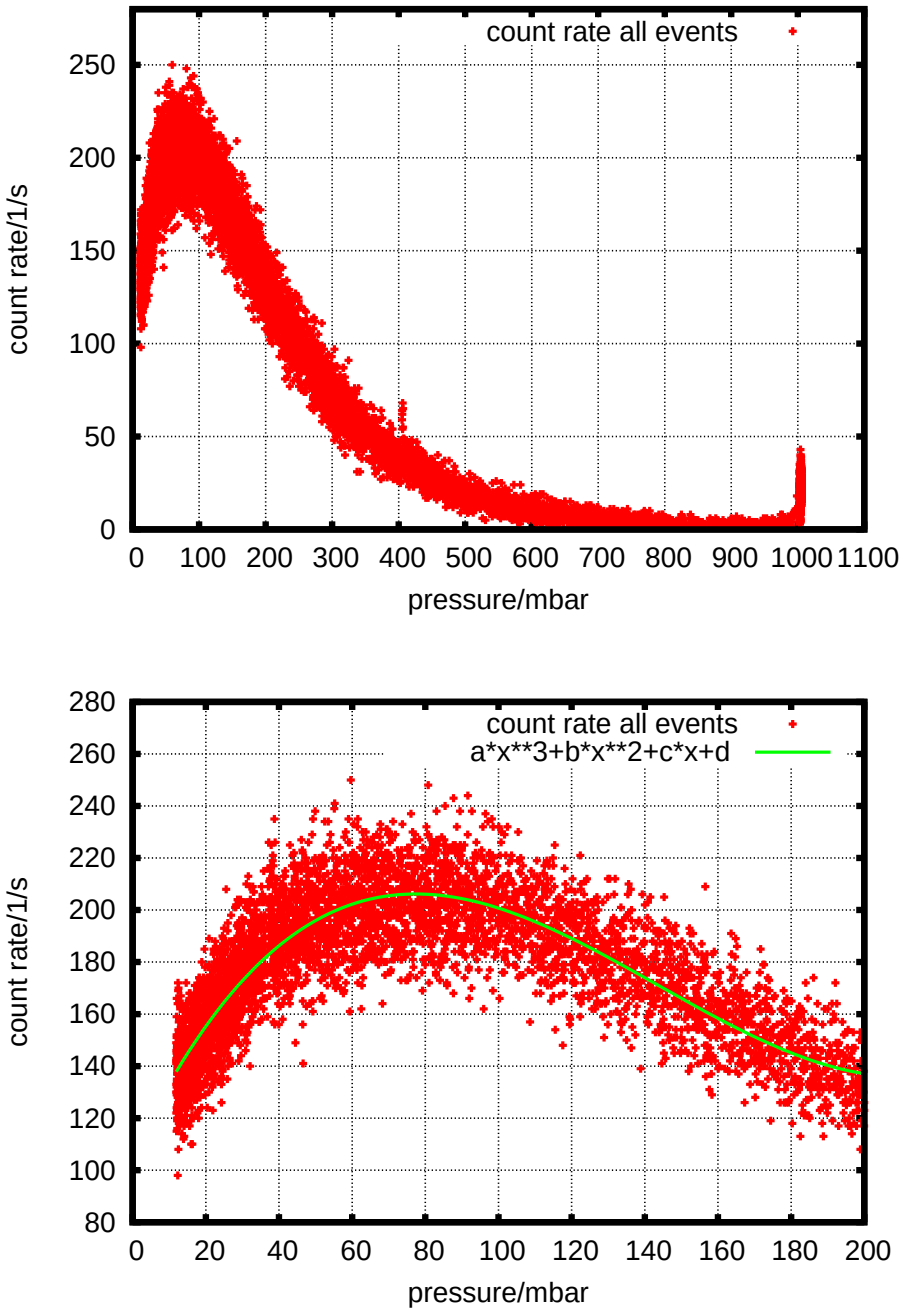

Figure 8.5: *Upper panel: Count rates of all events per seconds versus pressure in millibar measured by the pressure sensor of the Phoswich detector. Lower panel: The same data as in the upper panel but in the range between 0 mbar and 200 mbar with a cubic fit*

Pfotzer maximum is done for the correlation of the count rates with the pressure in millibar measured by the pressure sensor of the instrument. In this case also the count rates from the whole balloon flight are used meaning that both crossings through the Pfotzer maximum are considered. In the lower panel of Fig. 8.5 the data are fitted with a cubic function in the range from 0 mbar to 200 mbar resulting in the fit function $f(x)=6.0\cdot10^{-5}\cdot x^3-0.0260\cdot x^2+2.94\cdot x+106.4$. The maximum of the count rates is found at a pressure of 77.41 mbar.
To convert the measured pressure into an altitude in kilometers, data from a meteorological sensor from the DWD can be used. This sensor was launched with a second weather balloon eight minutes after the balloon with the Phoswich detector. These data were provided by the DWD (Naebert, 2011). Figure 8.6 shows the correlation of pressure in millibar and altitude in kilometers derived from these data.

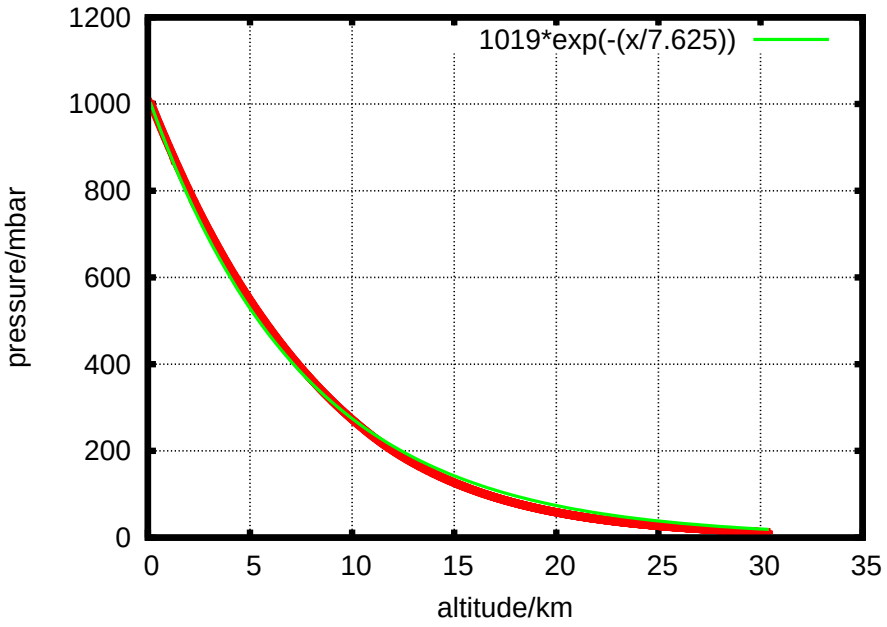

Figure 8.6: *Pressure in millibar versus the altitude in kilometers; data are taken from a meteorological sensor on board a second weather balloon (Naebert, 2011)*

The data are fitted with a barometric formula. The value for the atmospheric pressure at sea level is set to 1019 hPa for the day of the balloon flight (value provided by DWD (Naebert, 2013)). This results in the following relation to convert measured pressure into altitude:

$$h = -7.625 \cdot \ln\left(\frac{p(h)}{1019}\right) \tag{8.1}$$

with the altitude h in kilometers and the pressure p in millibar.
Applying equation (8.1) the pressure at the location of the maximum of the count rates, 77.41 mbar, equals an altitude of 19.65 km. Using the altitude measured by the GPS sensor the maximum of count rates was found at 18.47 km. Thus, the difference between the altitude of the Pfotzer maximum determined by the correlation with the altitude and the correlation with the pressure is 1.18 km which is about 6.4 %. Therefore, the pressure measured by the pressure sensor of the instrument can be used as an approximation for the altitude of the balloon.
Both the derived values for the altitude of the Pfotzer maximum agree quite well with the value in the literature where the location of the Pfotzer maximum is given with about 20 km (see e.g. Grieder, 2001b).

8.1.2 Count Rates for Events in CsI(Na) and BC-412

The upper panel of Fig. 8.7 displays the separate count rates for events in CsI(Na) and BC-412. The count rates for both materials show a similar profile as the count rates of all events in Fig. 8.2 but note that the count rate in BC-412 is much smaller (right axis in the upper panel of Fig. 8.7) than the count rate in CsI(Na) (left axis in in the upper panel of Fig. 8.7). The noise peak in the data which was mentioned above was also visible in the separate count rates. It is not taken into account for the further data analysis. The uncorrected count rates are shown in Fig. $F.2$ in Appendix F.
Analogous to the determination of the maximum of count rates of all events done in the previous section, the maxima of the separate count rates can also be determined. In the lower panel of Fig. 8.7 the count rates for events in CsI(Na) and BC-412 are shown versus the pressure measured by the instrument. The separate count rates are each fitted with a cubic function as it has been done for the count rates of all events in the lower panel of Fig. 8.5. Note that the separate count rates for events in CsI(Na) and BC-412 are shown per minute whereas the count rates for all events were shown per second.

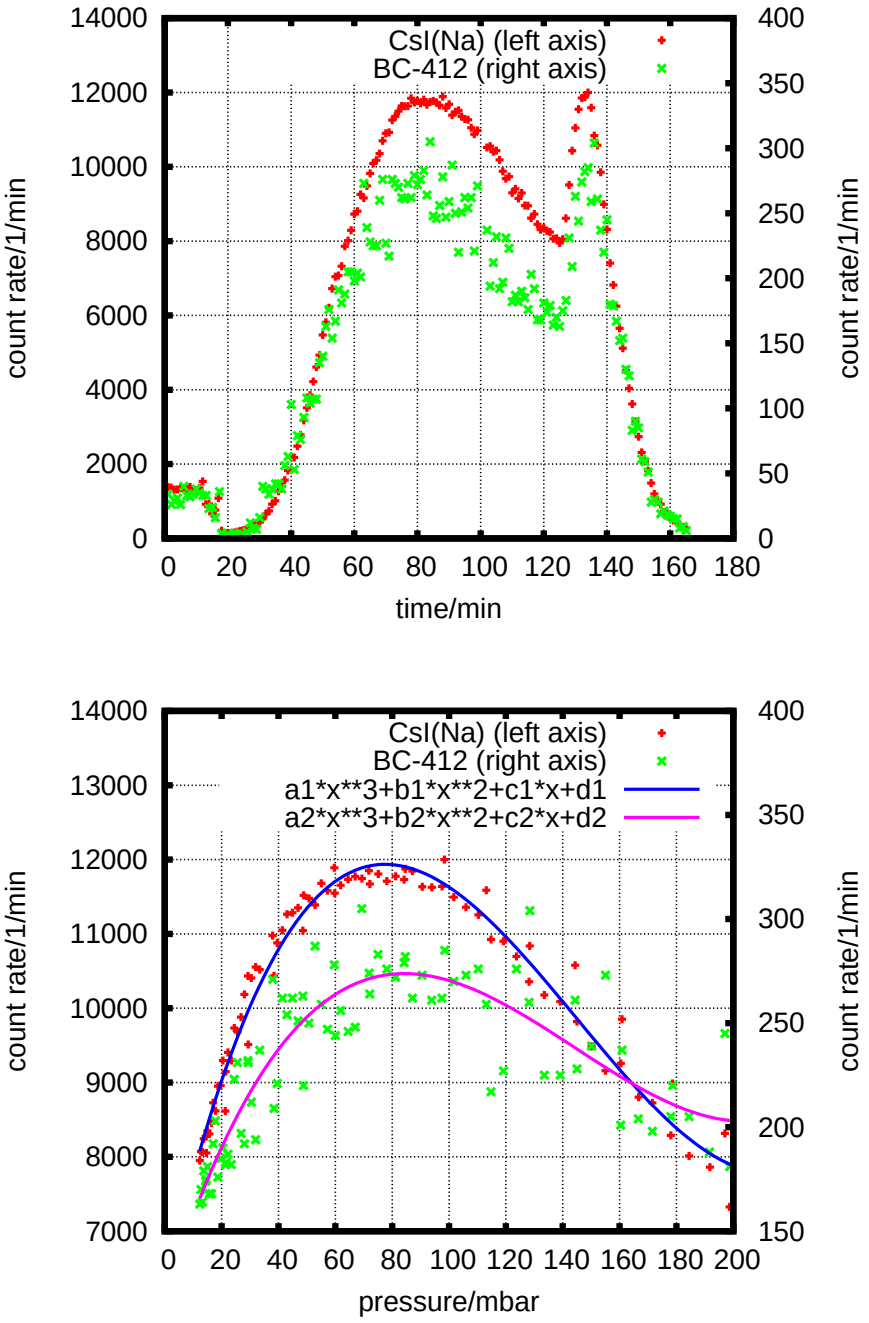

Figure 8.7: *Upper panel: Count rate profiles for events in CsI(Na) (left axis) and events BC-412 (right axis). Lower panel: Separate count rates for events in CsI(Na) (left axis) and events BC-412 (right axis) each with a cubic fit*

The following fit function was found for count rates of events in CsI(Na): $f(x)=0.0034 \cdot x^3-1.47 \cdot x^2+167 \cdot x+6238$. For the count rates of events in BC-412 the fit function is the following: $f(x)=8 \cdot 10^{-5} \cdot x^3-0.036 \cdot x^2+4.3 \cdot x+118$. The maximum of the count rates in CsI(Na) is found at 77.55 mbar (19.64 km) and the one of the count rates in BC-412 at 84.32 mbar (19.00 km).
The value for the events in CsI(Na) is very similar to the one for all count rates which shows that the measurement is dominated by events in CsI(Na). The maximum of count rates for events in BC-412 is at a lower altitude. The locations of the different maxima will be discussed in Section 8.3.

8.1.3 Dose Rates for Events in CsI(Na) and in BC-412

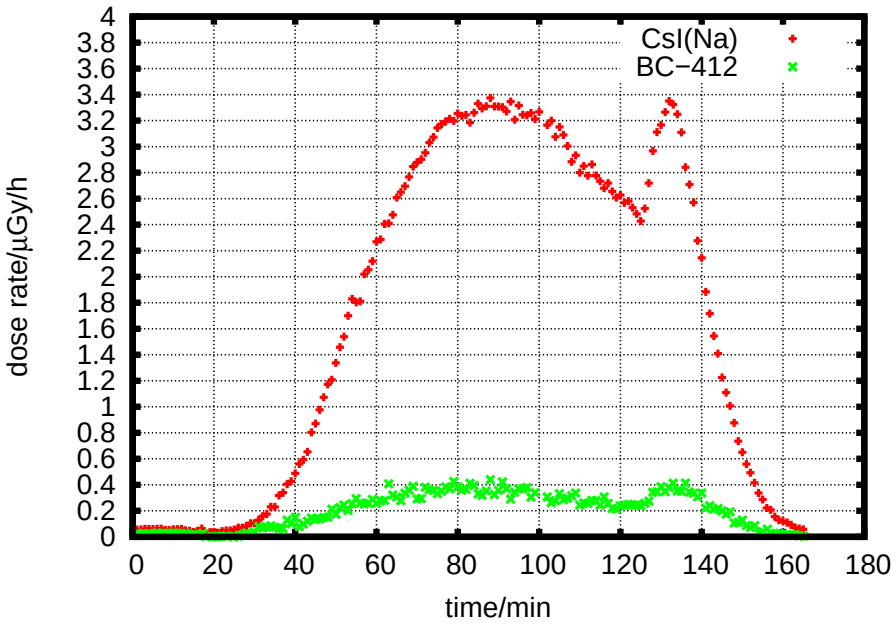

Figure 8.8: *Dose rate profiles for events in CsI(Na) and events in BC-412: the dose rates in µGy/h are shown versus the time in minutes*

The dose rates for events in CsI(Na) and BC-412 have been calculated as explained in Chapter 7, thus the dose rates for BC-412 include all events up to an energy of 100 MeV. In Fig. 8.8 the separate dose rates profiles for events in CsI(Na) and BC-412 are displayed. The noise peak in the data which was mentioned above causes an elevated dose rate at the same time when the noise peak occurred. The uncorrected data for the dose rates are shown

in Fig. *F*.3 in Appendix *F* and for the further data analysis these values of increased dose rate are not taken into account.
When comparing the dose rates during the balloon flight with the ones measured on board the airplane, the dose rates during the balloon flight are higher. This is as expected because the balloon rises to much higher altitudes which implies a higher particle flux (up to the Pfotzer maximum).
As already observed in the count rate profiles, the dose rate profiles show two maxima during the balloon flight. Such a maximum of the dose rates is mentioned in Bartlett (2004) where the author states that there is a maximum for the dose rates in the Earth's atmosphere and that it is located at about 20 km or about 50 g/cm^2. In the following the location of these maxima is calculated.

To determine the location of the maxima of the separate dose rates, the

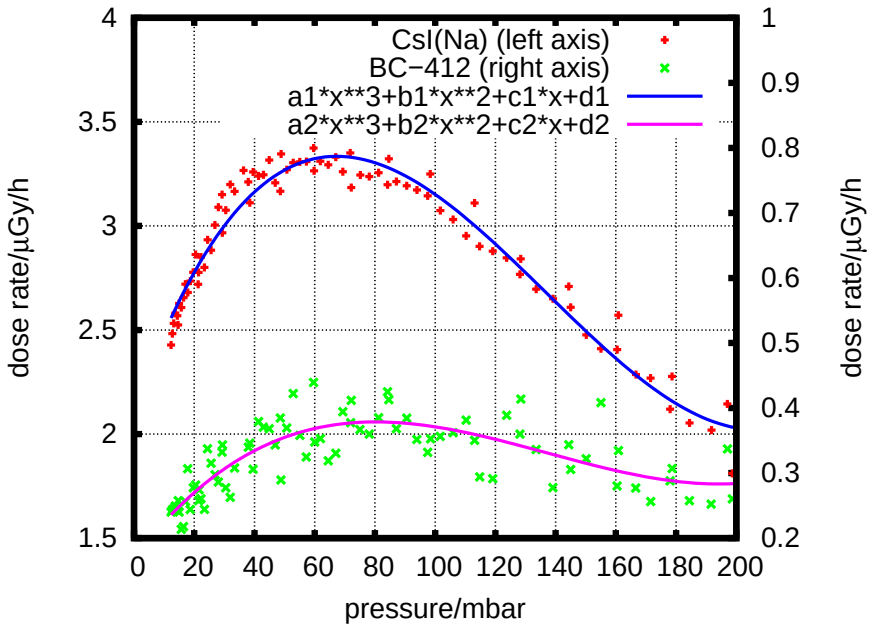

Figure 8.9: *Separate dose rates for events in CsI(Na) and events BC-412 versus the pressure of the instrument in millibar. Each curve is fitted with a cubic function*

dose rates in CsI(Na) and BC-412 are displayed versus the pressure measured by the instrument in Fig. 8.9. Again each curve is fitted with a cubic function. The fit function for the dose rates in CsI(Na) is: f(x)=$9.7\cdot10^{-7}\cdot x^3$-$0.00040\cdot x^2$+$0.041\cdot$x+2.12 and for the dose rates in BC-412: f(x)= $1.3\cdot10^{-7}\cdot x^3$-$5.3\cdot10^{-5}\cdot x^2$+$0.0060\cdot$x+0.17. The maximum of the dose rates in CsI(Na) is

located at 67.32 mbar (20.72 km) and the one for the dose rates in BC-412 at 80.29 mbar (19.37 km). As for the separate count rates the maximum for the events in CsI(Na) is at higher altitudes than the maximum for the events in BC-412.
The locations of the maxima for count rates and dose rates will be discussed in Section 8.3.

8.2 Balloon Flight on Board a BEXUS Balloon

In September 2012 the Phoswich detector was flown on board a BEXUS balloon. BEXUS stands for **B**alloon-borne **Ex**periments for **U**niversity **S**tudents and is a cooperation between the German Aerospace Center (Deutsches Zentrum für Luft- und Raumfahrt, DLR) and the Swedish National Space Board (SNSB) (see web site REXUS/BEXUS, 20.11.2012). The project to participate in the BEXUS programme was realized with a group of students from the University of Kiel (see web site MONSTA, 25.11.2012). The balloon was launched near Kiruna, Sweden, and the flight lasted about four hours and 40 minutes including a floating phase of almost two and a half hours. According to the GPS sensor on board the balloon a maximum altitude of 28.7 km was reached.
In Fig. 8.10 the count rate profile for this balloon flight is shown. Displayed are the count rates of all events from the processed data and the pressure measured by the pressure sensor of the instrument. The count rates in Fig. 8.10 are higher than the ones recorded during the flight with the weather balloon (see Fig. 8.2), which is due to the fact that the balloon flight with the weather balloon took place at lower latitudes where the cutoff rigidity is higher which means that particles need a higher energy to penetrate the Earth's magnetic field and thus less particles are able to enter the Earth's atmosphere.
Note that there was a noise peak during the rising phase which is not taken into account for the further data analysis. The uncorrected data with the noise peak are shown in Fig. *F*.4 in Appendix *F*.

8.2.1 Determination of the Pfotzer Maximum

The determination of the Pfotzer maximum for this balloon flight is done as explained for the other balloon flight in Section 8.1.1. In case of the other balloon flight it was found that there was a difference between the Pfotzer maximum determined with the pressure of the instrument and with the GPS altitude of the balloon. In case of this balloon flight a pressure measurement

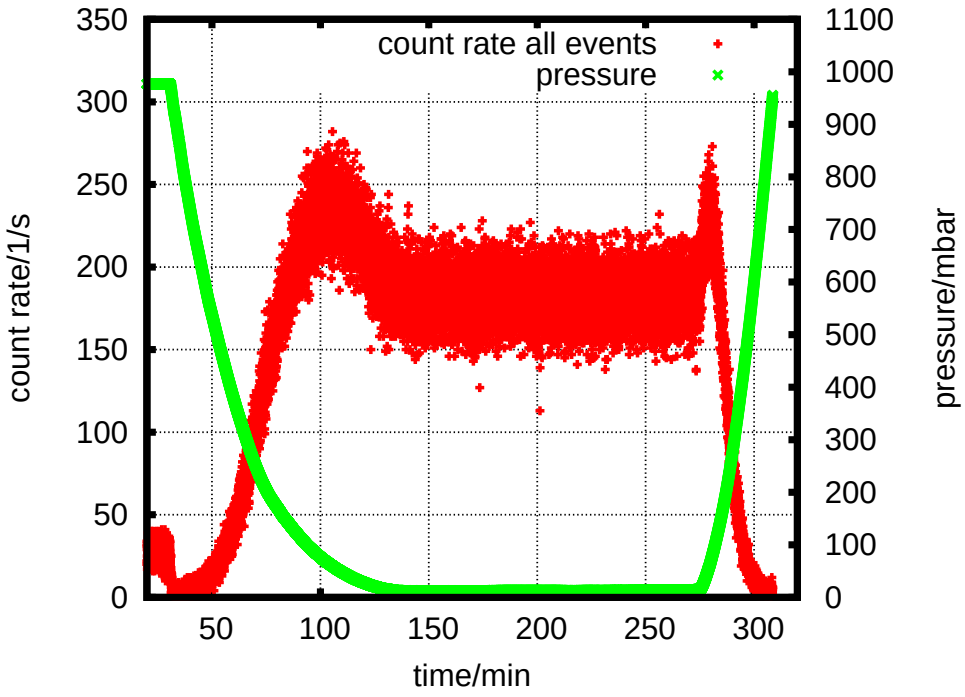

Figure 8.10: *Time profile of the balloon flight: Count rates of all events and pressure measured by the pressure sensor of the instrument is displayed versus the time in minutes*

from a sensor on board the balloon is provided (Inga, 29.10.12).
In Fig. 8.11 the count rates of all events in the instrument are shown together with the pressure measured by the instrument and the pressure measured by the sensor on board the balloon. In the following the latter will be referred to as pressure sensor of the balloon. No difference between the pressure values is visible in this figure. The slide difference between the different pressure values is better visualised in Fig. 8.12 where the count rates are plotted versus each pressure. The maximum of count rates is shifted a little bit towards higher pressures for the pressure values of the sensor of the balloon. In the following the Pfotzer maximum will be determined using both, the pressure measured by the sensor of the balloon and the pressure measured by the sensor of the instrument.
Fig. 8.13 shows the count rate of all events plotted versus the pressure of pressure sensor of the balloon. The lower panel of Fig. 8.13 is a zoom into the upper panel of Fig. 8.13 and the count rates are fitted with a cubic function in the range between 0 mbar and 200 mbar. The following fit function

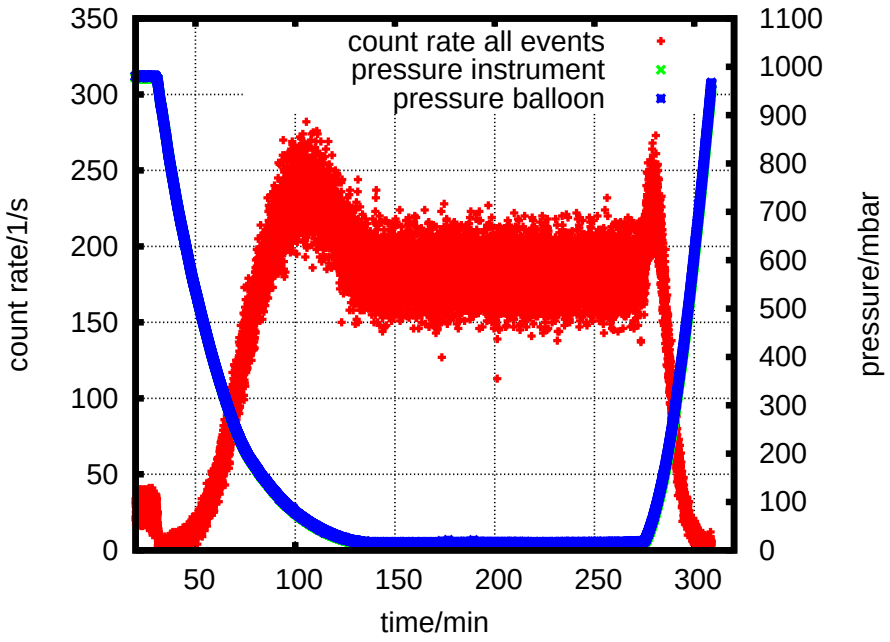

Figure 8.11: *Count rates of all events, pressure of the pressure sensor of the instrument and pressure measured by the pressure sensor of the balloon versus time in minutes*

was found: $f(x)=7.6\cdot10^{-5}\cdot x^3-0.0307\cdot x^2+3.16\cdot x+139.7$ and the resulting location of the maximum is at 69.25 mbar.
In Fig. 8.14 the same procedure is used to determine the maximum of the count rates of all events correlated with the pressure of the pressure sensor of the instrument. The following fit function was found: $f(x)=7.5\cdot10^{-5}\cdot x^3-0.0299\cdot x^2+2.97\cdot x+149.3$ and with these parameters the maximum of the count rates is found at 66.20 mbar. Thus, the difference between the two determined locations of the Pfotzer maximum is 3.05 mbar, which equals 4.4%. As it has been done in the data analysis for the other balloon flight, in the following the pressure measured by the pressure sensor of the instrument will be used.

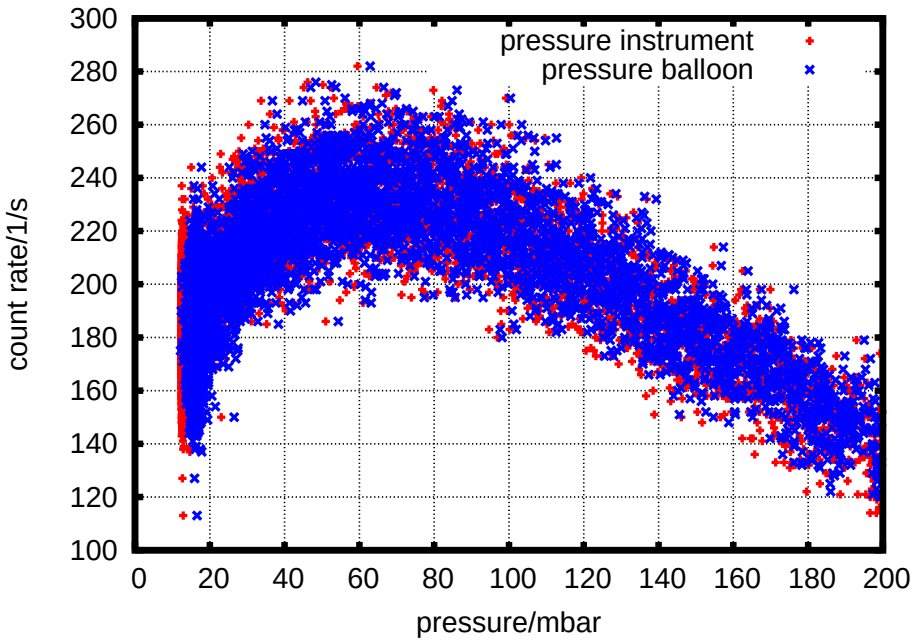

Figure 8.12: *Count rates of all events versus the pressure of the pressure sensor of the instrument (red) and versus the pressure of the pressure sensor of the balloon (blue)*

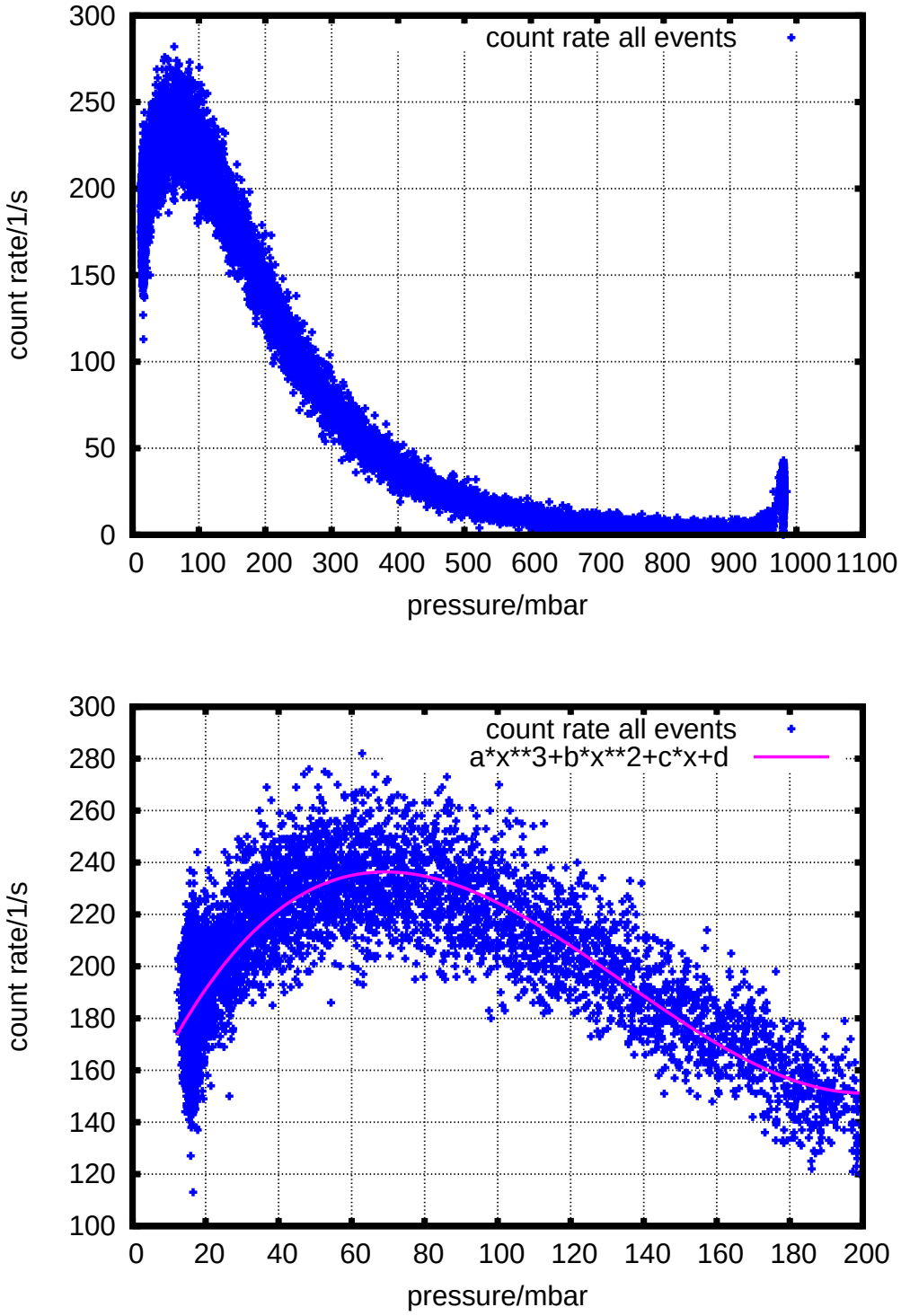

Figure 8.13: *Determination of the Pfotzer maximum by correlating the count rate of all events with the pressure measured by the sensor on board the balloon*

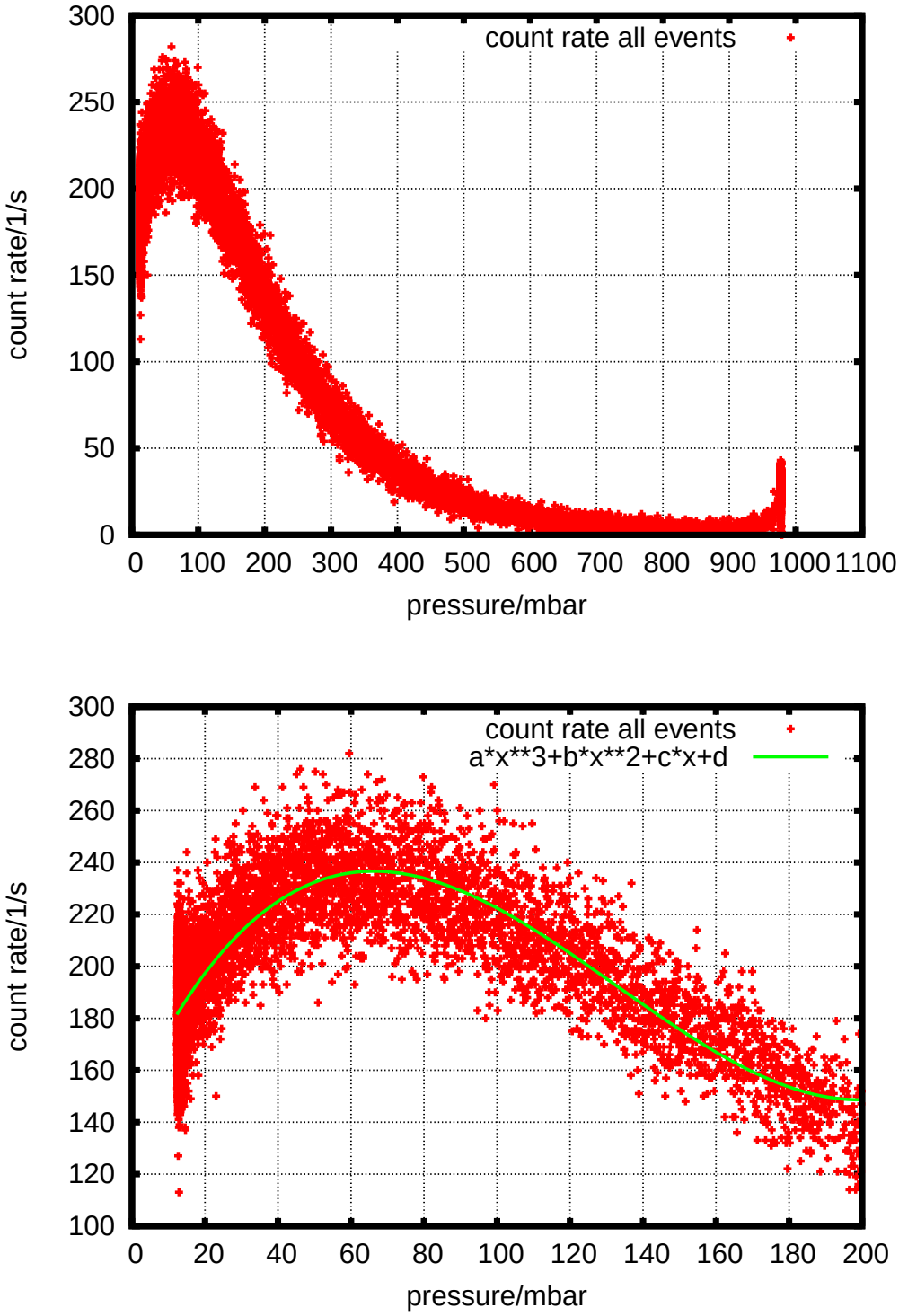

Figure 8.14: *Determination of the Pfotzer maximum by correlating the count rate of all events with the pressure measured by the sensor integrated in the Phoswich detector*

To convert the measured pressure into an altitude, data from the sensors on board the balloon (Inga, 29.10.12) can be used. In Fig. 8.15 the pressure in millibar measured by the sensor on board the balloon is plotted versus the altitude in kilometers. As for the other balloon flight the data are fitted

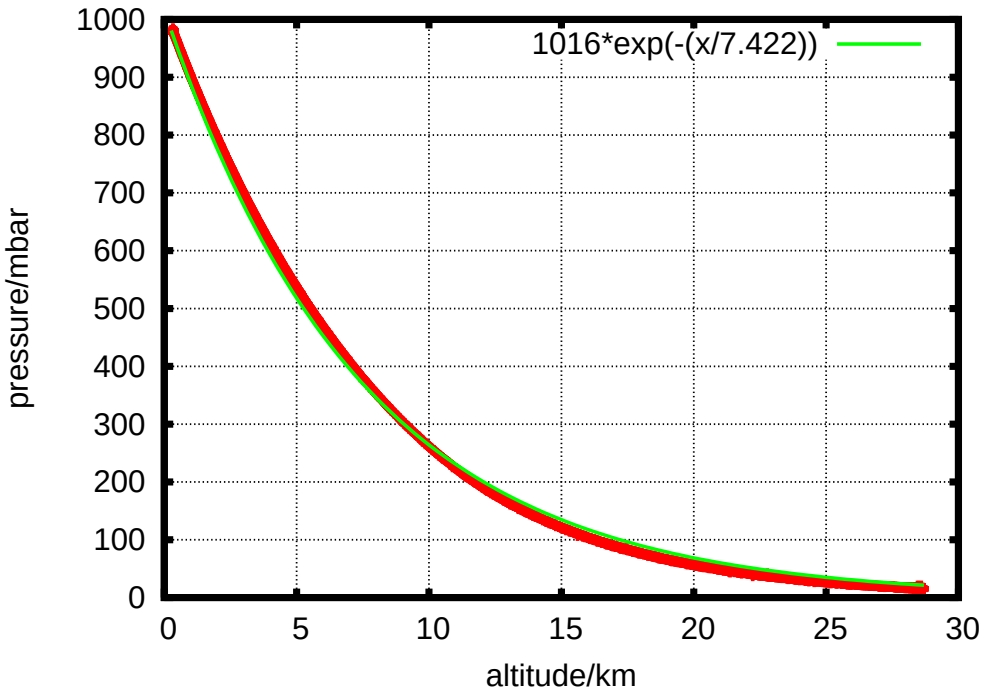

Figure 8.15: *Pressure in millibar versus altitude in kilometers for the balloon flight. The data are taken from sensors on board the balloon (Inga, 29.10.12)*

with a barometric formula and in this case the value for the atmospheric pressure at sea level is set to 1016 hPa (average value for the day of the flight with the BEXUS balloon taken from the web site of wetteronline.de (wetteronline.de, 22.01.2014)). The function to convert measured pressure into altitude is given by:

$$h = -7.422 \cdot ln\left(\frac{p(h)}{1016}\right) \tag{8.2}$$

with the altitude h in kilometers and the pressure p in millibar.
Using the correlation given in equation (8.2) the maximum of the count rates from all events at 66.20 mbar (determination with the pressure of sensor of

the instrument) equals an altitude of 20.27 km. For the determination with the pressure of the sensor of the balloon the maximum at 69.25 mbar equals 19.93 km. The difference of the determined location in kilometers then is 0.34 km, which equals 1.7 %.

8.2.2 Count Rates for Events in CsI(Na) and BC-412

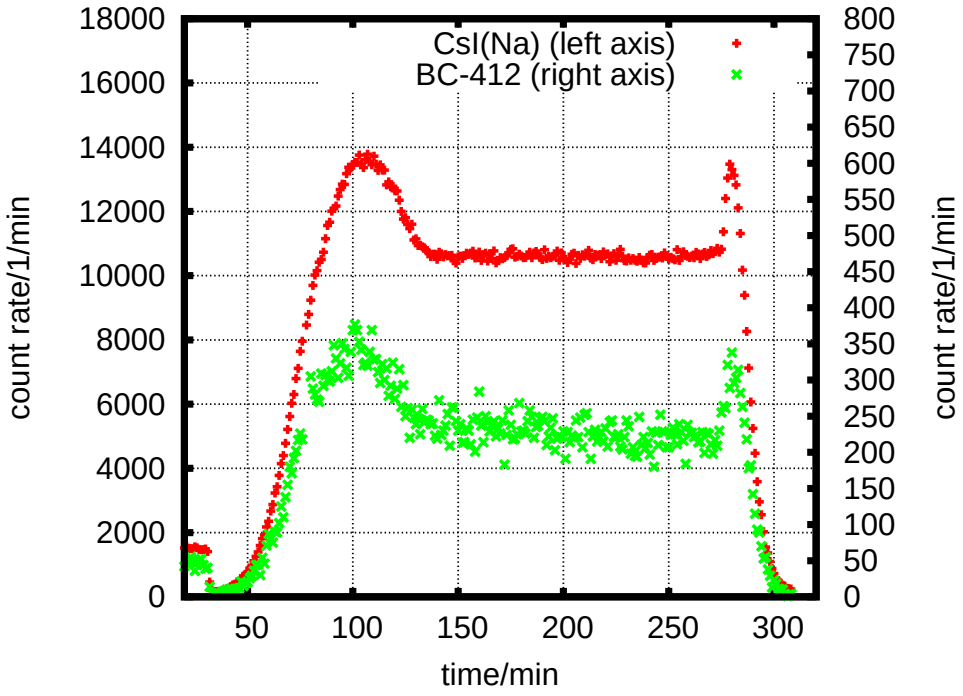

Figure 8.16: *Separate count rates for events in CsI(Na) (left axis) and events in BC-412 (right axis)*

Figure 8.16 shows the separate count rates for events in CsI(Na) and events in BC-412 per minutes versus the time in minutes. As the for the previous balloon flight only events in BC-412 with energies up to 100 MeV are taken into account.
It was mentioned above that there was a noise peak in the data during the rising phase of the balloon flight. This noise is also visible in the count rates of BC-412 and CsI(Na). The uncorrected data are shown in the upper and the lower panel of Fig. *F*.5 in Appendix *F*. Note that the noise during the

rising phase of the balloon flight caused points of increased count rate for both the count rate of events in CsI(Na) and in BC-412. These point are not considered for the further data analysis.
In the following the maxima of the separate count rates are calculated. Figure 8.17 shows the separate count rates for events in CsI(Na) and events in BC-412 versus the pressure from the pressure sensor of the instrument each fitted with a cubic function. The fit function found for the events in

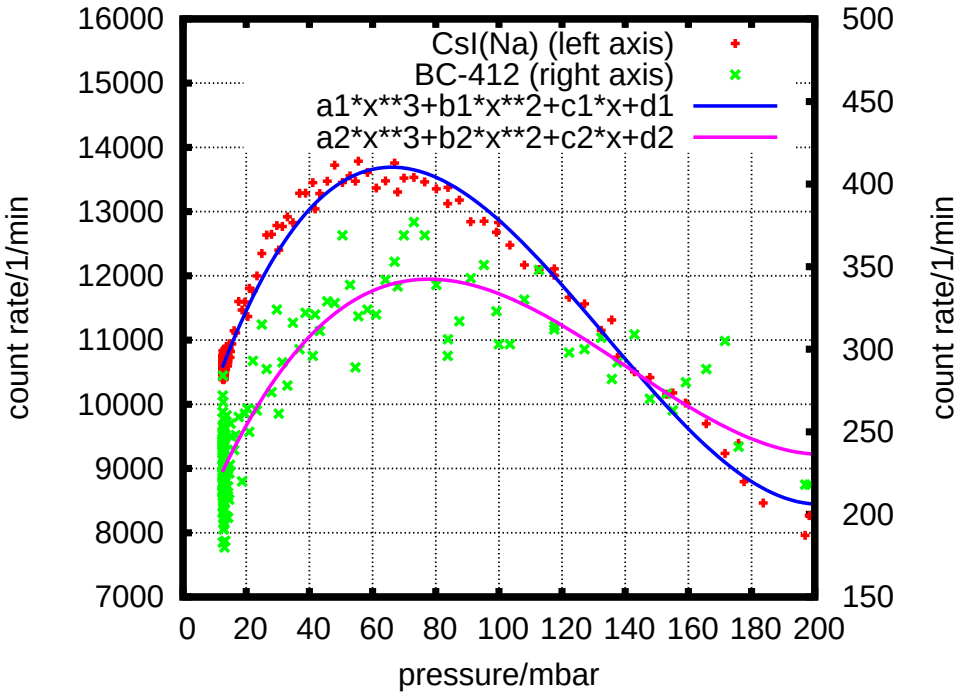

Figure 8.17: *Separate count rates for events in CsI(Na) (left axis) and in BC-412 (right axis)*

CsI(Na) is: $f(x)=0.0042 \cdot x^3-1.70 \cdot x^2+169 \cdot x+8723$ and for events in BC-412 it is: $f(x)=1.1 \cdot 10^{-4} \cdot x^3-0.045 \cdot x^2+5.1 \cdot x+169$. With these fits the maxima of the count rates are at 66.06 mbar for events in CsI(Na) and at 77.82 mbar for events in BC-412. Using equation (8.2) this equals 20.29 km and 19.07 km, respectively.
Comparing these results with the maximum of the count rates of all events, the maximum of the count rates in CsI(Na) is almost at the same altitude whereas the maximum for the count rates of events in BC-412 is at a lower altitude.

8.2.3 Dose Rates for Events in CsI(Na) and BC-412

In Fig. 8.18 the separate dose rates in μGy/h for events in CsI(Na) and events in BC-412 are displayed. The noise in the data that was already mentioned when the count rates were discussed, caused points of elevated dose rate in both the dose rates of events in CsI(Na) and the dose rates of events in BC-412. For the further data analysis these points are not taken into account. The uncorrected data are displayed in the upper and the lower panel of Fig. *F*.6 in Appendix *F*.

As observed for the count rates, the dose rates for this balloon flight are also

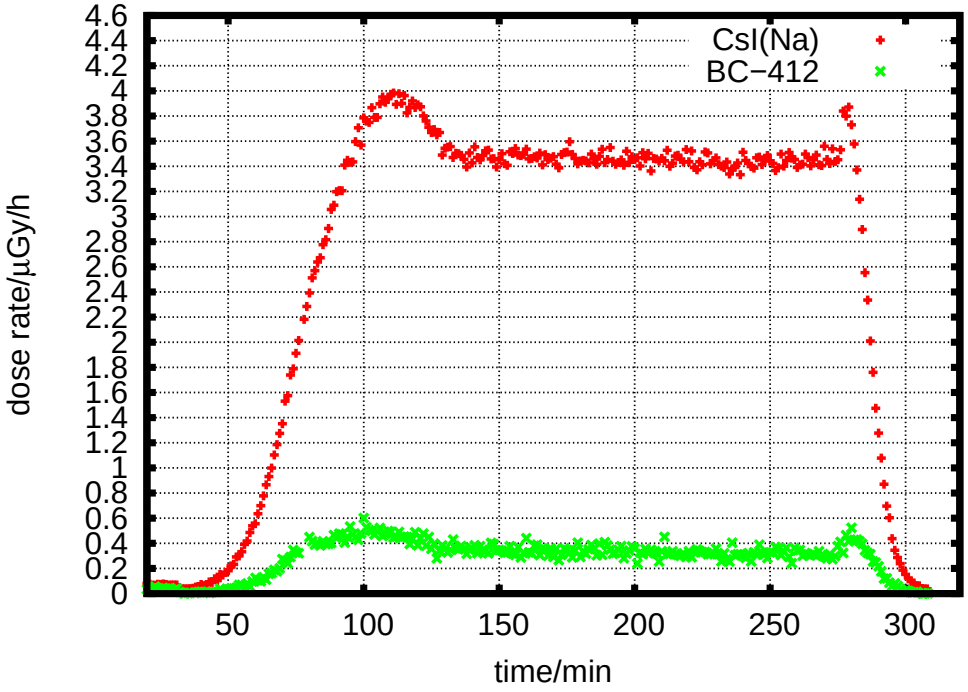

Figure 8.18: *Separate dose rates for events in CsI(Na) and BC-412*

higher than the ones measured on board the weather balloon (see Fig. 8.8). The reason is the same as for the count rates: with increasing latitudes the shielding of the Earth's magnetic field decreases and more particles can penetrate the Earth's atmosphere leading to higher dose rates.

To determine the maxima of the dose rates, Fig. 8.19 displays the dose rates in μGy/h for events in CsI(Na) and events in BC-412 versus the pressure of the pressure sensor of the instrument. The dose rates are fitted with the following cubic functions: $f(x)=1.07\cdot10^{-6}\cdot x^3-0.00041\cdot x^2+0.034\cdot x+3.09$ (for

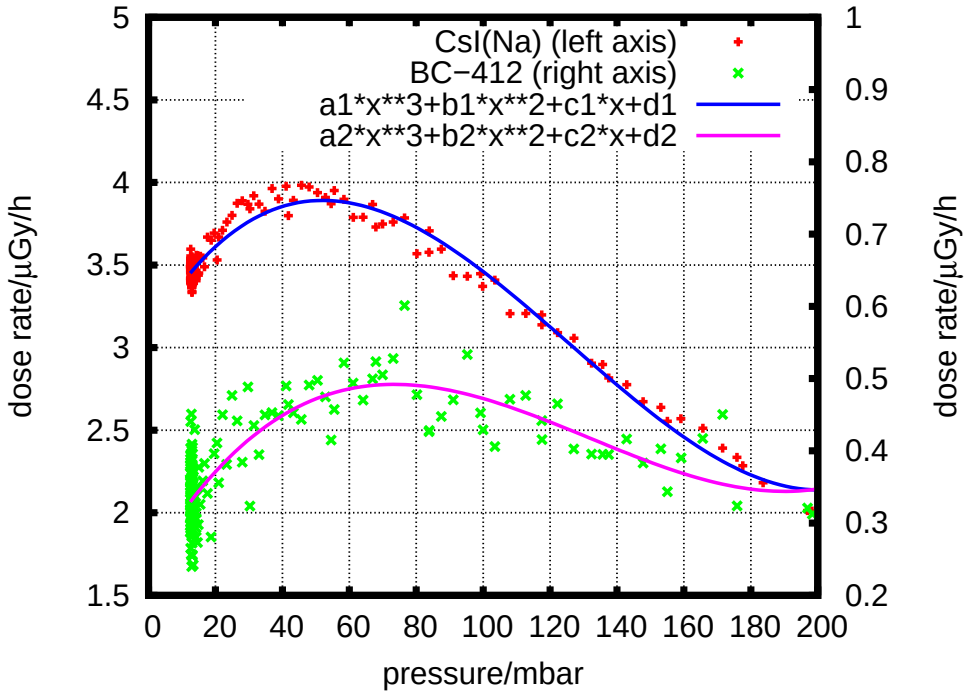

Figure 8.19: *Separate dose rates versus the pressure of the instrument each fitted with a cubic function*

CsI(Na)) and f(x)=$1.9 \cdot 10^{-7} \cdot x^3$-$7.4 \cdot 10^{-5} \cdot x^2$+0.0078·x+0.243 (for BC-412). The resulting maxima are 52.04 mbar (22.06 km) for the dose rates of events in CsI(Na) and 73.33 mbar (19.51 km) for the dose rates of events in BC-412. Thus, it is the same case as observed for the previous balloon flight: the maximum for the dose rates of events in CsI(Na) is at a higher altitude than the one for the dose rates of events in BC-412.

8.3 Locations of the Maxima of Count Rates and Dose Rates

All calculated locations of the maxima for count rates of all events, separate count rates and separate dose rates for both balloon flights are summarized in Table 8.1. Comparing the determined locations of the maxima, it is evident that all maxima for the balloon flight near Kiruna are located at higher altitudes than the ones for the balloon flight near Berlin. This can be explained with the difference in the cutoff rigidities between Kiruna and Berlin.

	Weather Balloon	BEXUS Balloon
count rate all events	77.41 mbar (19.65 km)	66.20 mbar (20.27 km)
count rate in CsI(Na)	77.55 mbar (19.64 km)	66.06 mbar (20.29 km)
count rate in BC-412	84.32 mbar (19.00 km)	77.82 mbar (19.07 km)
dose rates in CsI(Na)	67.32 mbar (20.72 km)	52.04 mbar (22.06 km)
dose rates in BC-412	80.29 mbar (19.37 km)	73.33 mbar (19.51 km)

Table 8.1: *Locations of the maxima of count rates and dose rates for both balloon flights (note that the calculated altitudes in km are only valid for the specific day, since the same pressure may represent a different altitude depending on the conditions in the atmosphere)*

While the cutoff rigidity for Berlin is about 2 to 3 GV the cutoff rigidity for Kiruna is below 1 GV and since more particles are able to enter the Earth's magnetosphere at lower cutoff rigidities, the maximum of the particle flux is located at a higher altitude for locations with lower cutoff rigidities.
Furthermore the comparison of the location of the maxima for count rates of all events and count rates in CsI(Na) shows that these are almost the same for each of the balloon flights. This supports the assumption that the measurements are dominated by events in CsI(Na).
For both balloon flights it is clearly visible that the location of the maximum of dose rates in BC-412 is at a lower altitude than the maximum of dose rates in CsI(Na). Even though events in BC-412, up to an energy of 15 MeV, are contaminated with γ-rays, a trend can be seen that the location of the maximum for dose rates dominated by neutron events is at a lower altitude than the location of the maximum for γ-rays and charged particles (events in CsI(Na)). This trend could be understood as a consequence of the longer mean free path for neutron in the Earth's atmosphere.

8.4 Spectrum of Events in BC-412 During the Floating Phase

Figure 8.20 shows the energy deposition spectra of events in BC-412 on ground (green), at airplane flight levels (red) and during the floating phase of the balloon (blue). The spectra on ground and at airplane flight levels have already been shown and analysed in Chapter 7. From the discussion in Chapter 7 it is known that the spectra of the events in BC-412 are spectra of neutral particles and that there is a contribution of γ-rays up to an energy of 15 MeV. The comparison of the spectrum at aircraft altitudes and during

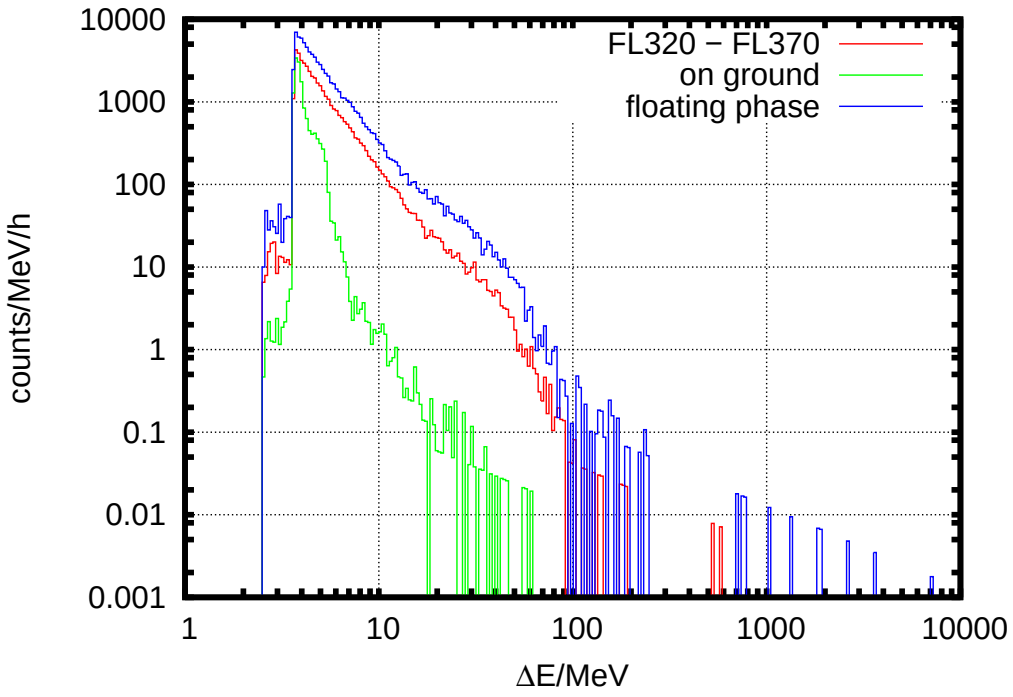

Figure 8.20: *Spectra of events in BC-412 on ground (green), at airplane flight levels (red) and during the floating phase of the balloon (blue)*

the floating phase shows that the latter has more events with energies higher than 100 MeV. This cannot be explained yet, since it is unclear which particle interactions with the instrument lead to these events (see Section 5.1). However, the shape of the two spectra up to an energy of 100 MeV seems to be similar.

For better comparison Fig. 8.21 shows the spectrum at aircraft flight levels and during the floating phase normalised to the spectrum during the floating phase. In the upper panel the spectrum is normalised to the low energy part of the spectrum, where it is influenced by γ-rays and in the lower panel the spectrum is normalised to the region of the spectrum where neutrons dominate. Differences between the two spectra are visible in both cases. The modulation of cosmic rays is similar during both flights, which could suggest that the spectra do not differ a lot. But for a detailed analysis, which is beyond the scope of this work, one also has to consider other factors, e.g. that the airplane flight took place at higher cutoff rigidities (about 3 GV to 10 GV) than the balloon flight. Also the contribution of γ-rays has to be taken into account.

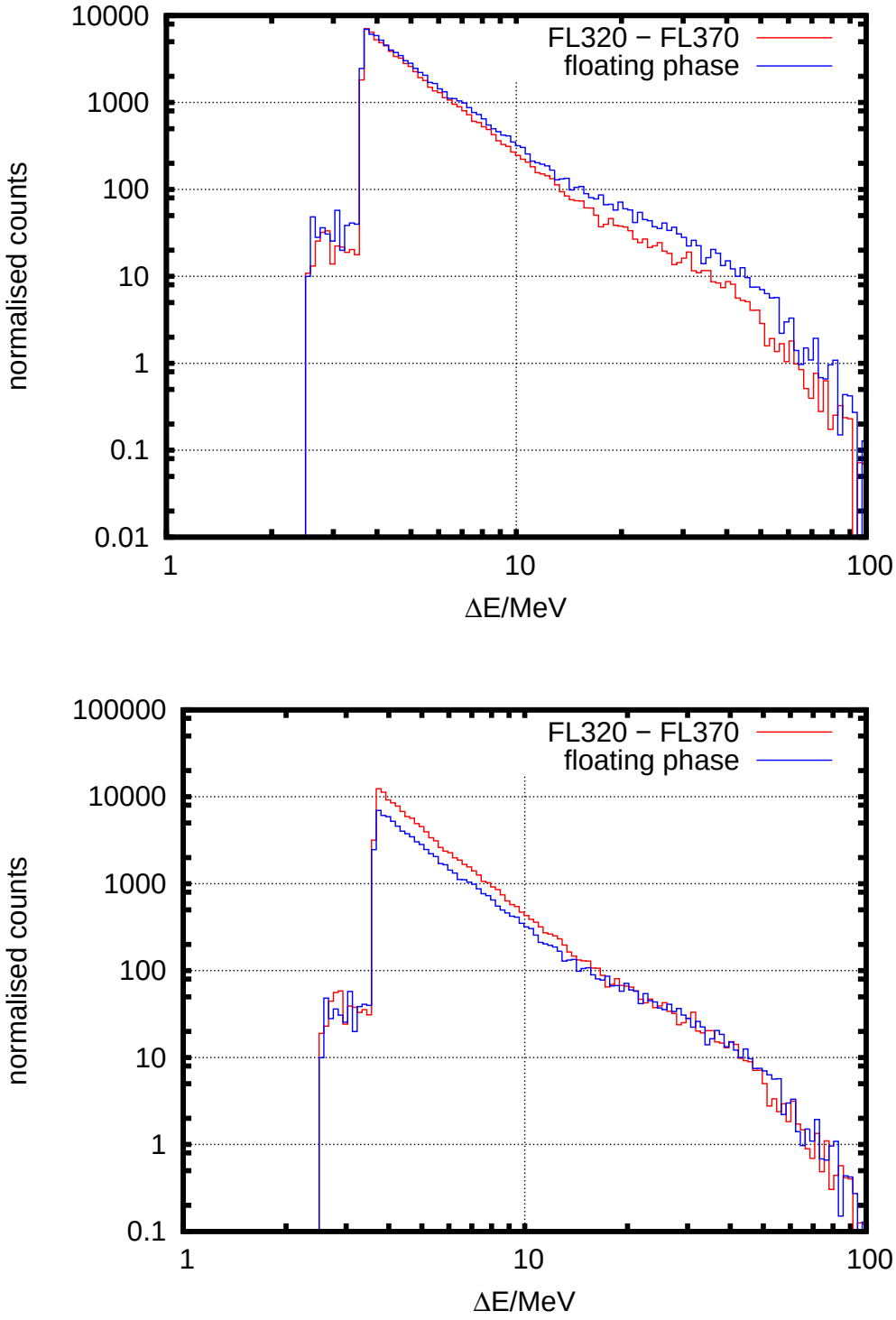

Figure 8.21: *Spectra at aircraft flight levels and during the floating phase normalized to the spectrum during the floating phase. Upper panel: Normalized to the region where the spectrum is influenced by γ-rays. Lower panel: Normalized to the region of the spectrum where neutron dominate the spectrum*

The results in this chapter clearly show that the developed Phoswich detector has been flown successfully on board two stratospheric balloons. During both flights the measured count rates show a maximum which corresponds to the Pfotzer maximum (Pfotzer, 1936). The analysis of the measured dose rates showed a maximum as well, which has also been mentioned in Bartlett (2004). In addition, the difference in the location of the maxima of dose rates from events in CsI(Na) and events in BC-412 could be understood as a hint that dose rates dominated by neutron events have their maximum at a lower altitude than the dose rates dominated by γ-rays and charged particles.

Chapter 9

Summary and Conclusions

In this work the Phoswich detector PING for neutron dose rate measurements in the Earth's atmosphere was developed, calibrated and flown successfully. Dose rate measurements have been performed during an airplane flight and stratospheric balloon flights. Furthermore a data analysis technique for the output data of this instrument, based on pulse shape analysis, was developed. The main results are presented in the following.

Calibration and Pulse Shape Analysis

The instrument was designed to measure neutrons with energies up to 100 MeV in the mixed radiation field of the Earth's atmosphere. Calibration measurements with neutrons from 5 MeV to 100 MeV showed that it is possible to measure 100 MeV neutrons with the developed instrument and that they can, in principle, be distinguished from other particle species. In the developed detector an anticoincidence made of CsI(Na) is used to discriminate against charged particles and to distinguish neutrons from γ-rays. By analysing the shape of the output pulses for different measurements with neutrons, γ-rays and charged particles, it was possible to distinguish events in the plastic scintillator (mainly caused by the interaction with neutrons) from events in the CsI(Na) (mainly charged particles and γ-rays) because of the different decay times of the two scintillators.

Contamination of the Neutron Channel

A GEANT4 simulation of the instrument showed that the inner plastic scintillator does not only respond to neutrons but also to γ-rays, although the response to γ-rays is much smaller than that to neutrons, depending on the

energy of the incident particle. A more detailed analysis of the spectra of events in the plastic scintillator on ground and at airplane flight levels indicated that the spectrum is influenced by γ-rays up to an energy of 15 MeV. Thus, events in the plastic scintillator with energies between the low energy threshold and 15 MeV are neutral particles and events with energies above 15 MeV up to 100 MeV are neutrons.

Measurements on Board Aircraft

The developed instrument has been flown successfully on board an airplane. To convert the measured events in the two scintillators into dose rates, the neutron calibration (equation 5.4) was used for the events in the plastic scintillator and the γ-ray calibration (equation 5.7) for the events in the CsI(Na). The dose rates in the CsI(Na) consist mainly of γ-rays and charged particles and the dose rates of the events in the plastic scintillator are caused by neutrons and γ-rays depending on the energy as mentioned above. The dose rates which have been measured during the airplane flight are in good agreement with measurements with other instruments. Dose rates in the CsI(Na) were compared to measurements with the DOSTEL instrument which measures mainly charged particles and the dose rates in the plastic scintillator were compared to measurements with the NEUDOS instrument which is dedicated to measure neutrons.

Measurements on Board Stratospheric Balloons

In addition to the airplane flight, the developed Phoswich detector has been flown on board two stratospheric balloons successfully. During these flights the altitude dependence of count rates and dose rates has been determined up to an altitude of almost 30 km. As expected the dose rates measured during the balloon flights reached higher values than the ones measured during the airplane flight. Analysing the count rates measured during the balloon flights a maximum was found which corresponds to the location of the Pfotzer maximum (Pfotzer, 1936). Additionally maxima in the dose rates of the events in both the CsI(Na) and BC-412 scintillator were found. Such a maximum of dose rates in the Earth's atmosphere is already mentioned in Bartlett (2004). Comparing the locations of the maxima for dose rates in CsI(Na) and BC-412 showed that the latter is found at lower altitudes for both balloon flights, which could be a hint that the maximum of dose rates caused mainly by neutrons is found at lower altitudes than the maximum of dose

rates of other particles.

To summarize, it was possible to measure fast neutrons in the mixed radiation field of the Earth's atmosphere with the Phoswich detector PING developed in this work. With the pulse shape analysis technique applied here it was possible to separate events in the plastic scintillator, which are mainly caused by the interaction with neutrons, from events in the CsI(Na) which are mainly caused by γ-rays and charged particles. The contamination of the neutron channel with γ-rays is only relevant up to an energy of 15 MeV. The instrument successfully measured dose rates on board an airplane and on board stratospheric balloons. The measured dose rates on board the airplane were in good agreement with measurements of other instruments. The measurements on board the stratospheric balloons showed maxima in the count rates as well as in the dose rates, which agree with values in the literature (Pfotzer (1936), Bartlett (2004)).

Chapter 10

Future Prospects

The Phoswich detector developed in this work was constructed mainly to measure dose rates caused by neutrons and to distinguish these from γ-rays and other particles. In order to use the developed instrument as a dosimeter some aspects have to investigated in more detail.

Calculation of the Dose Equivalent

In this work only the absorbed dose D has been calculated from the measured events, but this is not the relevant quantity in radiation protection. To use the developed detector as a dosimeter the dose equivalent H, which is a measurable quantity used in radiation protection, has to be determined. As explained in Section 2.5.1 the calculation of the dose equivalent requires the knowledge of the energy of the primary neutrons because the quality factor needed to convert absorbed dose into dose equivalent depends on this energy. But the spectra measured by the instrument are only energy deposition spectra and as mentioned above the spectrum of the events in the plastic scintillator does not only contain neutrons but also γ-rays to a certain extent, at least up to an energy of 15 MeV. To obtain a spectrum of primary neutrons first the influence of the spectrum by γ-rays has to be taken into account and has to be subtracted from the spectrum of the events in the BC-412. After that the measured spectrum has to be unfolded. One possibility to do this is the procedure developed in the dissertation of J. Köhler (Köhler, 2011).

Events above 100 MeV

An interesting effect that needs to be examined is that there are events recorded in the plastic scintillator which have energies higher than 100 MeV. The highest available neutron energy for calibration was 100 MeV, thus the instrument was calibrated up to this energy. As the neutron calibration for the events in the plastic scintillator is non-linear it is not easy to find a calibration function which can be extrapolated to energies higher than 100 MeV. The calibration function which is used in this work overestimates the energy of the events above 100 MeV, thus, these events are not taken into account for the calculation of the absorbed dose rates. The comparison of the spectra of events in the plastic scintillator at airplane flight level and during the floating phase of the balloon flight showed that there are more events above an energy of 100 MeV at higher altitudes. So far it is unclear which interaction in the instrument causes these events with energies higher than 100 MeV. As these are events interacting only in the plastic scintillator they cannot be caused by charged particles because in this case the result should be a mixed signal from both scintillators. On the other hand when considering the geometry of the detector it becomes evident that it is not possible to stop neutrons with an energy of much more than 100 MeV.
In order to calculate the total absorbed dose measured by the instrument these events have to be identified and they have to be converted into the right energy in order to calculate the right dose caused by these events.

Events in the Lower Finger

Another effect which has not been dealt with in this work are the events in the lower finger. These events have not been taken into account for the calculation of the absorbed dose, because so far no energy calibration is available for them. It is a bit complicated to classify these events because from the analysis of their pulse shape they seem to be mixed events taking place in both scintillators but in the 2d-histogram plots (see e.g. Fig. 7.1) it seems that these are events only in the plastic scintillator. The fact that these events are not contained in the upper or middle finger indicates that they have a different phase. Thus, it could be that the phase as well as the amplitude of these events is not determined correctly, which makes it difficult to identify their origin.

To conclude, when the open issues mentioned above are investigated in detail, it could be possible to use the developed Phoswich detector for measurements of primary neutrons in the Earth's atmosphere and to be able to calculate the total absorbed dose as well as the total dose equivalent.

Bibliography

Alberts, W. G., Beaujean, R., Böhm, J., Pychlau, P., Reitz, G., Schnepel, G. H., Winkelmann, I., 1997. Die Ermittlung der durch kosmische Strahlung verursachten Strahlenexposition des fliegenden Personals. Berichte der Strahlenschutzkommission (SSK) des Bundesministeriums für Umwelt, Naturschutz und Reaktorsicherheit Heft 1 (1997).

Allkofer, O. C., 1975. Introduction to Cosmic Radiation. Buchreihe der Atomkernenergie. Verlag Karl Thiemig.

Allkofer, O. C., Grieder, P. K. F., 1983. Cosmic Rays on Earth. Physik Daten 25-1 1984, Fachinformationszentrum Energie Physik Mathematik GmbH Karlsruhe.

Bartlett, D. T., 2004. Radiation Protection Aspects of the Cosmic Radiation Exposure of Aircraft Crew. Radiation Protection Dosimetry 109 (4), 349–355.

Beaujean, R., Burmeister, S., Petersen, F., Reitz, G., 2005. Radiation Exposure Measurement Onboard Civil Aircraft. Radiation Protection Dosimetry 116 (1-4), 312–315.

Beaujean, R., Kopp, J., Reitz, G., 1999. Radiation Exposure in Civil Aircraft. Radiation Protection Dosimetry 85 (1-4), 287–290.

Berger, M. J., Coursey, J. S., Zucker, M. A., Chang, J., 2005a. ESTAR, PSTAR, and ASTAR: Computer Programs for Calculating Stopping-Power and Range Tables for Electrons, Protons, and Helium Ions (version 1.2.3) [Online] Available. National Institute of Standards and Technology, Gaithersburg, MD.
URL `http://physics.nist.gov/PhysRefData/Star/Text/programs.html` `[01.01.2013]`

Berger, M. J., Coursey, J. S., Zucker, M. A., Chang, J., 2005b. ESTAR, PSTAR, and ASTAR: Computer Programs for Calculating Stopping-

Power and Range Tables for Electrons, Protons, and Helium Ions (version 1.2.3) [Online] Available. National Institute of Standards and Technology, Gaithersburg, MD.
URL http://physics.nist.gov/Star [21.09.2012]

Berger, M. J., Coursey, J. S., Zucker, M. A., Chang, J., 2005c. ESTAR, PSTAR, and ASTAR: Computer Programs for Calculating Stopping-Power and Range Tables for Electrons, Protons, and Helium Ions (version 1.2.3) [Online] Available. National Institute of Standards and Technology, Gaithersburg, MD.
URL http://physics.nist.gov/Star [22.11.2012]

Birks, J. B., 1964. Chapter 3 - The Scintillation Process In Organic Materials—I. In: Birks, J. B. (Ed.), The Theory and Practice of Scintillation Counting. International Series of Monographs in Electronics and Instrumentation. Pergamon, pp. 39 – 67.

Böttcher, S. I., 2011. Analysis of a ^{207}Bi spectrum measured with a Hamamatsu photo diode, a TSH310 based preamp, and the HETI IRENA. Internal Report (revision 494), University of Kiel.
URL http://www.ieap.uni-kiel.de/et/people/stephan/solo/spectra/irena/2011-06-01-Bi207.pdf

Brooks, F. D., 1979. Development of Organic Scintillators. Nuclear Instruments and Methods 162 (1–3), 477 – 505.

Burmeister, S., 2006. Entwicklung eines Neutronendosimeters und Messung schneller Neutronen in der Verkehrsluftfahrt. Dissertation, Christian-Albrechts-Universität zu Kiel.

DETEC, 10.01.14. Scintillating-products.
URL http://www.detec-rad.com/dl/Scint_Brochure.pdf

Dönsdorf, E. M., 2007. Messung der Photonenkomponente in der unteren Erdatmosphäre. Diploma thesis, Christian-Albrechts-Universität zu Kiel.

Dow Corning, 07.12.2012. DOW CORNING®93-500 SPACE–GRADE ENCAPSULANT.
URL http://www.syscoindia.com/catalogs/DC-93-500.pdf

European Commission, 1996. Radiation Protection 85: Exposure of Air Crew to Cosmic Radiation. EURADOS report 1996-01. European Commission, Directorate-General for Environment, Nuclear Safety, and Civil Protection, A report of EURADOS Working Group 11 'The radiation exposure and

monitoring of air crew'. Edited by I. R. McAulay, D. T. Barlett, G. Dietze, H. G. Menzel, K. Schnuer and U. J. Schrewe.

Evans, R. D., 1955. The atomic nucleus. International series in pure and applied physics. McGraw-Hill.

GeoExplo Ltda., 22.11.12. Airborne Gamma-Ray Spectrometry Surveys. URL `http://www.geoexplo.com/airborne_survey_workshop_rad.html`

Goldhagen, P., Clem, J. M., Wilson, J. W., 2003. Recent results from measurements of the energy spectrum of cosmic-ray induced neutrons aboard an ER-2 airplane and on the ground. Advances in Space Research 32 (1), 35 – 40.

Goldhagen, P., Clem, J. M., Wilson, J. W., 2004. The energy spectrum of cosmic-ray induced neutrons measured on an airplane over a wide range of altitude and latitude. Radiation Protection Dosimetry 110 (1-4), 387–392.

Grieder, P. K. F., 2001a. Chapter 1 - Cosmic Ray Properties, Relations and Definitions. In: Grieder, P. K. F. (Ed.), Cosmic Rays at Earth: Researcher's Reference Manual and Data Book, 1st Edition. Elsevier Science Limited, pp. 1 – 53.

Grieder, P. K. F., 2001b. Cosmic Rays at Earth: Researcher's Reference Manual and Data Book, 1st Edition. Elsevier Science Limited.

Hamamatsu/HV, 23.09.2012. High voltage DC-DC-converter C4900-01. URL `http://sales.hamamatsu.com/assets/pdf/parts_C/C4900_TACC1013E04.pdf`

Hamamatsu/PMT-handbook, 06.01.2013. Photomultiplier Tubes Basics and Applications, third edition. URL `http://sales.hamamatsu.com/assets/applications/ETD/pmt_handbook_complete.pdf`

Hamamatsu/R5070A, 21.09.2012. Data sheet for R5070A. URL `http://sales.hamamatsu.com/assets/pdf/parts_R/R5070A.pdf`

Heber, B., 2001. Modulation of galactic and anomalous cosmic rays in the inner heliosphere. Advances in Space Research 27 (3), 451 – 460.

Heber, B., Kopp, A., Gieseler, J., Müller-Mellin, R., Fichtner, H., Scherer, K., Potgieter, M. S., Ferreira, S. E. S., 2009. Modulation of galactic cosmic ray protons and electrons during an unusual solar minimum. The Astrophysical Journal 699 (2), 1956 – 1963.

Herbst, K., 2012. Interaction of Cosmic Rays with the Earth's Magnetosphere and Atmosphere. Dissertation, Christian-Albrechts-Universität zu Kiel.

Herbst, K., 2013. Private communications.

Hess, V. F., 1912. Über Beobachtungen der durchdringenden Strahlung bei sieben Freiballonfahrten. Physik. Zeitschr. XIII, 1084–1091.

Hörandel, J. R., 2008. The origin of galactic cosmic rays. Nuclear Instruments and Methods in Physics Research Section A: Accelerators, Spectrometers, Detectors and Associated Equipment 588 (1–2), 181 – 188, Proceedings of the First International Conference on Astroparticle Physics-RICAP 07.

ICRP, 1991. 1990 Recommendations of the International Commission on Radiological Protection. ICRP Publication 60. Ann. ICRP 21 (1-3).

ICRP, 2003. Relative Biological Effectiveness (RBE), Quality Factor (Q), and Radiation Weighting Factor (w_R). ICRP Publication 92. Ann. ICRP 33 (4).

ICRP, 2007. The 2007 Recommendations of the International Commission on Radiological Protection. ICRP Publication 103. Ann. ICRP 37 (2-4).

ICRU, 2010. Reference Data for the Validation of Doses from Cosmic-Radiation Exposure of Aircraft Crew. ICRU Report 84 (prepared jointly with ICRP). Journal of the ICRU 10 (2), 2010.

Inga, M., 29.10.12. Private communication.

Knoll, G. F., 2000. Radiation Detection and Measurement, 3rd Edition. John Wiley and Sons, Inc.

Köhler, J., 2011. Gamma/neutron separation in the Martian radiation environment. Dissertation, Christian-Albrechts-Universität zu Kiel.

Leo, W. R., 1987. Techniques for Nuclear and Particle Physics Experiments. Springer-Verlag Berlin Heidelberg.

Lindborg, L., Kyllönen, J.-E., Beck, P., Bottollier-Depois, J.-F., Gerdung, S., Grillmaier, R. E., Schrewe, U., 1999. The Use of TEPC for Reference Dosimetry. Radiation Protection Dosimetry 86 (4), 285–288.

Marquardt, J., 2012. Private communication.

Marquardt, J., 2013. Private communication.

McKibben, R. B., 2009. Private communications.

McKibben, R. B., Connell, J. J., Bancroft, C. M., Bravar, U., Pirard, B., Wood, J. R., 2008. Development of a Miniature Phoswich-Based Detector for 1-10 MeV Solar Neutrons. 37th COSPAR General Assembly, Montreal, Canada, July 2008, Paper D23-0051-08.

McKibben, R. B., Connell, J. J., Macri, J. R., McConnell, M. L., Ryan, J. M., Flückiger, E. O., Moser, M. R., Brown, J. C., McKinnon, A. L., 2005. Applications of a phoswich-based detector for fast ($\sim$ 1-10 MeV) solar neutrons for missions to the inner heliosphere. Advances in Space Research 36, 1432–1438.

Millipore, 27.11.2012. MF-Millipore Membrane Filter.
URL `http://www.millipore.com/catalogue.nsf/docs/HAWP29325`

MONSTA, 25.11.2012. Measurement Of Neutrons with Scintillators in The Atmosphere.
URL `http://www.physik.uni-kiel.de/monsta/`

Naebert, T., 2011. Private communication.

Naebert, T., 2013. Private communication.

NMDB, 27.03.2013. Neutron Monitor Database website.
URL `www.nmdb.eu/nest/search.php`

NuDat2, 15.11.2012. National Nuclear Data Center, information extracted from the NuDat 2 database.
URL `http://www.nndc.bnl.gov/nudat2/`

Nusil Silicone Technology, 09.02.2011. Data sheet Nusil CV-1152.
URL `http://www.polytec-pt.de/ger/_files/DBnusCV-1152.pdf`

O'Brien, K., Friedberg, W., Sauer, H. H., Smart, D. F., 1996. Atmospheric cosmic rays and solar energetic particles at aircraft altitudes. Environment International 22, Supplement 1 (0), 9 – 44.

Pfotzer, G., 1936. Dreifachkoinzidenzen der Ultrastrahlung aus vertikaler Richtung in der Stratosphäre. Zeitschrift für Physik 102 (1-2).

Podgoršak, E. B., 2010. Radiation Physics for Medical Physicists, 2nd Edition. Biological and Medical Physics, Biomedical Engineering. Springer Berlin Heidelberg.

Potgieter, M. S., 1998. The modulation of galactic cosmic rays in the heliosphere: Theory and models. Space Science Reviews 83 (1-2), 147–158.

Price, W. J., 1964. Nuclear Radiation Detection, 2nd Edition. McGraw-Hill Series in Nuclear Engineering. McGraw-Hill.

Reitz, G., 1993. Radiation environment in the stratosphere. Radiation Protection Dosimetry 48 (1), 5–20.

Reitz, G., 2008. Characteristic of the radiation field in low earth orbit and in deep space. Zeitschrift für Medizinische Physik 18 (4), 233 – 243.

REXUS/BEXUS, 20.11.2012. REXUS/BEXUS - Rocket and Balloon Experiments for University Students.
URL http://www.rexusbexus.net/

Rhodorsil, 30.11.2010. Data sheet Rhodorsil RTV141.
URL http://www.bentleychemicals.co.uk/files/RTV141_1.pdf

Rinck Electronic GmbH, 08.10.2012. Temperatursensor PT1000, Temperatur/Widerstandstabelle, Bereich-50-+200°C.
URL http://www.rinck-electronic.de/rinck2001/pdf/AN_T303_D_PT1000_Temperaturtabelle.PDF

Roos, F., 1997. Messung der Strahlenexposition in Verkehrsflugzeugen mit einem Halbleiterdetektor. Diploma thesis, Christian-Albrechts-Universität zu Kiel.

Röttger, S., 2012. Private communication.

Saint-Gobain/BC-412, 21.09.2012. Data sheet for BC-412.
URL http://www.detectors.saint-gobain.com/uploadedFiles/SGdetectors/Documents/Product_Data_Sheets/BC400-404-408-412-416-Data-Sheet.pdf

Saint-Gobain/CsI, 21.09.2012. Data sheet for CsI.
URL http://www.detectors.saint-gobain.com/uploadedFiles/SGdetectors/Documents/Product_Data_Sheets/CsI(Na)-CsI(Tl)-Data-Sheet.pdf

Saint-Gobain/detectors, 03.12.12.
URL http://www.detectors.saint-gobain.com/uploadedFiles/SGdetectors/Documents/Brochures/Organics-Brochure.pdf

Seimetz, L., 2012. Private communication.

SIDC-team, 1957-2013. The International Sunspot Number. Monthly Report on the International Sunspot Number, online catalogue.
URL `http://www.sidc.be/sunspot-data/`

Simpson, J. A., 1983. Elemental and isotopic composition of the galactic cosmic rays. Annual Review of Nuclear and Particle Science 33 (1), 323–382.

Simpson, J. A., 2000. The cosmic ray nucleonic component: The invention and scientific uses of the neutron monitor – (keynote lecture). Space Science Reviews 93 (1-2), 11–32.

Takada, M., Taniguchi, S., Nakamura, T., Nakao, N., Uwamino, Y., Shibata, T., Fujitaka, K., 2002. Characteristics of a phoswich detector to measure the neutron spectrum in a mixed field of neutrons and charged particles. Nuclear Instruments and Methods in Physics Research Section A: Accelerators, Spectrometers, Detectors and Associated Equipment 476 (1–2), 332–336.

Thomas, D. J., Alevra, A. V., 2002. Bonner sphere spectrometers—a critical review. Nuclear Instruments and Methods in Physics Research Section A: Accelerators, Spectrometers, Detectors and Associated Equipment 476 (1–2), 12 – 20.

Tsoulfanidis, N., Landsberger, S., 2011. Measurement and Detection of Radiation, 3rd Edition. CRC Press Taylor & Francis Group.

Turner, J. E., 1995. Atoms, Radiation, and Radiation Protection, 2nd Edition. John Wiley & Sons, Inc.

UNSCEAR, 16.01.14a. Report of the United Nations Scientific Committee on the Effects of Atomic Radiation to the General Assembly.
URL `http://www.unscear.org/unscear/en/publications/2000_1.html`

UNSCEAR, 16.01.14b. UNSCEAR 2000 Report Vol. I Sources and Effects of Ionizing Radiation Annex B: Exposures from natural radiation sources.
URL `http://www.unscear.org/unscear/en/publications/2000_1.html`

UNSCEAR, 16.01.14c. UNSCEAR 2000 Report Vol. I Sources and Effects of Ionizing Radiation Annex E: Occupational radiation exposures.
URL `http://www.unscear.org/unscear/en/publications/2000_1.html`

Watanabe, T., Arakawa, H., Kajimoto, T., Iwamoto, Y., Satoh, D., Kunieda, S., Noda, S., Shigyo, N., Ishibashi, K., Nakamura, T., Haight, R. C., 2008.

Performance of a phoswich detector composed of an inner NaI(Tl) crystal and surrounding NE102A plastic scintillator for neutron spectrometry. Nuclear Instruments and Methods in Physics Research Section A: Accelerators, Spectrometers, Detectors and Associated Equipment 587 (1), 20–28.

wetteronline.de, 22.01.2014. Wetter im Rückblick, Wetterstation Kiruna Airport, Luftdruck [hPa] vom 02.09.2012 bis 30.09.2012.
URL http://www.wetteronline.de/wetterdaten/kiruna?pcid=pc_rueckblick_data&gid=02044&pid=p_rueckblick_diagram&sid=StationHistory&iid=02044&paraid=PDLD&period=4&month=09&year=2012

Appendix A

Light Yield of CsI(Na) and BC-412

The values given for the light yield of BC-412, CsI(Na) and anthracene are listed in Table *A*.1.

material	light yield	Reference
BC-412	60 % of anthracene	Saint-Gobain/detectors (03.12.12)
CsI(Na)	85 % of NaI	DETEC (10.01.14)
anthracene	40 to 50 % of NaI	Saint-Gobain/detectors (03.12.12)

Table A.1: *Light yield of different scintillator materials*

The ratio between the light yield of CsI and BC-412 is about 3.15.

Appendix B

100 MeV Neutron Measurement

In the upper panel of Fig. $B.1$ the raw data of the 100 MeV measurement are shown. It is clearly visible that there is an additional branch located below the lower finger. This branch is also found in the measurements with 66 MeV, the two measurements on board airplanes and the measurements on board balloons.
In the lower panel of Fig. $B.1$ the processed data are displayed. To get this plot the conditions to sort out wrong data points listed in Chapter 4 were applied. The additional branch could be reduced significantly with these conditions so that now it is merely a tail of the palm population. For the data analysis the events in the additional branch are treated as palm events.
There is another feature seen in the palm events of the processed data. Some events seem to be set apart from the palm itself and form a parallel line to the other palm events. This effect is only seen in the 100 MeV and the 66 MeV neutron measurements. It has not been investigated in detail. It could be that this feature is caused by a non-linearity in the pulse height S which would be an indication that the cut used for S is not strong enough. In this work these events are also considered to belong to the palm population.

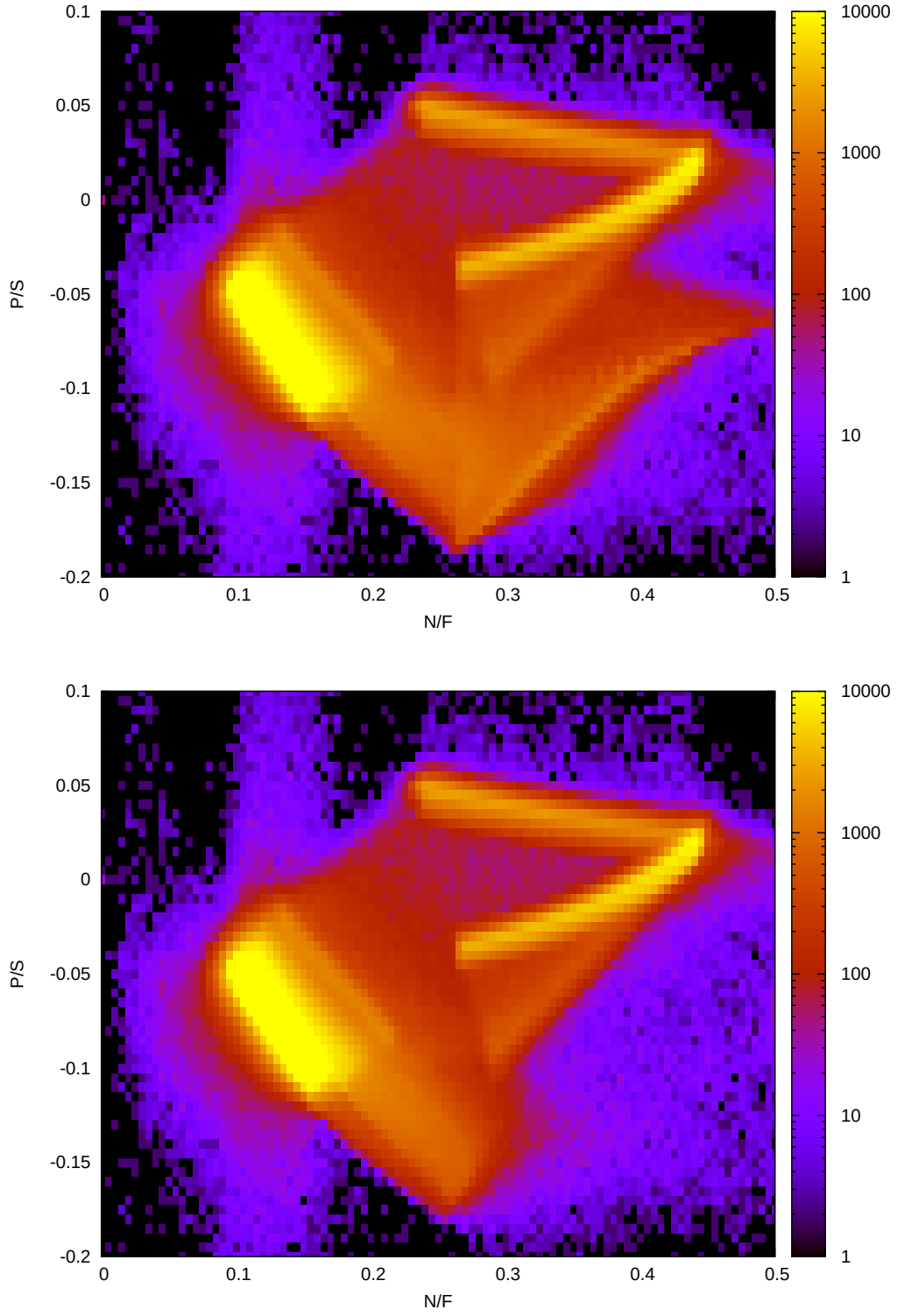

Figure B.1: *Upper panel: Raw data of the 100 MeV neutron measurement. Lower panel: Processed data of the 100 MeV neutron measurement*

Appendix C

Histogram and Integrated Histogram of λ

The histogram and the integrated histogram of λ as well as a fit to the rising part of the integrated histogram is shown in Fig. $C.1$ for the palm events (upper panel) and for the events in the middle and lower finger (lower panel).

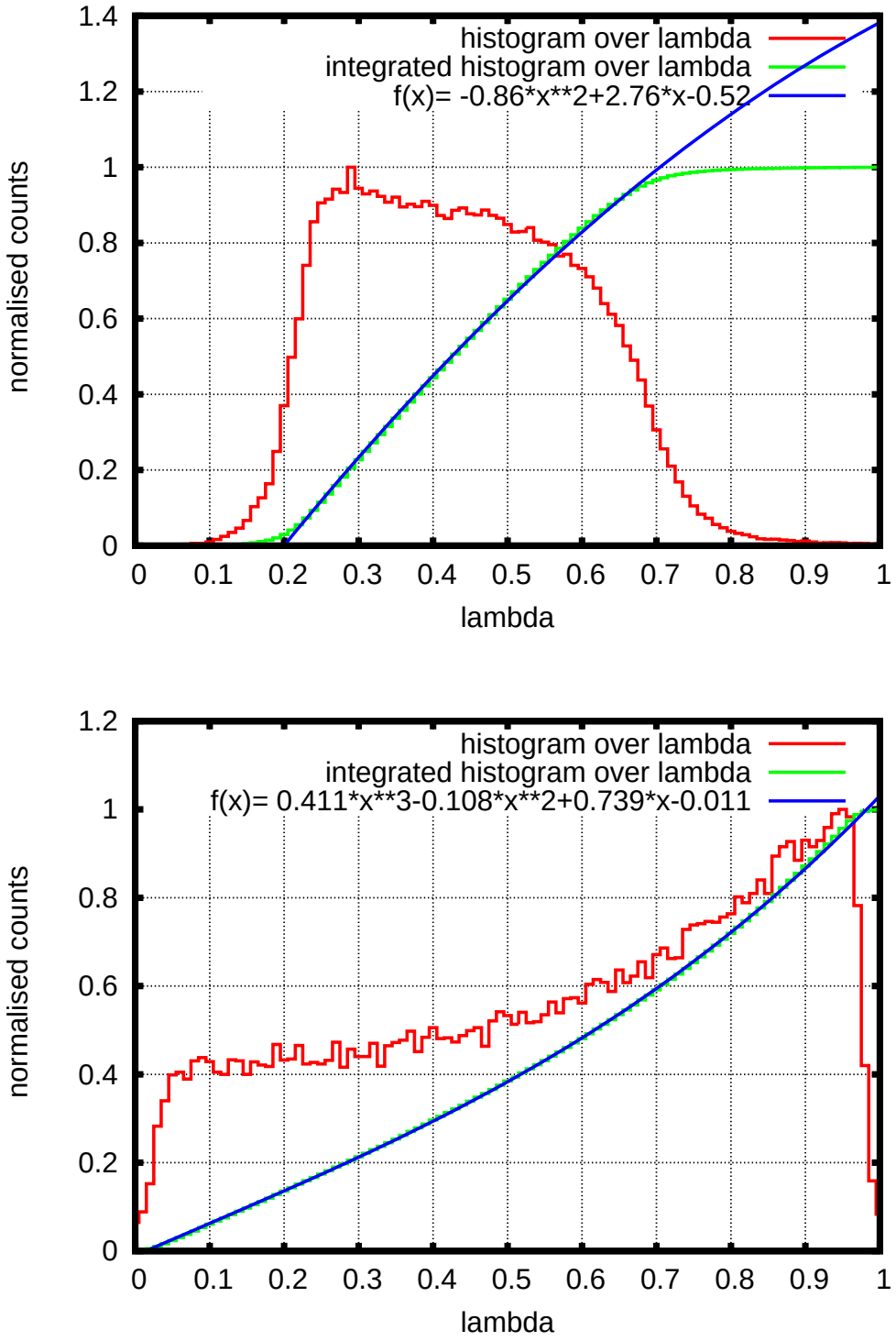

Figure C.1: *Histogram and integrated histogram for the palm events (upper panel) and for the events in the middle and lower finger (lower panel)*

Appendix D

Measurement with ^{137}Cs

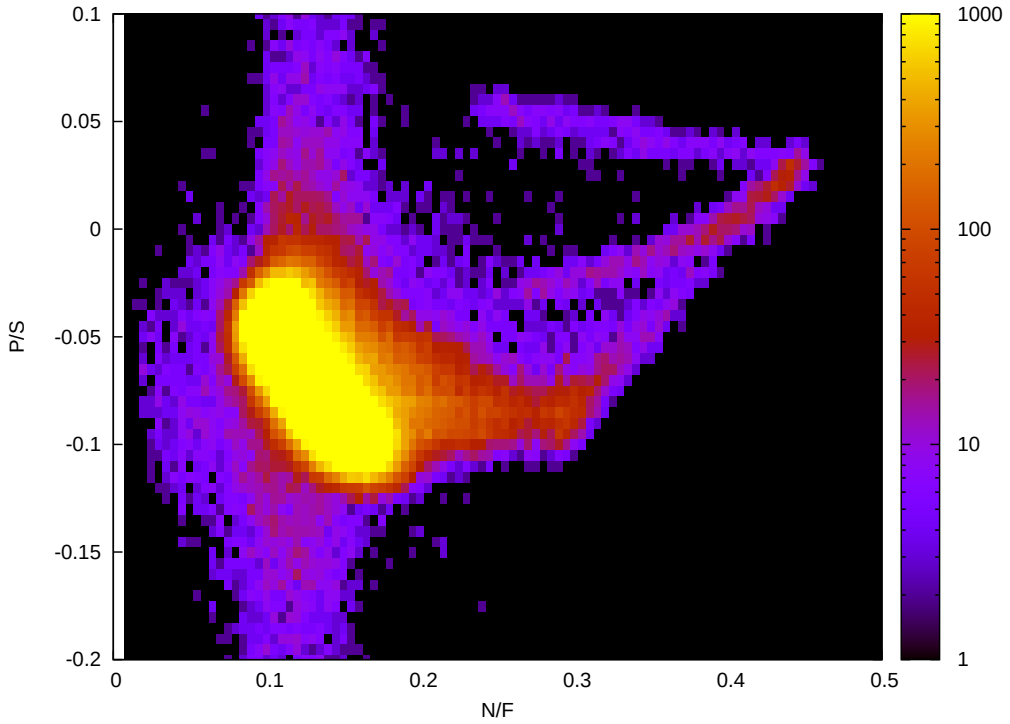

Figure D.1: *Measurement with ^{137}Cs*

In Fig. *D*.1 the measurement with ^{137}Cs is shown. In this measurement the four populations discussed in Chapter 4 are visible but the three fingers are not very prominent. Instead there are a lot of palm events and another population that goes from the palm towards and into the lower finger. This population could be Compton electrons which leave the CsI(Na) and enter

the BC-412. The lack of finger events is as expected because ^{137}Cs is a γ-ray source and thus many events in the CsI(Na) scintillator caused by the γ-rays are to be expected. As the duration of this measurement was only two hours not many neutrons are expected to be measured on ground.

Appendix E

Background Measurements at iThemba

At the iThemba beam line background measurements can be performed at an angle of 16° with respect to the primary beam. In Fig. $E.1$ the 66 MeV and the 100 MeV neutron measurement are shown with the corresponding background measurements. The additional peak is clearly visible in the measurements at the 0° position but only very slightly in the measurements of the 16° position. It is concluded that the additional peaks are the result of an interaction of the incident neutrons with the instrument (see discussion Chapter 5).

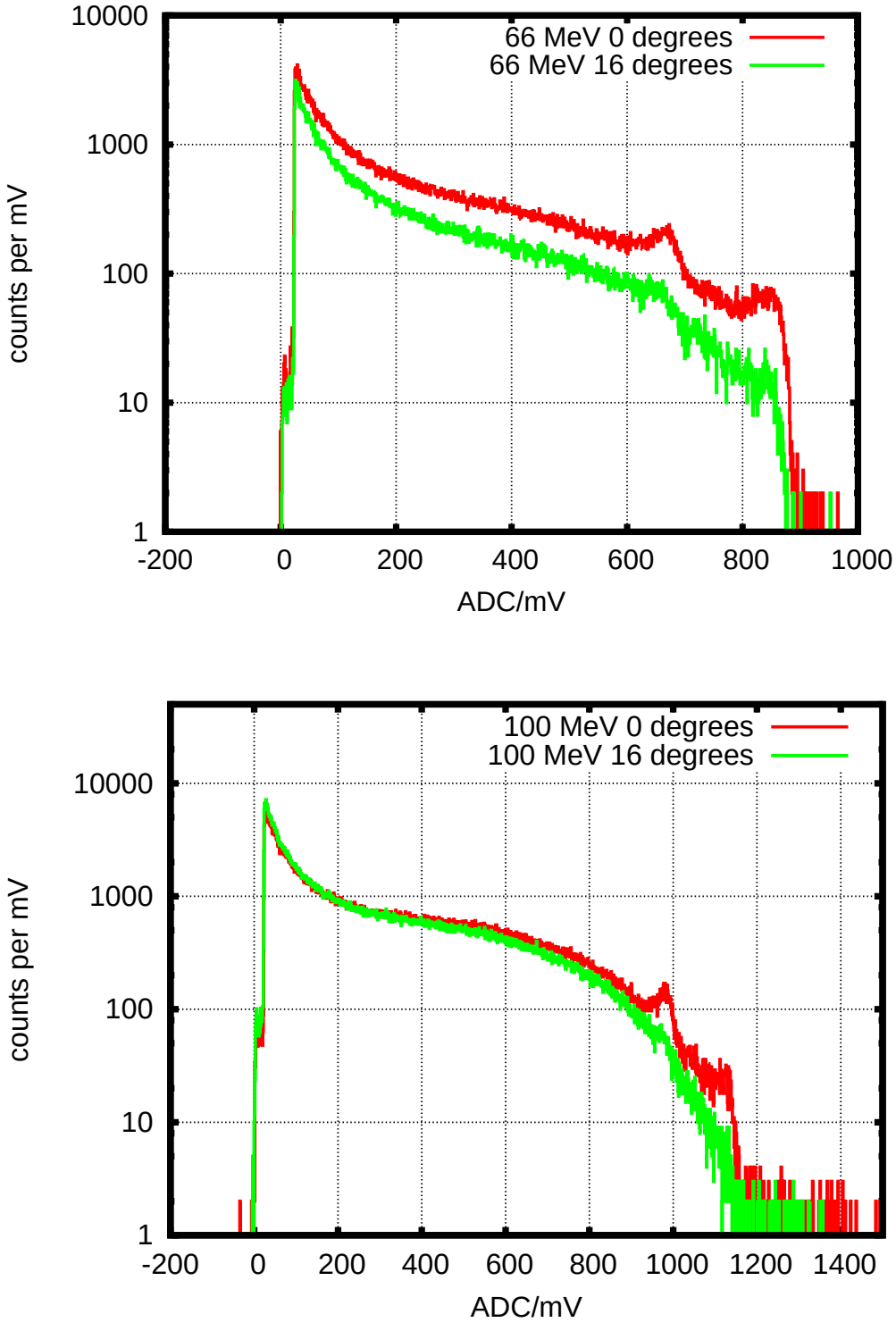

Figure E.1: *Upper panel: 66 MeV neutron measurement with the corresponding background measurement. Lower panel: 100 MeV neutron measurement with the corresponding background measurement*

Appendix F

Correction of Balloon Flight Data

F.1 Weather Balloon

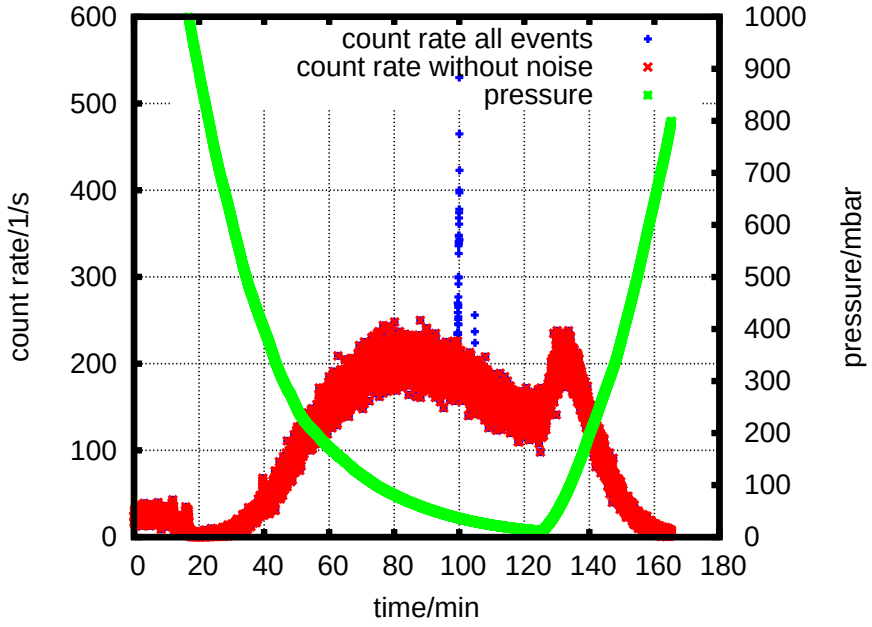

Figure F.1: *Time profile of the balloon flight: count rates of all events in the instrument with (blue) and without (red) noise peak as well as the pressure measured by the pressure sensor of the Phoswich detector displayed versus the time in minutes*

Figure *F*.1 shows the count rate profile of the processed data with and without a noise peak. For the further data analysis in Chapter 8 the count rate without the noise peak is used.
When the separate count rates for events in CsI(Na) and BC-412 are calculated, the noise peak displayed in Figure *F*.1 leads to two point of higher count rate at 100 and 101 minutes in both cases. In the upper and lower panel of Fig. *F*.2 the uncorrected and corrected count rates for events in CsI(Na) and BC-412 are displayed over the time and over the pressure of the instrument, respectively. For the data analysis in Fig. 8.7 the corrected count rates are used. In Fig. *F*.3 the dose rate profiles for events in CsI(Na) and BC-412 are shown. The noise peak displayed in Fig. *F*.1 causes elevated dose rates at the same time. While in the dose rates of events in CsI(Na) one point of increased dose is found, two points of elevated dose rate are visible in the dose rates of events in BC-412. For the further data analysis in Chapter 8 the dose rates without the points of elevated dose rate are used.

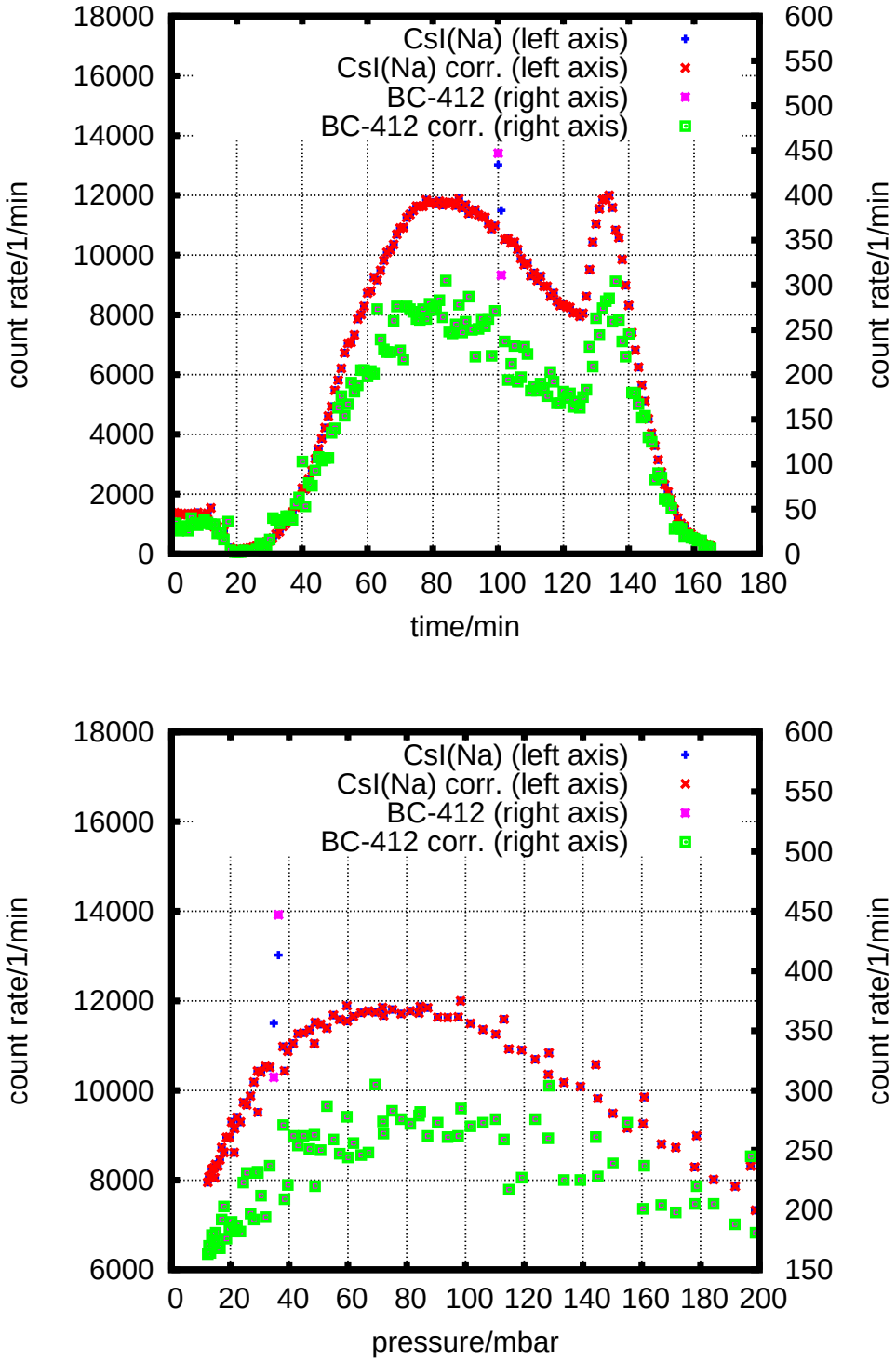

Figure F.2: *Upper panel: Separate count rates of events in CsI(Na) and BC-412 with and without noise versus the time in minutes. Lower panel: The same data as in the upper panel but shown versus the pressure of the instrument in millibar*

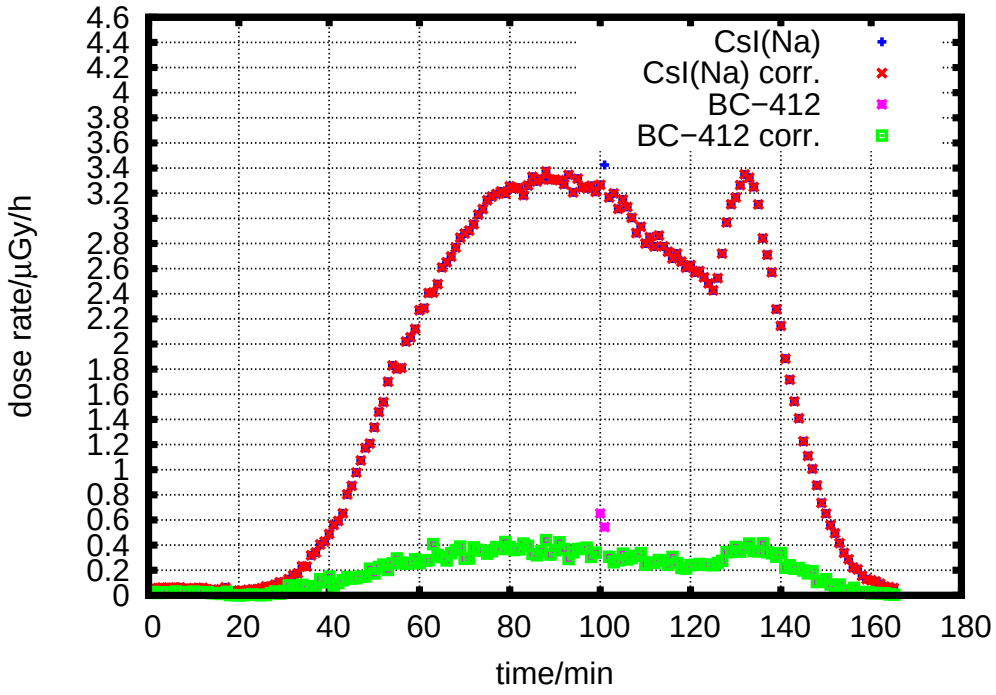

Figure F.3: *Dose rate profile for events in CsI(Na) and events in BC-412. Shown here are the dose rates with (blue and pink) and without (red and green) points of increased dose caused by noise*

F.2 BEXUS Balloon

In Fig. *F.*4 the count rate profile for all events is shown with and without the noise peak. For the further data analysis the data without the noise peak are used. In addition to the noise peak seen here, there were a few events with a wrong pressure value, these are also excluded from the data analysis.

The upper and lower panel of Fig. *F.*5 show the separate count rates for events in CsI(Na) and BC-412 with and without the noise versus the time in minutes and versus the pressure of the pressure sensor of the instrument, respectively. For the further data analysis the data without the noise are used.

In the upper and the lower panel of Fig. *F.*6 the dose rates of events in CsI(Na) and events in BC-412 with and without noise versus time in minutes and versus the pressure of the pressure sensor of the instrument are displayed, respectively. For the further data analysis the data without noise are used.

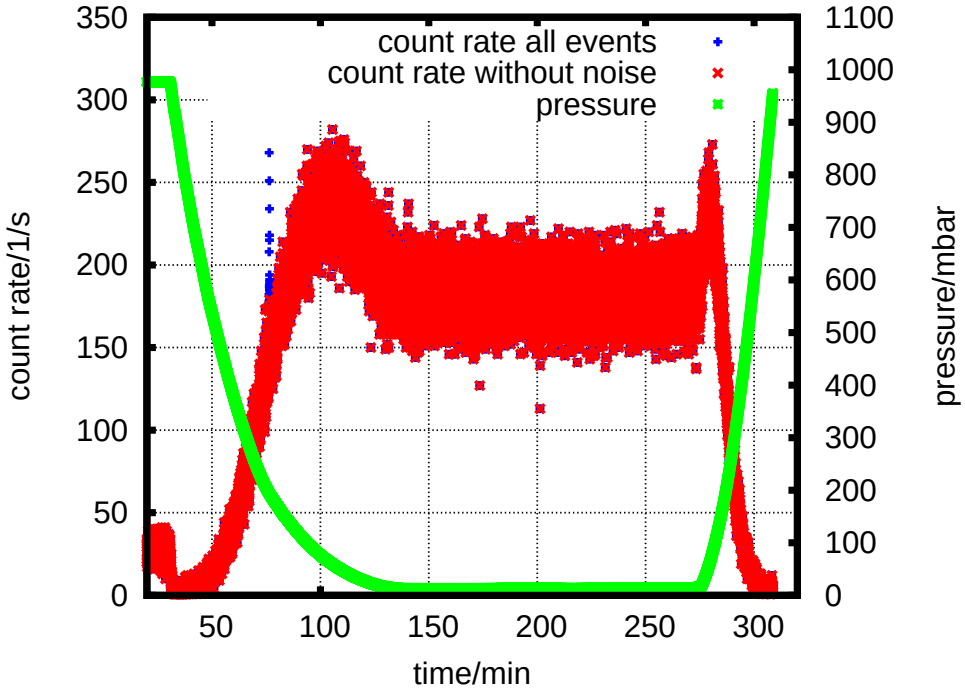

Figure F.4: *Time profile of the balloon flight: count rates of all events in the instrument with (blue) and without (red) noise peak as well as the pressure measured by the pressure sensor of the instrument shown versus the time in minutes*

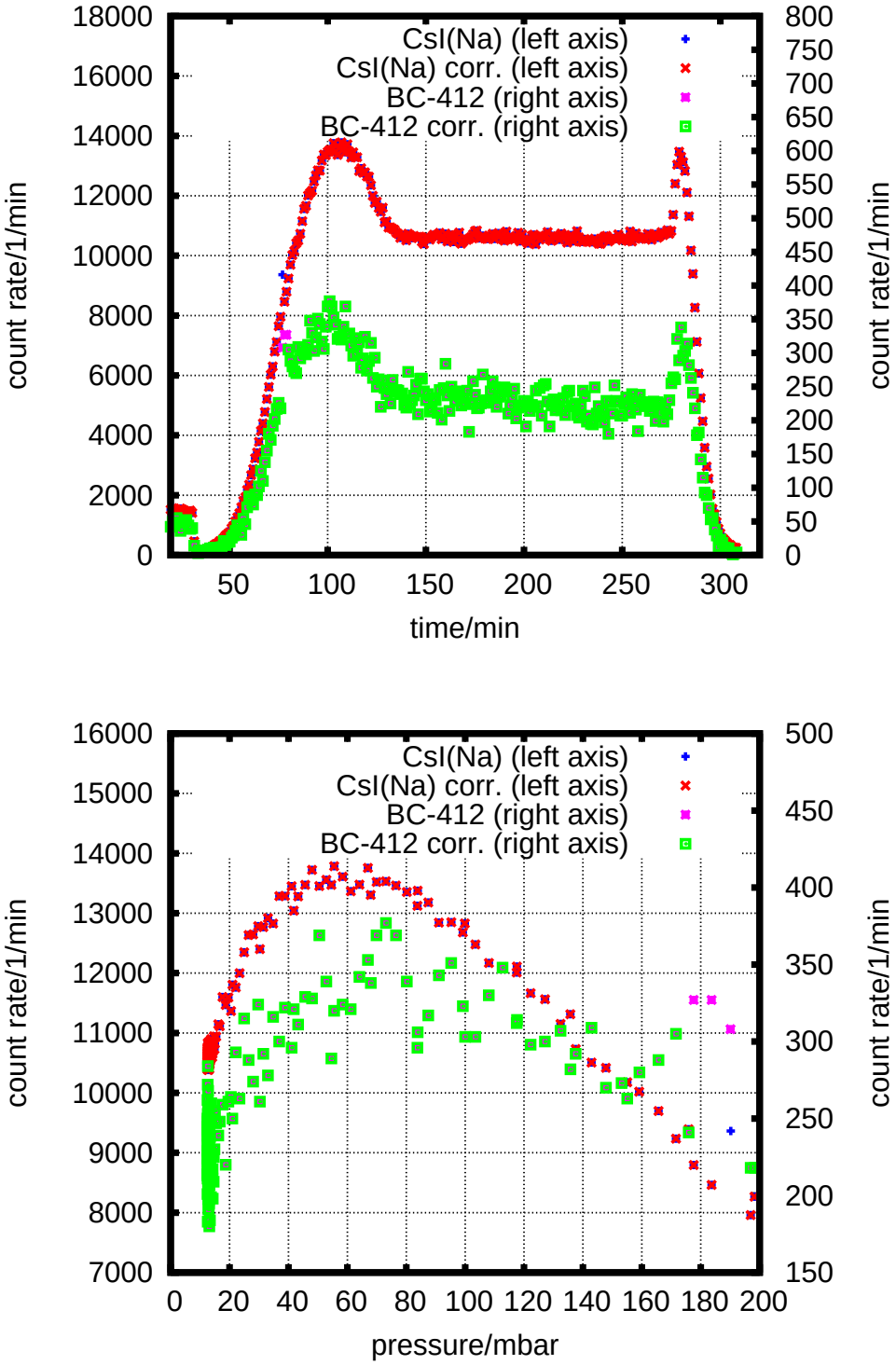

Figure F.5: *Upper panel: Separate count rates for events in CsI(Na) and events in BC-412 with and without noise versus the time in minutes. Lower panel: The same data as in the upper panel but shown versus the pressure measured by the pressure sensor of the instrument*

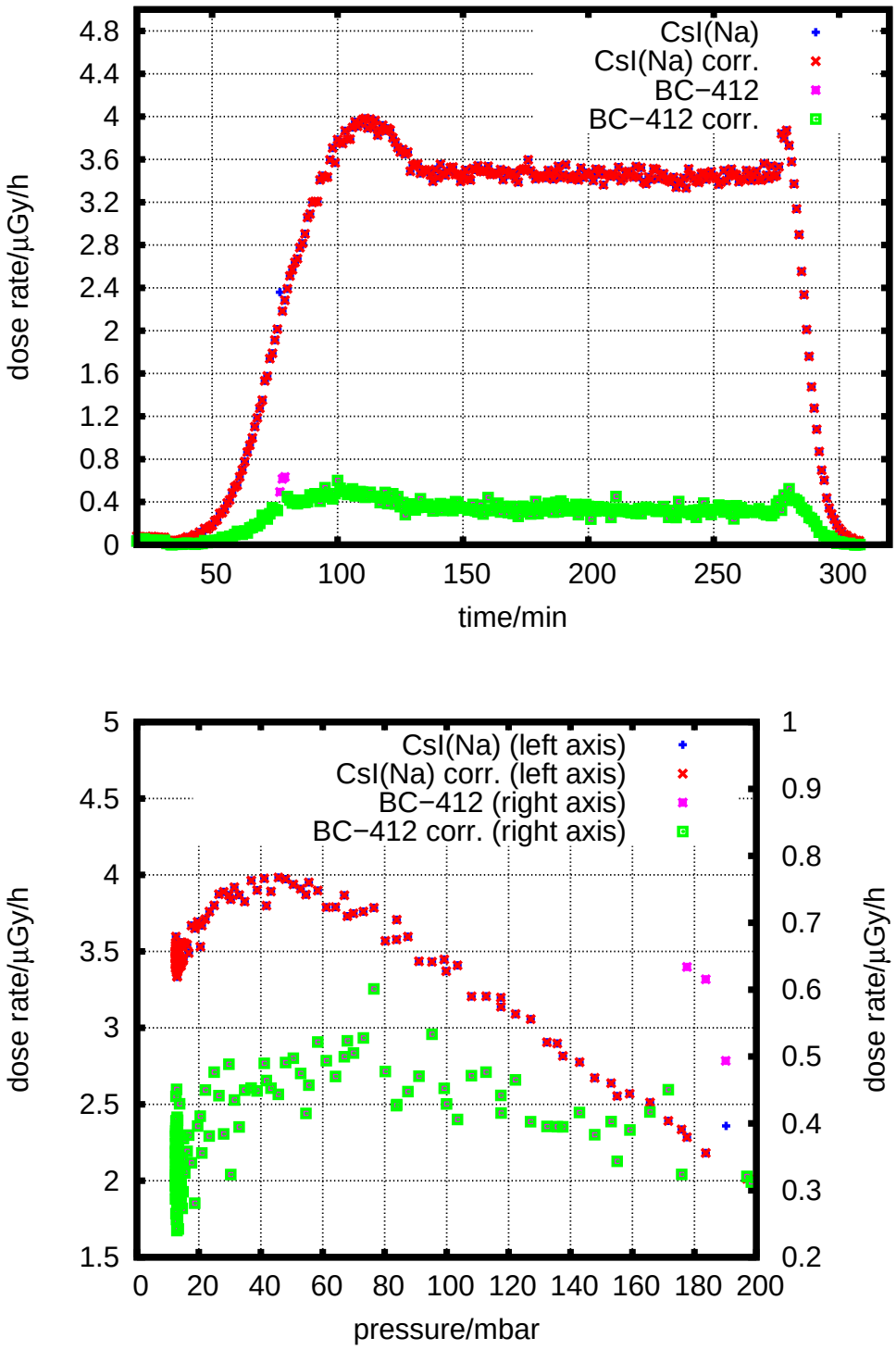

Figure F.6: *Upper panel: Dose rates for events in CsI(Na) and events in BC-412 with and without noise versus the time in minutes. Lower panel: The same data as in the upper panel but shown versus the pressure measured by the pressure sensor of the instrument*

Eidesstattliche Erklärung

Die vorliegende Abhandlung ist, abgesehen von der Beratung durch meine Betreuer, nach Inhalt und Form meine eigene Arbeit und sie hat weder ganz noch zum Teil schon an anderer Stelle im Rahmen eines Prüfungsverfahrens vorgelegen. Die Arbeit ist unter Einhaltung der Regeln guter wissenschaftlicher Praxis der Deutschen Forschungsgemeinschaft entstanden. Frühere Promotionsversuche wurden von mir nicht unternommen.
Teile dieser Arbeit wurden im Rahmen zwei verschiedenen Konferenzen veröffentlicht:

E. Scharrenberg, **E. M. Dönsdorf**, P. Kühl, H. Lohf, J. Marquardt, H. Winterfeld, *Measurement with a Phoswich detector on a stratospheric balloon*, Vortrag und Proceeding auf dem 21st ESA Symposium on European Rocket & Balloon Programmes and Related Research, Thun, Schweiz, 09.06-14.06.2013

E. Scharrenberg, S. I. Böttcher, S. Burmeister, **E. M. Dönsdorf**, B. Heber, P., Kühl, H. Lohf, J. Marquardt, H. Winterfeld, *Measurement with a Phoswich detector on a stratospheric balloon*, Poster and Proceeding auf der 33nd International Cosmic Ray Conference, Rio de Janeiro, Brasilien, 02.07.-09.07.2013

Desweiteren wurden Teile dieser Arbeit für das SED (**S**tudent **E**xperiment **D**escription) im Rahmen des BEXUS Projektes 2012 verwendet.

Eine kurze Beschreibung des in dieser Arbeit entwickelten Instruments, inklusive einer Skizze, befindet sich in der Masterarbeit von J. Marquardt: *Simulation des "Phoswich Instruments for Neutrons and Gammas" in der Atmosphäre*, eingereicht am 28. September 2012 an der Christian-Albrechts-Universität zu Kiel.

Kiel, den _____

(Esther M. Dönsdorf)

Danksagung/Acknowledgment

An dieser Stelle möchte ich allen danken, die mich während meiner Doktorarbeit unterstützt haben. Mein besonderer Dank gilt...

- ... Prof. Dr. Bernd Heber, der mir die Möglichkeit gegeben hat auf dem Gebiet der Instrumentenentwicklung in der Dosimetrie zu forschen, mir ermöglicht hat viele nationale und internationale Konferenzen zu besuchen und mich immer mit Diskussionen und konstruktiver Kritik unterstützt hat.

- ... Dr. Sönke Burmeister für seine Unterstützung, für die vielen Diskussionen und Gespräche über meine Arbeit sowie jegliche konstruktive Kritik.

- ... Dr. Stephan Böttcher für seine Unterstützung im Bereich der Elektronik sowie für die wertvollen Hinweise zur Datenanalyse.

- ... Dipl.-Ing. Lars Seimetz für das Erstellen der CAD-Zeichnungen und die Unterstützung bei allen mechanischen Fragen.

- ... Dipl.-Ing. Björn Schuster für seine Unterstützung im Bereich der Elektronik.

- ... Dr. Eckart Böhm für die vielen Diskussionen und hilfreichen Hinweise zu meiner Arbeit.

- ... allen Mitarbeitern der Arbeitsgruppe Extraterrestrik.

- ... Ing. Tatjana Naebert, Dr. Holger Vömel und allen Mitarbeitern vom Meteorologisches Observatorium Lindenberg des Deutschen Wetterdienstes, die es mir ermöglicht haben den stratosphärischen Ballonflug durchzuführen und mich während des Messfluges immer unterstützt haben.

- ... Susanne Meier und Dirk Jantze vom Meteorologisches Observatorium Lindenberg des Deutschen Wetterdienstes für die erfolgreiche Bergung meines Instruments nach dem Ballonflug.

- ... PD Dr. Frank Wissmann, allen Mitarbeitern der Physikalisch-Technische Bundesanstalt (PTB) sowie allen Mitarbeitern des iThemba Laboratory for Accelerator-Based Sciences, die es mir ermöglicht haben mein Instrument sowohl an der PTB in Braunschweig als auch am iThemba in Südafrika mit Neutronen zu kalibrieren.

- ... der Helmholtz Space Life Sciences Research School *SpaceLife*, durch deren finanzielle Unterstützung viele Dienstreisen ermöglicht wurden.

- ... Dr. Thomas Berger für gute Diskussionen, insbesondere über Aspekte der Dosimetrie.

- ... Prof. Bruce McKibben für gute Diskussionen und viele wertvolle Hinweise über verschiedenste Aspekte von Phoswich-Detektoren.

- ... meinen Eltern, meiner Oma, meiner gesamten Familie, allen meinen Freunden und meinem Partner für die große Geduld und bedingungslose Unterstützung während der gesamten Zeit.

I would like to thank the German Aerospace Center (DLR), the Swedish National Space Board (SNSB), EuroLaunch, the Esrange Space Center and the Swedish Space Corporation (SSC) for the possibility to fly the instrument onboard the stratospheric balloon BEXUS 14.
This experiment was carried out as a part of the REXUS/BEXUS programme. The REXUS/BEXUS programme is realised under a bilateral Agency Agreement between the German Aerospace Center (DLR) and the Swedish National Space Board (SNSB). The Swedish share of the payload has been made available to students from other European countries through a collaboration with the European Space Agency (ESA). EuroLaunch, a cooperation between the Esrange Space Center of the Swedish Space Corporation (SSC) and the Mobile Rocket Base (MORABA) of DLR, is responsible for the campaign management and operations of the launch vehicles. Experts

from DLR, SSC and ESA provide technical support to the student teams throughout the project.